



# Holocene sediment transport and climate variability of offshore Adélie Land, East Antarctica

By

Anna Borisovna Albot

A thesis

submitted to Victoria University of Wellington

in partial fulfilment of the requirements for the degree of

Master of Science

in Geology

Victoria University of Wellington

Wellington, New Zealand

2017



## Abstract

Grain size analysis of the terrigenous fraction of a laminated diatom ooze dating back to 11.4 kyr recovered offshore Adélie Land, East Antarctic margin was used to examine variations in sediment transport, depositional environments and Holocene climate variability at the location. Interpretations were assisted by additional proxies of primary productivity ( $\delta^{13}\text{C}_{\text{FA}}$ , BSI%), glacial meltwater input ( $\delta\text{D}_{\text{FA}}$ ) and subsurface temperature ( $\text{TEX}^{\text{L}}_{86}$ ). Three lithologic intervals with distinct grain size distributions were identified. At  $\sim 11.4$  ka the diatom ooze has a clear glacial influence which gradually decreases until  $\sim 8.2$  ka. During this time interval, coincident with the early Holocene warm period, sediment is inferred to have been delivered by glacial meltwater plumes and ice-bergs in a calving bay environment. It is suggested that the glaciers in Adélie Land had retreated to their present day grounding lines by 8.2 ka, and from then on sediment was delivered to the site primarily via the Antarctic Coastal and Slope Front Currents, largely through a suspended sediment load and erosion of the surrounding banks. Enhanced biogenic mass accumulation rates and primary production at 8.2 ka suggest onset of warmer climatic conditions, coincident with the mid-Holocene Climatic Optimum.

At  $\sim 4.5$  ka, grain size distributions show a rapid increase in mud content coincident with a transient pulse of glacial meltwater and a sudden decrease in biogenic and terrigenous mass accumulation rates. The increased mud content is inferred to have been deposited under a reduced flow regime of the Antarctic Coastal and Slope Front Currents during the Neoglacial period that followed the final stages of deglaciation in the Ross Sea. It is hypothesised here that cessation of glacial retreat in the Ross Sea and the development of the modern day Ross Sea polynya resulted in enhanced Antarctic Surface Water production which led to increased sea ice growth in the Adélie Land region. The presence of sea ice led to reduced primary production and a decrease in the maximum current strength acting to advect coarser-sized terrigenous sediment to the core site during this time.

Sedimentation rates appear to have a strong correlation with the El Niño Southern Oscillation (ENSO) over the last 8.2 kyr, and are inferred to be related to changing sea ice extent and zonal wind strength. Light laminae counts (biogenic bloom events) appear to decrease in frequency during time intervals dominated by El Niño events. Spectral analysis

of the greyscale values of core photographs reveals peaks in the 2-7 year band, known ENSO periods, which increase in frequency in the mid-and-late Holocene. Spectral analyses of the sand percent and natural gamma ray (NGR, a measure of clay mineral input) content of the core reveal peaks in the ~40-60, 200-300, 600, 1200-1600 and 2200-2400 year bands. The most significant of these cycles in the NGR data is in 40-60 year band may be related to internal mass balance dynamics of the Mertz Glacier or to the expansion and contraction of the Antarctic circumpolar vortex. Cycles in the 200-300 and 2200-2400 year bands are related to known periods of solar variability, which have previously been found to regulate primary productivity in Antarctic coastal waters. Cycles in the 590-625 and 1200-1600 year bands have a strong signal through the entire record and are common features of Holocene climatic records, however the origin of these cycles is still under debate between solar forcing and an independent mode of internal ocean oscillation.

## Acknowledgements

I would like to say a huge thank you to my supervisors Rob McKay and Lionel Carter who have guided me through this project and have always been happy to help with any questions I had. I have enjoyed my thesis year very much and am very happy with how the project turned out. Thank you also to Gavin Dunbar and Nancy Bertler who provided valuable feedback throughout the year, much appreciated.

A big thank you to Jane Chewings for her help in the lab during processing of my samples, especially for her understanding and helpful responses during equipment failure or accidental lab mishaps.

Thank you to Kate Newton and James Bendle for providing the  $\delta^{13}\text{C}$ ,  $\delta\text{D}$  and  $\text{TEX}^{\text{L}}_{86}$  (originally provided by Stefan Schouten) data for core U1357B and also data from core MD03-2601, originally sent by Xavier Crosta. Thank you also to Christina Riesselman for providing the BSi% data for core U1357B. These datasets were very helpful for the interpretations made in this thesis.

I wish to acknowledge the Rutherford Discovery Fellowship for granting Rob McKay funding for this project and Victoria University of Wellington for granting me the Victoria graduate and the Victoria Masters by thesis scholarships.

I am very grateful to my friends and family for the moral support and understanding that you provided me with during my years as a student, without you the road to get here would have been much harder. Thank you in particular to Olya, Hubert and Christoph whom I have shared an office with throughout the thesis year. You were always helpful if I had any questions and made the year full of entertainment. Most of all thank you to Agustin for your continued love and support. Thank you to all of the SGEES and ARC staff who have supported me throughout my years as a postgraduate and an undergraduate student at Victoria University.

# Table of Contents

1	Chapter 1: Introduction.....	1
1.1	Thesis context.....	1
1.2	Study Location .....	2
1.3	Thesis aims and objectives .....	3
1.4	Thesis outline.....	4
2	Chapter 2: Background.....	5
2.1	Basement of Wilkes Land Margin.....	5
2.2	Glacial history of East Antarctica.....	6
2.2.1	Prior to the Last Glacial Maximum .....	6
2.2.2	Last Glacial Maximum to Holocene history of the East Antarctic Ice Sheet.....	7
2.3	George-V-Adélie Land continental shelf bathymetry.....	8
2.4	Post-LGM glacial retreat on Adélie Land continental shelf.....	10
2.5	Antarctic Sea Ice, Meteorology and Primary Production.....	12
2.5.1	Sea Ice .....	12
2.5.2	Meteorology .....	13
2.5.3	Primary Production .....	15
2.6	Major modes of interannual climatic variability in the Southern Hemisphere.....	18
2.6.1	The Southern Annular Mode .....	18
2.6.2	The El Niño Southern Oscillation .....	20
2.6.3	SAM and ENSO coupling .....	25
2.7	Site Summary.....	26
2.8	Antarctic Bottom Water formation and ocean circulation offshore Adélie Land....	27
2.8.1	Bottom water formation in Antarctica .....	27
2.8.2	Bottom Water Formation offshore Adélie Land.....	29
2.8.3	Circulation of water masses offshore Adélie Land .....	30

2.9	Holocene climate in Antarctica.....	32
2.9.1	Long-term Holocene trends in East Antarctica .....	33
2.9.2	Millennial to centennial Holocene variability in East Antarctica .....	33
2.9.3	Holocene Climate Variability offshore Adélie Land .....	36
3	Chapter 3: Methodology .....	39
3.1	Core recovery and drilling disturbance issues.....	39
3.2	Core Lithostratigraphy .....	42
3.3	Age Model.....	43
3.4	Data generated by this project .....	44
3.4.1	Grain Size Analysis.....	44
3.4.2	Subsampling reproducibility .....	48
3.5	Additional uncertainties associated with grain size analysis using the LPSA .....	49
3.6	Linear sedimentation and mass accumulation rates.....	52
3.7	Image Analysis .....	53
3.8	Additional unpublished IODP-318-U1357B data used in the study .....	57
3.8.1	Natural Gamma Ray .....	57
3.8.2	Carbon and Deuterium isotopes.....	57
3.8.3	TEX <sub>86</sub> .....	57
3.8.4	Biogenic Silica.....	58
3.9	Time Series Analysis.....	58
4	Chapter 4: Results .....	61
4.1	Grain size analysis.....	61
4.1.1	Variations in mud and sand percentages.....	61
4.1.2	Mean grain size and sorting.....	65
4.2	Linear sedimentation and mass accumulation rates.....	65
4.3	Grainsize frequency distributions.....	69
4.3.1	Interval 1 .....	70

4.3.2	Interval 2 .....	70
4.3.3	Interval 3 .....	73
4.4	Laminae counting .....	73
4.5	Spectral Analysis .....	75
5	Chapter 5: Discussion .....	81
5.1	Sedimentary processes at IODP Site U1357 .....	81
5.1.1	Interval 3 (early Holocene ~11.4-8.2 ka).....	81
5.1.2	Interval 2 (mid-to-late Holocene ~8.2 to 4.5 ka BP) .....	84
5.1.3	Interval 1 (Late Holocene, ~4.5 ka to present) .....	91
5.2	Comparisons with other Antarctic records .....	92
5.2.1	Comparison of U1357B with other records in the Adélie Land region.....	92
5.2.2	Far field Antarctic records.....	96
5.2.3	Millennial-to-centennial climate variability.....	98
6	Chapter 6: Conclusions and Future Work .....	105
6.1	Conclusions.....	105
6.2	Future Work.....	108
	Appendices.....	111
	References.....	113

## List of Figures and Tables

### Chapter 1

Figure 1.1: Aerial view the of study area .....3

### Chapter 2

Figure 2.1: Geological map of Wilkes Land region.....6

Figure 2.2: Bathymetric map of Adélie Land region .....9

Figure 2.3: Map of Adélie Land continental shelf showing the location of sediment cores used to study Holocene climate variability of the region..... 12

Figure 2.4: Schematic map of major ocean currents in the Southern Hemisphere ..... 15

Figure 2.5: Seasonal values of the Southern Annular Mode index (1955-2010)..... 19

Figure 2.6: Schematic diagram of the El Niño Southern Oscillation phenomenon .....22

Figure 2.7: Sea surface temperature composites (°C) for El Niño and La Niña conditions in the Pacific and Southern Oceans ..... 24

Figure 2.8: Schematic diagram of the Amundsen Sea Low under La Niña/El Nino conditions25

Figure 2.9: Bathymetric map of the Adélie Land region showing movement of various water masses and ocean currents.....27

Figure 2.10: Map of the East Antarctic sector of the Southern Ocean displaying major Antarctic Bottom Water pathways.....28

Table 1: Mean and standard deviation values of current meter data offshore Adélie Land (139.5°E, 65.1°S) collected for two time periods in 1994-1995.....30

Figure 2.11: Bathymetric map of the Adélie Land region showing the circulation of various water masses in the region .....32

Figure 2.12: Map of Antarctica showing the location of ice cores used in the study by Masson et al. (2000).....	34
Figure 2.13: Millennial-scale Antarctic climate variability throughout the Holocene.....	36
Figure 2.14: Summary figure of climate variability along the Adélie Land coast for the past 11,500 years.....	37
 <b>Chapter 3</b>	
Figure 3.1: Schematic example of the three depth scales (CSF-A; CSF-B; CSF-D) used in this study .....	41
Figure 3.2: 3.2: Age model for the U1357B core based on 87 radiocarbon analyses .....	44
Figure 3.3: Grain size curves produced from replicate runs of core 1357B samples and the quartz glass bead standard .....	46
Figure 3.4: Smear slide image of sample 19-5H 43/45 after chemical treatment.. .....	48
Figure 3.5: Grain size curves of representative samples (original and repeat runs) that were subsampled after chemical treatment and the least square regression of sand percent from the same samples .....	50
Figure 3.6: Grain size curves of representative samples (original and repeat runs) that were subsampled prior to chemical treatment and the least square regression of sand percent for the same samples .....	51
Figure 3.7: Moisture and density values from discrete sample of core U1357A with a linear interpolation fitted through the data.....	53
Figure 3.8: Visual example of lamina counting for cores 4H-6, 5H-7, 10H-7 and 17H-5.....	55
Figure 3.9: Images of colour development upon surficial oxidation in freshly split surfaces of core U1357A-6H-4 .....	56
 <b>Chapter 4</b>	
Figure 4.1: Mud percent and sand percent of dark and light laminae for U1357B .....	62

Figure 4.2: Natural gamma ray counts and clay percent of dark and light laminae for U1357B .....	63
Figure 4.3: Normalised (to the overall terrigenous content) mud, sand and clay percent of dark and light laminae for U1357B .....	64
Figure 4.4: Sorting and mean grain size of dark and light laminae for U1357B .....	66
Figure 4.5: Linear sedimentation curve for U1357B.....	67
Figure 4.6: Mass accumulation rates for the biogenic and terrigenous components of U1357B .....	68
Figure 4.7: Normalised (to the overall terrigenous content) mud percent of dark and light laminae and biogenic silica of dark and light laminae for U1357B.....	69
Figure 4.8: Grain size distributions of dark laminae for Interval 1, 2 and 3 .....	71
Figure 4.9: Grain size distributions of light laminae for Interval 1, 2 and 3. ....	72
Figure 4.10: Linear sedimentation rate, laminae counts per 100 years and laminae counts per metre for U1357B .....	74
Figure 4.11: REDFIT and Wavelet analysis of the mean sand percent for core U1357B .....	77
Figure 4.12: Multi-taper and Wavelet analysis of the natural gamma ray content of core U1357B.....	77
Figure 4.13 Multi-taper analysis of the greyscale data for core U1357B. ....	79
<b>Chapter 5</b>	
Figure 5.1: Schematic representation of a calving bay reentrant model. ....	84
Figure 5.2: Seismic image of U1357B core site .....	86
Figure 5.3: Summary figure of datasets from core U1357B, MD03-2601 and the principal component one (PC1) from four East Antarctic $\delta^{18}\text{O}$ ice core records .....	88

Figure 5.4: Map of Antarctica showing the location of Site U1357B, Palmer Deep ODP Site 1098 and the four East Antarctic  $\delta^{18}\text{O}$  ice core records used to derive PC1 by Masson-Delmotte et al. (2011)..... 97

Figure 5.5: Holocene ENSO frequency derived by Zhang et al. (2014) plotted with mass accumulation rate of biogenic sediment, laminae counts per 100 years and linearly detrended laminae per metre for U1357B..... 100

## Abbreviation Index

### Text Abbreviations

AABW	Antarctic Bottom Water
AASW	Antarctic Surface Water
ACC	Antarctic Circumpolar Current
ALBW	Adélie Land Bottom Water
BSi%	biogenic silica weight percent
CO <sub>2</sub>	carbon dioxide
CDW	Circumpolar Deep Water
CSF	core depth below seafloor
EAIS	East Antarctic Ice Sheet
ENSO	El Niño Southern Oscillation
HSSW	High Salinity Shelf Water
IBRD	ice-berg rafted debris
IODP	Integrated Ocean Drilling Program (now International Ocean Discovery Program)
ISW	Ice Shelf Water
LGM	Last Glacial Maximum
LPSA	Laser Diffraction Particle Size Analyser
LSR	Linear sedimentation rate
MAR	mass accumulation rate
MCDW	Modified Circumpolar Deep Water
MIZ	marginal ice zone
MSW	modified shelf water
MTM	multi-taper analysis

NGR	natural gamma ray
PFZ	Polar Front Zone
RSBW	Ross Sea Bottom Water
SAM	Southern Annular Mode
SST	sea surface temperature
TEX <sup>l</sup> <sub>86</sub>	tetraether lipid-based paleothermometer
WAIS	West Antarctic Ice Sheet
<sup>14</sup> C	carbon-14
δ <sup>13</sup> C	ratio of carbon-13 to carbon-12
δ <sup>15</sup> N	ratio of nitrogen-15 to nitrogen-14
δ <sup>18</sup> O	ratio of oxygen-18 to oxygen-16
δD	ratio of deuterium to hydrogen

### Units of Measurement

%	percentage; a number or ratio as a fraction of 100
°C	degrees Celcius; unit of temperature, the freezing point of water at one atmosphere is 0°C = 273.15°K
cm	centimetre; unit of length, equivalent to one hundredth of a metre
cm/yr	centimetre per year
cm <sup>-1</sup>	centimetres per second
g	gram; unit of mass, equivalent to one thousandth of a kilogram
g/cm <sup>2</sup> /yr	grams per centimetre squared per year
g/cm <sup>3</sup>	grams per centimetre cubed
g/L	grams per litre; a litre is the base SI unit of volume
ka/kyr	thousands of years before present/thousand years (duration)
km	kilometre; unit of length, equivalent to one thousand metres

km <sup>2</sup>	kilometres squared; measure of surface area
m	metre; base SI unit of length
Ma	millions of years before present
Mbsf	metres below sea floor
mL	millilitre; unit of volume, equivalent to one cubic centimetre
mm	millimetre; unit of length, equivalent to one hundredth of a metre
ms <sup>-1</sup>	metres per second
rpm	revolutions per minute
wt%	weight percent
years BP	years before present
μm	micron; unit of length, equivalent to one millionth of a metre

# Chapter 1: Introduction

## 1.1 Thesis context

The East Antarctic Ice Sheet (EAIS) is the largest ice sheet in the world, storing the equivalent of ~53 m of potential sea level rise (Fretwell, et al., 2013), and influencing global climate through interactions with the ocean, sea ice and atmosphere of the Southern Hemisphere (Golledge et al., 2015; DeConto and Pollard, 2016). Over the last few decades, significant changes in ice sheet stability have been observed at ocean margins of the West Antarctic Ice Sheet (WAIS). Wind-driven incursions of Modified Circumpolar Deep Water (MCDW) onto Antarctic continental shelves are proposed to be the main driver of ice shelf melting and potential marine ice sheet instability (Jacobs et al., 2011; Pritchard et al., 2012; Joughin et al., 2014). The EAIS is largely grounded on bedrock above present sea level and is considered relatively stable compared to the WAIS, which is mostly grounded several km below sea level (Anderson, 1999). However, recent research suggests that the EAIS may have contributed 3-5 m of sea level during the last interglacial (130-115 ka) and that the ice sheet margin in the Wilkes Land sector retreated several hundred kilometres inland of the present day grounding line during a warm interval in the Pliocene (5.3-3.3 Ma) (Dutton and Lambeck, 2012; Cook et al., 2013; Fogwill et al., 2014) (Figure 1.1). Antarctic continental shelves commonly exhibit an over-deepened, reverse slope bathymetry that is thought to have resulted in a runaway marine retreat and contributed to an accelerated sea level rise during the last deglaciation (Thomas and Bentley, 1978; Golledge et al., 2014; McKay et al., 2016). Hence, it is important to reconstruct glacier dynamics and ocean-atmosphere interactions at Antarctic continental margins in order to improve future predictions of sea level rise.

With an increase in carbon dioxide (CO<sub>2</sub>) concentrations and global atmospheric and oceanic temperatures predicted for the 21<sup>st</sup> century (Pachauri et al., 2014), model simulations of the Southern Ocean region show a decrease in sea ice extent, freshening of surface waters, increase in the Southern Hemisphere westerly winds, and enhanced MCDW upwelling and CO<sub>2</sub> ventilation from deeper waters (Cai et al., 2005; Russell et al., 2006; Anderson et al., 2009; Sen Gupta et al., 2009; Kushara and Hasumi, 2013). These changes are projected to weaken Antarctic Bottom Water Formation (AABW) which plays a first order control on heat, salt, nutrient and CO<sub>2</sub> storage and transport around the globe via the meridional overturning circulation (Marsland et al., 2007; Marshall and Speer, 2012; Spence et al., 2012). Recent

observations confirm strengthening of the westerly winds over the Southern Ocean, enhanced MCDW upwelling and freshening and reduction of AABW formation (Thompson and Solomon, 2002; Whitworth, 2002; Rintoul, 2007; Jacobs et al., 2011).

Based on atmospheric temperature records from ice cores, the Holocene epoch (11.7 ka to present) is defined as an interval of relatively stable atmospheric CO<sub>2</sub> concentrations and climate, relative to the last glacial period (Masson et al., 2000; Masson-Delmotte et al., 2011). However, paleoceanographic studies have revealed significant variations in sea ice extent and duration, primary productivity and sea surface temperatures in the Southern Ocean sector of Antarctica, with potential implications for AABW formation (Presti et al., 2003; Nielsen et al., 2004; Crosta et al., 2007; Denis et al., 2009a). Some of these climatic variations have been attributed to changes in zonal wind stress and upwelling dynamics, though there are large uncertainties with dating of specific events. Thus, there is a need for well-dated high resolution records of paleoceanographic change in order to better understand past variations in Antarctic Ice Sheet extent, ocean-ice interactions, and associated biological change, through the Holocene. Such data will provide context for the modern observations of change at the Antarctic margin, as well as providing critical constraints for numerical models to improve future predictions of Antarctic atmospheric-oceanic-sea ice processes in a warming world.

## 1.2 Study Location

Integrated Ocean Drilling Program (IODP) Expedition 318 recovered a 170 m sediment core in February 2010, at Site U1357 within the Adélie Basin (core IODP-318-U1357B, 66°24.7990'S, 140°25.5705'E; Figure 1.1). The core consists of diatom ooze, a drift deposit that is thought to contain laminae representing annual depositional events (Escutia et al., 2011). Site U1357 is located downwind and downcurrent of the Mertz Glacier polynya, a region of significant primary productivity thought to be responsible for ~30% of the total AABW production (Meredith, 2013). The site is also heavily influenced by katabatic “drainage” winds from the Antarctic continent, the zonal flow of the polar easterlies, and changes in local productivity and sea ice. There is limited knowledge of the variability of these systems at the EAIS margin throughout the Holocene from sedimentary marine records, and none have annual to near-annual resolution (Escutia et al., 2011).

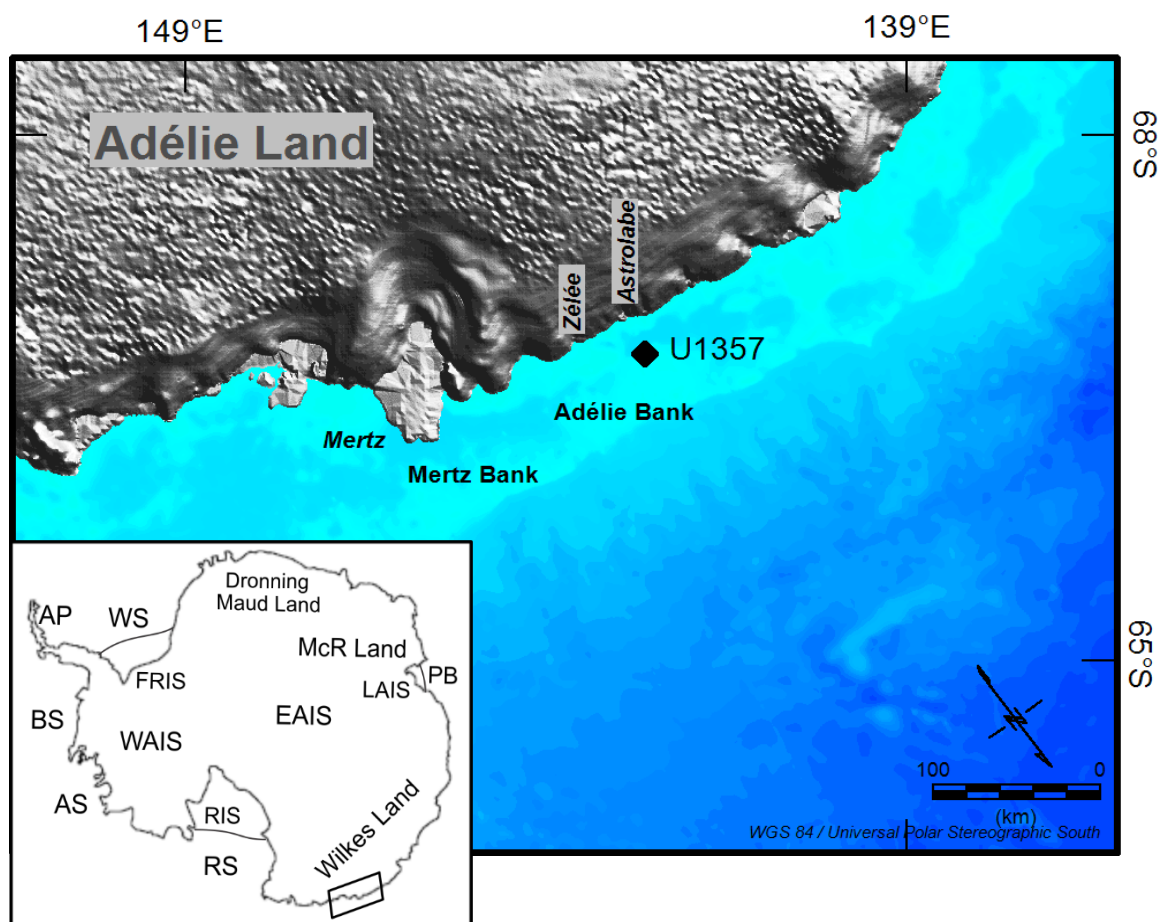


Figure 1.1: The location of the core Site U1357 and major EAIS outlet glaciers in the region (in italics). The insert shows the location of the study area (black rectangle) and other Antarctic locations discussed in the text. Ross Sea (RS); Amundsen Sea (AS); Weddell Sea (WS); Bellingshausen Sea (BS); Ross Ice Shelf (RIS); Filchner-Ronne Ice Shelf (FRIS); Antarctic Peninsula (AP); Mac.Robertson (McR) Land; Lambert-Amery Ice Shelf (LAIS); Prydz Bay (PB); West Antarctic Ice Sheet (WAIS) and East Antarctic Ice Sheet (EAIS).

### 1.3 Thesis aims and objectives

The aim of this thesis is to assess the physical processes of sedimentary transport and deposition at Site U1357 throughout the Holocene. Grain size analysis of the terrigenous component within U1357B and image analysis of the core photographs are used to examine the relative influences of various depositional processes at the drift deposit – including aeolian transport, ice-berg rafting, glacial meltwater plumes, primary production and ocean bottom-water currents.

Previous studies have suggested that the EAIS in the region had retreated to its present day grounding line by ~10.6 ka, however the majority of these studies were limited by incomplete recovery of Holocene sediment sections and poorly resolved carbon-14 ( $^{14}\text{C}$ ) dating due to reworking of older carbon (Mackintosh et al., 2014; see Section 2.4). A preliminary age model for U1357B has been developed by Prof Rob Dunbar (Stanford University, USA), which indicates minimal sediment reworking and places the base of the U1357B core at 11.4 ka, with an approximate sedimentation rate of 1.5 cm/yr and sampling resolution of 66 years (see Section 3.3). Thus another objective of this study is to help constrain the age of deglaciation and the retreat of the EAIS to its present day grounding line in the Adélie Land region.

Although this thesis is a standalone study, it was designed to contribute a key dataset that would assist in the interpretation of a broader geochemical and paleontological dataset from U1357B, and as such some aspects of the interpretations and hypotheses proposed here require further testing. Comparison to other near- and far-field paleoclimatic records are also used to guide the hypotheses developed in this thesis.

#### 1.4 Thesis outline

This thesis comprises six chapters. Chapter 1 outlines the context behind this study, its aims and objectives. Chapter 2 is an overview of the deglacial history of the region and modern oceanographic/atmospheric processes that influence sediment deposition to Site U1357B. Chapter 3 describes the methodology employed in this study to reconstruct Holocene paleoceanographic history from offshore Adélie Land. Chapter 4 details the results of grain size and image analyses. Chapter 5 discusses the interpretation of these results in the context of transport mechanisms and depositional environments. This chapter also evaluates the correlation of the datasets derived in this study with other U1357B proxies, and near- and far-field paleoclimatic records. Chapter 6 outlines the main conclusions and synthesis of this study.

## Chapter 2: Background

### 2.1 Basement of Wilkes Land Margin

The geology beneath the Wilkes Land sector of the East Antarctic Shield basement largely consists of Precambrian metamorphic rocks and granitoids of early Cambrian age, which either intruded or were derived by partial melting of the metamorphic basement (Kleinschmidt and Talarico, 2000; Goodge and Fanning, 2010). A structural boundary at approximately 147°E separates crystalline basement complex of metamorphic rocks and dolerites forming the East Antarctic craton to the west of the Mertz Glacier from granites and Triassic sandstones within the Wilkes Land subglacial basin to the east (Figure 2.1). The Wilkes Land basin is 1400x600 km in area, and extends beneath the EAIS. Its origin is debated to be the primary result of either lithospheric flexure (ten Brink et al., 1997) or back-arc rift basin forming processes (Ferraccioli et al., 2009).

The Wilkes Land continental margin is believed to have formed as a result of Australia detaching from Gondwanaland by 80 Ma (Lawver et al., 1992; Anderson, 1999). The separation of the Australian continent from East Antarctica resulted in the formation of the Southern Ocean and the isolation of the Antarctic continent in its modern position (Anderson, 1999; De Santis et al., 2010). A transpressional phase associated with the onset of fast spreading of Pacific-Indian Ocean in Paleocene-Eocene times reactivated previous structures, and folded and faulted sedimentary strata located beneath the inner continental shelf. Consequently, the basement across the Wilkes Land margin consists of block-faulted continental and oceanic crust with the transition zone between the two characterised by deep marginal rift basins, which are sites of significant sediment accumulation with a maximum 8 km sediment thickness (Eittreim, 1994; Escutia et al., 2005; De Santis et al., 2010). The post-rift evolution on the Wilkes Land margin is characterised by deposition of thick sedimentary sequences on the continental shelf, slope and rise. These were the target of drilling by the IODP Expedition 318 (Anderson, 1999; Escutia et al., 2005; Escutia et al., 2011).

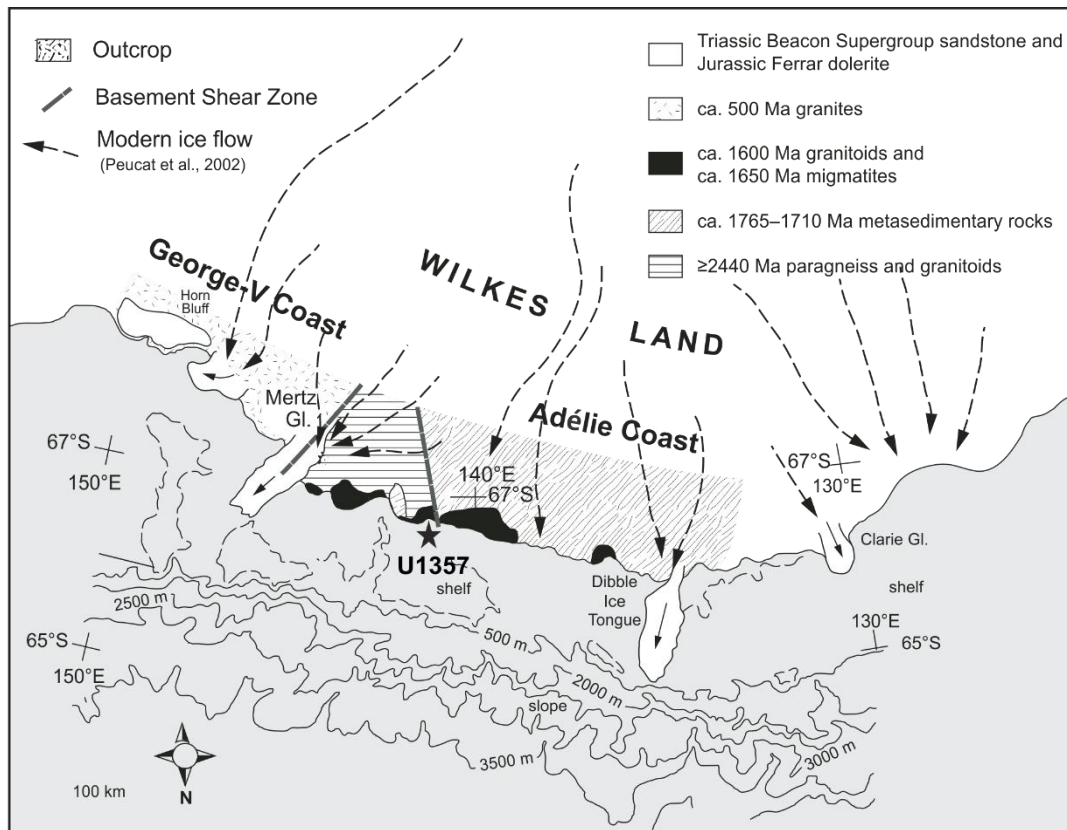


Figure 2.1: Map of Wilkes Land region, showing principal basement rock exposures and glacial features. U1357 is the site of the core that underpins this thesis. Modified from Gooch and Fanning (2010).

## 2.2 Glacial history of East Antarctica

### 2.2.1 Prior to the Last Glacial Maximum

Continental-scale ice sheets have been present in East Antarctica since the Eocene/Oligocene boundary, ~34 Ma, and are believed to be linked with the transition from greenhouse to ice house conditions when polar sea surface temperatures (SSTs) dropped by ~5°C and global ice volume increased by  $25 \times 10^6 \text{ km}^3$  (Zachos, 1996; Miller et al., 2008; Liu et al., 2009). The main drivers for glacial initiation in Antarctica are thought to be related to declining global atmospheric CO<sub>2</sub> (DeConto and Pollard, 2003; Haywood et al., 2010) and to the thermal isolation of Antarctica following the tectonic opening of the Southern Ocean gateways and formation of the Antarctic Circumpolar Current (ACC) (Kennet, 1976; Zachos, 1996; Bijl et al., 2013). In either case, these changes preconditioned the continent for glaciation, with the exact timing of glacial initiation at the Eocene/Oligocene boundary driven by a “cold” orbital

configuration of low seasonality (DeConto and Pollard, 2003; Coxall et al., 2005). Between 34 and 14 Ma, deep sea oxygen isotope records suggest the EAIS oscillated greatly in volume (Zachos, 1996).

A semi-permanent EAIS is thought to have been established by ~14 Ma, persisting through to the present day (Flower and Kennet, 1995; Sugden et al., 1993). However, recent provenance and ice-berg rafted debris (IBRD) studies from offshore of Wilkes Land, and far field sea level records suggest that its marine sectors may have deglaciated as recently as the late Pliocene contributing to global sea levels  $22\pm 10$  m higher than present day (Cook et al., 2013; Patterson et al., 2014; Miller et al., 2012).

### 2.2.2 Last Glacial Maximum to Holocene history of the East Antarctic Ice Sheet

During the Last Glacial Maximum (LGM, ~27-20 ka) global sea-levels were ~120 m lower than at present, and available geological evidence suggests that the EAIS expanded to near the present day continental shelf edge (Clark et al., 2009; Mackintosh et al., 2011; Mackintosh et al., 2014). The retreat of the EAIS during the transition from the LGM to the Holocene appears to show a general lack of synchronicity, although this interpretation is hampered by a lack of reliable and directly comparable age control from the various sectors of the East Antarctic margin (Verleyen et al., 2011; Mackintosh et al., 2014). Inland cosmogenic isotopes from glacial deposits in the Lambert/Amery system suggest that deflation of the EAIS associated with deglaciation began as early as 18 ka (Wagner et al., 2004; White et al., 2011). Radiocarbon dating of sedimentary cores from the continental shelf of Mac.Roberston Land and Prydz Bay give ages of ~14 ka for the onset of glacial retreat (Sedwick et al., 2001; Mackintosh et al., 2011). Two marine records of IBRD in the Southwest Atlantic, show an increase in IBRD flux at a similar time, ~14.5 ka (Weber et al., 2014). However, the bulk of marine geological evidence suggests that most of the EAIS rapidly retreated at the onset of the Holocene (~12 ka), which coincides with the early Holocene warm period (~11.5-9 ka) recorded in ice cores and lake sediment records (Finocchiaro et al., 2005; Mackintosh et al., 2011; Verleyen et al., 2011).

The early deglaciation at ~18 ka has been attributed to an abrupt post-glacial sea-level rise which enhanced the climatic sensitivity of some glacial systems (Golledge et al., 2012). The glacial retreats recorded at ~14 ka coincided with Melt Water Pulse 1a event, which involved a sea-level rise of 14-18 m between ~14.7 and 13.3 ka (Deschamps et al., 2012) and were most

likely related to it. Existing chronologies, combined with modelling experiments suggest that Melt Water Pulse 1a was unlikely to have been sourced from Antarctica alone. However, this sea-level pulse may have helped to initiate the main phase of ice-sheet recession in Antarctica, or contributed only a partial input to this event. Golledge et al. (2014) largely attribute the widespread deglaciation recorded at the onset of the Holocene to subsurface ocean warming which triggered the rapid retreat of marine-based Antarctic ice. This subsurface warming occurred due to a reduction in Southern Ocean upwelling, most likely as a result of the strengthening of the Atlantic Meridional Overturning Circulation at this time (McManus et al., 2004; Siani et al., 2013). Reduced upwelling led to a reduction in SSTs and expansion of sea ice –Antarctic Cold Reversal (Morgan, 2009), while also decreasing surface water ventilation which led to subsurface warming of the Southern Ocean. Importantly, these model experiments indicate that post-LGM EAIS retreat cannot be explained by an abrupt sea level rise and warming air temperatures alone.

Most evidence suggests that the EAIS reached its present day extent by the early-to-mid-Holocene, although a precise chronology is hampered by the general lack of reliable material (i.e. carbonate) to date the subglacial to glacial (i.e. deglacial) facies transition in sediment cores collected on the continental shelves around East Antarctica (Mackintosh et al., 2014). However, such a multistage deglaciation pattern across the EAIS is consistent to that observed in the Northern Hemisphere, where the ice sheets began to melt immediately after the LGM, but continued to disintegrate in various stages until the late Holocene (Siegert, 2001).

### 2.3 George-V-Adélie Land continental shelf bathymetry

The dominant features of the George-V-Adélie Land continental shelf, referred to from now on as Adélie Land, are overdeepened (>1200 m), shelf depressions: the Adélie Basin and the Adélie Depression (also called the George V Basin or Mertz-Ninnis Trough) (Beaman and Harris, 2005; Beaman et al., 2011). Bounding the northeast and west of the Adélie Depression are the Mertz and Adélie Banks, respectively. These extensive banks lie in water depths <300 m and are generally flat-topped (Figure 2.2). As commonly observed around Antarctica, the shelf exhibits a land-ward sloping, over-deepened bathymetric profile that is caused by glacial erosion and sediment loading onto the outer continental shelf (Dunbar et al., 1985; Anderson, 1999). Glacially-carved inner-shelf valleys plunge to depths of 1200 m over distances of only

several kilometres north of the coastline to form small enclosed basins or troughs. Two such valleys are evident near Site U1357, one directly perpendicular from the coast originating from the Astrolabe Glacier and one running parallel to the coast which probably originates from the interplay between the Mertz and Zélée glaciers (Beaman and Harris, 2005; Beaman et al., 2011). The small basins/troughs then connect to the larger Adélie and George V basins via narrow rugged canyons, which trend in varying directions across the inner-shelf.

The continental shelf break in the region varies between about 500 m water depth north of the Adélie and Mertz banks to slightly deeper depths of up to 660 m where broad cross-shelf valleys connect the Adélie Basin and Adélie Depression to the shelf edge, forming sills on the outer shelf (Figure 2.2). Large submarine canyons incise the continental slope in depths >1000 m (Beaman et al., 2011). Canyons are separated by steep parallel ridges ~200 m above the axes, before the canyons and ridges eventually merge into a relatively flat abyssal plain at ~3500 m depth.

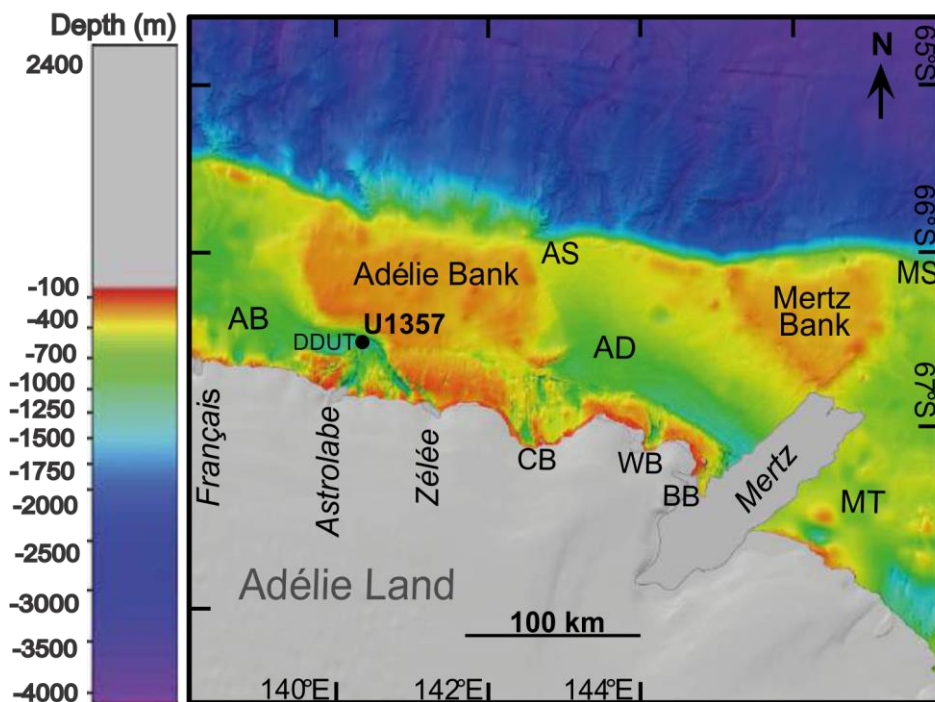


Figure 2.2: Bathymetric map of the Adélie Land region modified from Beaman et al. (2011). Major glaciers are indicated in italics; coastal bays: Commonwealth (CB); Watt (WB); Buchan (BB); bathymetric features: Dumont d'Urville Trough (DDUT); Adélie Basin (AB); Adélie Depression (AD); Adélie Sill (AS); Mertz Sill (MS); Mertz Trough (MT).

## 2.4 Post-LGM glacial retreat on Adélie Land continental shelf

The timing and pattern of post-LGM deglaciation of the Adélie Land continental shelf is constrained by sediment cores and geophysical (e.g. multibeam and seismic surveys) data. Mega-scale glacial lineations are present in the troughs and are unequivocal evidence of past ice-streaming and past grounded ice extending out to the continental shelf edge. Ice streams form as a result of a deformable till bed beneath the ice acting as a lubricant, allowing the ice above it to move more rapidly (Powell and Domack, 1995; Anderson et al., 2001). Mega-scale glacial lineations in the George-V Basin and Mertz Trough indicate that ice flow in the LGM was fed from the Mertz Glacier, while in the Adélie Basin ice flow resulted from the interplay between the Astrolabe and Zélée glaciers (Figure 2.3) (Beaman and Harris, 2005; McMullen et al., 2006; Beaman et al., 2011). The shoals, grooves, ice gouges, and depressions shaped by glacial ice and icebergs in these basins were used to reconstruct the ice-flow direction as aligned approximately parallel to the axes of the bathymetric troughs. Grounding zone wedges and lateral moraines in the Mertz Trough composed of diamicton with overlying diatomaceous sediments have been interpreted to represent the extent of the ice-sheet in Wilkes Land during the LGM, suggesting that in some parts the ice sheet may have only expanded out to the mid-shelf (Presti et al., 2005; McMullen et al., 2006). These features were formed from sediment that was transported beneath the Mertz Glacier towards its margins, and were deposited when the ice paused during its retreat.

Kasten cores recovered from the Mertz Trough (McMullen et al., 2006) and a sediment drift deposit (Mertz Drift) in the Adélie Basin (Harris et al., 2001; Presti et al., 2003; 2005) (Figure 2.3) reveal a similar stratigraphic succession of diamict overlain by laminated diatom ooze and diatom-bearing muds. The diamicts were interpreted to represent subglacial deposition during ice sheet retreat in the LGM. Deposition of diatom oozes in the Holocene was interpreted to represent pelagic sedimentation in seasonally-open waters after the ice sheet retreated. A slight increase in terrigenous content (muds and IBRD) at the top of the cores is interpreted to represent enhanced sediment supply associated with a change to cooler conditions following the mid-Holocene Climatic Optimum. In the Mertz Trough, only one core recovered the contact between the diamict and diatom ooze which gave a  $^{14}\text{C}$  age of  $\sim 6400 \pm 50$  years from Acid Insoluble Organic (AIO) residues from bulk sediment. However,  $^{14}\text{C}$  ages from AIO residues are subject to large uncertainties, in particular reworking of older (including pre-LGM) carbon which results in anomalously old ages. Combined with the highly

bioturbated nature of the sediment (which can act to bring younger carbon deeper into the sediment column) and the fact that the core was recovered from a grounding-line wedge located inland from one further out on the continental shelf, this date does not give a reliable estimate for the initiation of deglaciation in the region (Mackintosh et al., 2014). In the Mertz Drift, dates retrieved from just above the transition from sub-ice shelf to open water conditions calibrated by Mackintosh et al. (2014) loosely bracket the retreat of the Adélie Basin ice to ~11.3-21.2 ka. However, due to high potential for reworked pre-LGM organic material at this location (Harris et al., 2001; Presti et al., 2003), particularly in the deglacial mud-rich facies, these dates are considered to be a poor age constraint.

In the Adélie Basin, a 40 m-long piston core (MD03-2601) of laminated diatom ooze was recovered from the Dumont d'Urville Trough (Figure 2.3) (Denis et al., 2006; Crosta et al., 2007). The submillimetre to centimetre laminae in the diatom ooze, with minimal reworking through bioturbation, were interpreted to represent seasonal variability throughout the Holocene after the retreat of glacial ice. The oldest date from the core calibrated by Mackintosh et al. (2014) indicates that diatom oozes have been deposited in this basin since at least 10.6-11.15 ka, although this core did not penetrate into glacial retreat facies. The high-resolution record of post-LGM sedimentation (U1357B) examined in this study thus offers an opportunity to better constrain the timing and nature of glacial retreat in the Wilkes Land region, as well as climate variability throughout the Holocene.

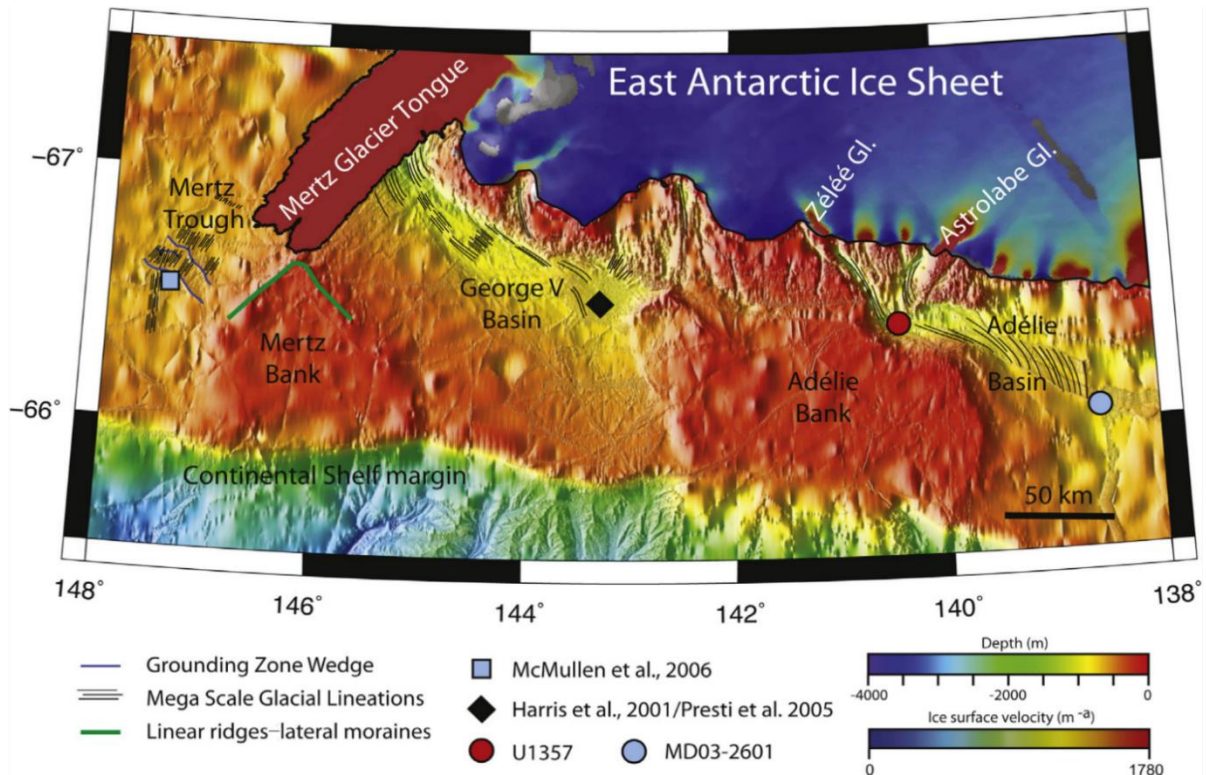


Figure 2.3: Map of Adélie Land continental shelf showing the major glaciers, shelf bathymetry, location of sediment cores discussed in Section 2.4 and LGM glacial features. Adapted from Mackintosh et al. (2014). Shelf bathymetry was derived from Beaman et al. (2011) and ice velocity from Rignot et al. (2011).

## 2.5 Antarctic Sea Ice, Meteorology and Primary Production

### 2.5.1 Sea Ice

Sea ice is a significant feature of Antarctica, extending from  $4 \times 10^6$  km<sup>2</sup> in the summer to  $19 \times 10^6$  km<sup>2</sup> in late winter (Cavalieri et al., 1999). Main factors controlling the formation of sea ice include seasonal insolation, SST (must be colder than  $-1.86^\circ\text{C}$  for sea ice to form), salinity, and surface wind speed, which advects ice away from the site of formation (Ackley and Sullivan, 1994; Pezza et al., 2012). In winter, sea ice extends out to  $\sim 60^\circ\text{S}$  in the Pacific, and  $\sim 55^\circ\text{S}$  in the Atlantic and Indian Oceans (Figure 2.4), but retreats to within a few kilometres off the Antarctic coast in spring and summer (Comiso and Nishio, 2008). The expansion and reduction of Antarctic sea ice exerts a significant control on the Southern Hemisphere climate by regulating ocean structure and circulation, exchange of heat and gases between the ocean and atmosphere, as well as affecting the formation of cyclonic weather systems and their paths of migration (Godfred-Spenning and Simmonds, 1996; Yuan and Martinson, 2000; Raphael, 2003; Pezza et al., 2012). These climatic signals in turn exert a control on the

equatorward heat transport by the atmosphere and the ocean, thus impacting the state of the global climate. At glacial/interglacial timescales, increases (decreases) in sea ice provide a feedback mechanism for atmospheric cooling (warming) by decreasing (increasing) CO<sub>2</sub> ventilation of the Southern Ocean (Anderson et al., 2009; Ayliffe et al., 2013). This effect is further enhanced by increased primary production and biological sequestration of CO<sub>2</sub> within the sub Antarctic zone due to greater aeolian deposition of iron to the surface ocean during glacial periods (Martin, 1990; Moore et al., 2000; Sigman et al., 2010). Sea ice therefore acts as an important coupling mechanism between the ocean and the atmosphere.

Over the satellite period beginning 1979, sea ice extent in the Southern and Northern Hemispheres has shown contrasting trends. While the Southern Hemisphere has experienced an overall increase (Turner et al., 2007; Comiso and Nishio, 2008), the Northern Hemisphere has had a substantial decline in sea ice extent, which has been partially attributed to 20<sup>th</sup> century warming of atmospheric and oceanic temperatures (Comiso, 2006; Comiso and Nishio, 2008). However, recent investigations show overall decreases in sea ice concentration and duration around the Antarctic Peninsula and the Amundsen and southern Bellingshausen seas while the rest of Antarctica shows a generally weak but increased sea ice trend (Kwok and Comiso, 2002; Liu et al., 2004; Pezza et al., 2012).

### 2.5.2 Meteorology

During the instrumental period (past ~60 years) surface air temperature trends from station data have recorded a dipole change across Antarctica with [i] significant warming over the Antarctic Peninsula (~0.5°C/decade), attributed mostly to rising atmospheric and oceanic temperatures of the 20<sup>th</sup> century; [ii] some warming over West Antarctica (~0.1°C/decade) and; [iii] little change in temperatures over East Antarctica, with cooling (~0.1°C/decade) recorded during some decades, although the continent-wide average near-surface temperature trend is positive (Turner et al., 2004; Steig et al., 2009). The mean annual temperature in the East Antarctic coastal region has been about -10°C, with positive temperatures generally confined to the summer months when lakes and coastal regions become ice free (Steig et al., 2009). As a result, a strong temperature gradient develops between Antarctica and the Southern Hemisphere mid-latitudes, thereby isolating a pool of very cold air above the Antarctic surface (referred to as the polar vortex) resulting in a temperature inversion – a condition in which the temperature of the atmosphere increases

with altitude in contrast to the normal decrease with altitude. The temperature inversion is maintained even in the summer months by radiative cooling from the highly reflective snow and ice surface. Because of this temperature inversion and the steep slope of the Antarctic terrain, cold air has a higher density than air at the same height down the slope which causes a gravitational air movement down the slopes of the continent – i.e. katabatic winds (Turner et al., 2009).

The prevailing wind direction at the Adélie Land coast is from the south-southeast, with higher wind speeds correlated with more southerly directions (König-Langlo et al., 1998). The southerly winds are associated with the katabatic drainage of air from the interior of the continent, which can extend up to 100 km offshore before being deflected to the west by the Coriolis force to join the flow of the polar easterlies (Adolphs and Wendler, 1995; Wendler et al., 1997a). These easterly winds generate a westward geostrophic coastal current at the surface referred to as the Antarctic Coastal Current, and the deeper westward Antarctic Slope Front Current which transports intermediate and bottom waters around the continent. (Bindoff et al., 2000; Carter et al., 2008). Interplay between low sea level pressures at the Antarctic coast (known as the circumpolar trough), higher pressures in the subtropics and the Coriolis force result in mid-to-high latitude westerly winds (Turner et al., 2009). These winds drive the eastward flow of the longest and largest oceanic current, the Antarctic Circumpolar Current (ACC; Figure 2.4), which encompasses the entire Antarctic margin and connects all of the world's major oceans (Carter et al., 2008).

The Adélie Land coast experiences the windiest conditions on Earth through the presence of the katabatic winds being funnelled by narrow glacial valleys close to the shoreline (Parish et al., 1993; Adolphs and Wendler, 1995; Wendler et al., 1997a). Mean annual wind speed values at Commonwealth Bay and Dumont d'Urville stations are  $20 \text{ ms}^{-1}$  and  $10 \text{ ms}^{-1}$  respectively. However during winter storms, speeds of  $>50 \text{ ms}^{-1}$  are exceeded at both stations (Wendler et al., 1997a; König-Langlo et al., 1998). The katabatic winds in this region have also been found to be reinforced by the passage of cyclonic disturbances near the coast (Parish et al., 1993; Adolphs and Wendler, 1995). During the summer season, the winds weaken significantly (~40-30%) compared to the winter season.

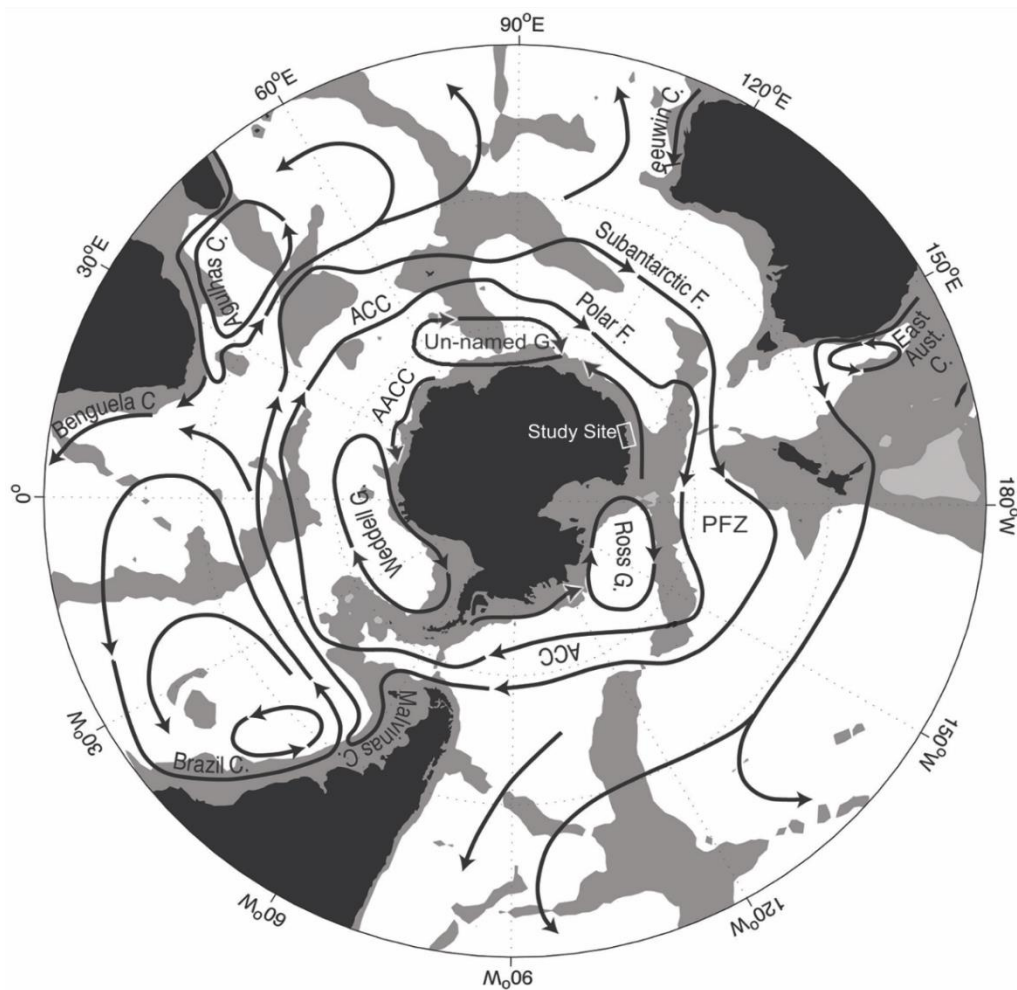


Figure 2.4: Schematic map of major ocean currents in the Southern Hemisphere. Depths shallower than 3500 m are shaded. The Southern Hemisphere westerly winds drive the Antarctic Circumpolar Current (ACC) in an eastward direction north of 64°S, while the polar easterlies drive the westward flow of the Antarctic Coastal Current (AACC) closer to the Antarctic coastline. The three large oceanic gyres reflect the interplay between low sea level pressures at the Antarctic coastline the ACC and the AACC (McCartney and Donohue, 2007; Carter et al., 2008). PFZ stands for Polar Front Zone; F: Front; C: Current; G: Gyre. Modified from Rintoul et al. (2001).

### 2.5.3 Primary Production

The Southern Ocean and the associated sea ice cover are widely recognised for the role they play in global carbon cycling and climate change as mentioned in Section 2.5.1. Waters over much of the Southern Ocean are characterised by high concentrations of macronutrients such as nitrate ( $\text{NO}_3^-$ ), phosphate ( $\text{PO}_4^{3-}$ ) and silicate ( $\text{SiO}_4^{4-}$ ) (Arrigo et al., 1998; Moore and Abbott, 2000), but low amounts of micronutrients like iron (Fe), which is essential for the synthesis of chlorophyll and thus photosynthesis (Martin et al., 1988). As a result, these high macro-

nutrient, low chlorophyll waters are characterised by low rates of primary production as phytoplankton (which provide the food base for most marine food chains) are not able to fully utilize the available macronutrients for growth without sufficient Fe supply. Exceptions include areas of extreme micro-nutrient upwelling such as: the Polar Front Zone (PFZ), defined at its southern margin by the Polar Front and the Sub-Antarctic Front as its northern boundary (Figure 2.4); and waters overlying the continental shelves in close proximity to the Antarctic land mass, termed the marginal ice zone (MIZ) (Moore and Abbott, 2000; Arrigo et al., 2008). Fe in these waters has been found to come from atmospherically-derived dust in sea ice melt, glacial calving and meltwater plumes, and resuspension of shelf sediments (Sedwick et al., 2000; Sambrotto et al., 2003; Croot et al., 2004). Upwelling of MCDW onto continental shelf during the summer season has been observed to coincide with episodic phytoplankton blooms and has thus been suggested to be an additional source of micronutrients in the MIZ, as well as a source of heat impacting sea ice and ice shelf melting (Prézelin et al., 2000; Sambrotto et al., 2003).

Sea ice is also a first order regulator of the availability of irradiance to phytoplankton, and hence controls phytoplankton distribution, abundance and production (Arrigo et al., 1998; Moore and Abbott, 2000). Rates of primary production in the MIZ are influenced by the degree of meltwater-induced stratification in the surface waters. Inputs of freshwater create a more stable water column by reducing the mixed layer depth, and thus produce a more favourable light environment for phytoplankton production. Weaker katabatic winds in summer prevent water column mixing and thus help to sustain well-stratified surface waters (Arrigo et al., 1998; 2008). During the seasonal retreat of sea ice, phytoplankton blooms extending over thousands of kilometres are observed within the MIZ with estimates typically derived from satellite ocean-colour estimates of chlorophyll (Moore and Abbott, 2000; Arrigo and van Dijken, 2003). However, this method has been proven to underestimate the true magnitude of primary production in the Southern Ocean with large-scale intra-ice phytoplankton blooms found to occur off the coast of East Antarctica in early autumn (Lieser et al., 2015). Sometimes such events are not detected by remote sensing, possibly due to masking by frazzle ice.

Particularly high rates of primary production have been identified in surface waters of polynyas that ring the Antarctic continent (Arrigo and van Dijken, 2003). Polynyas are large, persistent openings in sea ice maintained by strong katabatic winds that blow newly formed

ice away from the coast. As a result these open water areas are the first marine systems to be exposed to increased springtime solar radiation and meltwater stratification (Arrigo and van Dijken, 2003). Consequently, the ocean floor beneath polynyas receives an increased flux of biogenic silica (Dunbar et al., 1985; Leventer, 2003). Of particular importance from the phytoplankton group are diatoms. Diatoms have wide a range of habitat preferences, are abundant throughout Antarctic waters, are well-preserved in sediment, and can therefore be useful indicators of paleoceanographic change (Leventer, 1991; Stickley et al., 2005; Crosta et al., 2007).

Seasonal changes in diatom species offshore Adélie Land are well documented through sediment trap and water sampling transects (Riaux-Gobin et al., 2011; Beans et al., 2008) and sedimentary cores (Denis et al., 2006; Maddison et al., 2006; 2012; Crosta et al., 2007). In early spring, species associated with sea ice (e.g. *Thalassiosira antarctica*) dominate the diatom taxa. As sea ice retreats meltwater from glacial runoff and sea ice creates a well-stratified water column producing favourable conditions for diatoms that thrive in such conditions (e.g. *Thalassiosira antarctica* spp.). Towards late spring, diatoms associated with open water conditions (e.g. *Thalassiosira antarctica*) become the dominant species until the autumn period when sea ice-associated taxa reappear again (e.g. *Thalassiosira antarctica*, commonly used as proxy for autumn sea ice formation). Particularly thick biogenic lamina corresponding to mass depositional events have been documented in several sedimentary cores off Adélie Land (Maddison et al., 2006; Crosta et al., 2007). Thick laminae dominated by *Thalassiosira antarctica* spp. spores are believed to reflect deposition in well-stratified waters in close proximity to sea ice and are considered good proxies for spring sea ice melting and water column stratification (Crosta et al., 1997; Crosta et al., 2007). *Thalassiosira antarctica* spp. are deposited as the sea ice edge retreats during the spring season. In addition, relatively strong katabatic winds in early spring are known to cause intermittent mixing of the stratified surface waters and upwelling of deeper waters, resulting in deposition of biogenic laminae characterised by these species (Maddison, et al., 2006; Denis et al., 2006). Other diatoms known to deposit thick biogenic laminae are *Thalassiosira antarctica* spp. and *Thalassiosira antarctica* k. These diatoms thrive in open water conditions and are able to exploit a well-stratified water column which allows large prolonged blooms to occur. Mass sinking of these species occurs when water column stratification is destabilised by reduced sea ice melting in mid-to-late summer, which allows MCDW to upwell to the surface and creates a deeper mixed surface layer (Maddison, et al., 2006; Denis et al., 2006).

Seasonal and interannual changes in diatom species abundances offshore Adélie Land thus reflect fluctuations in sea ice extent caused by variations in SST and stratification, upwelling and katabatic wind strength. Currently, the response of primary production and resultant global carbon cycle in sea ice zones to global warming remains unclear and controversial, making it a priority to research its past variability and the likely causes (see Arrigo and Thomas, 2004; Arrigo et al., 2008).

## 2.6 Major modes of interannual climatic variability in the Southern Hemisphere

### 2.6.1 The Southern Annular Mode

The Southern Annular Mode (SAM) is a measure of the pressure difference associated with the movement of the westerly wind belt between the mid and high latitudes of the Southern Hemisphere (Thompson and Wallace, 2000; Marshall, 2003). There are two phases: a positive SAM is associated with lower sea level pressures at low latitudes, and vice versa for a negative SAM. As a consequence, during years with a positive (negative) SAM index, the westerly wind flow is intensified (weakened) in the Antarctic region and weakened (strengthened) north of 40°S (Thompson and Wallace, 2000; Marshall, 2003; Yuan and Li, 2008). SAM variability occurs on a variety of timescales from low frequency (inter-decadal—Thompson and Solomon, 2002) to high frequency (daily—Baldwin, 2001).

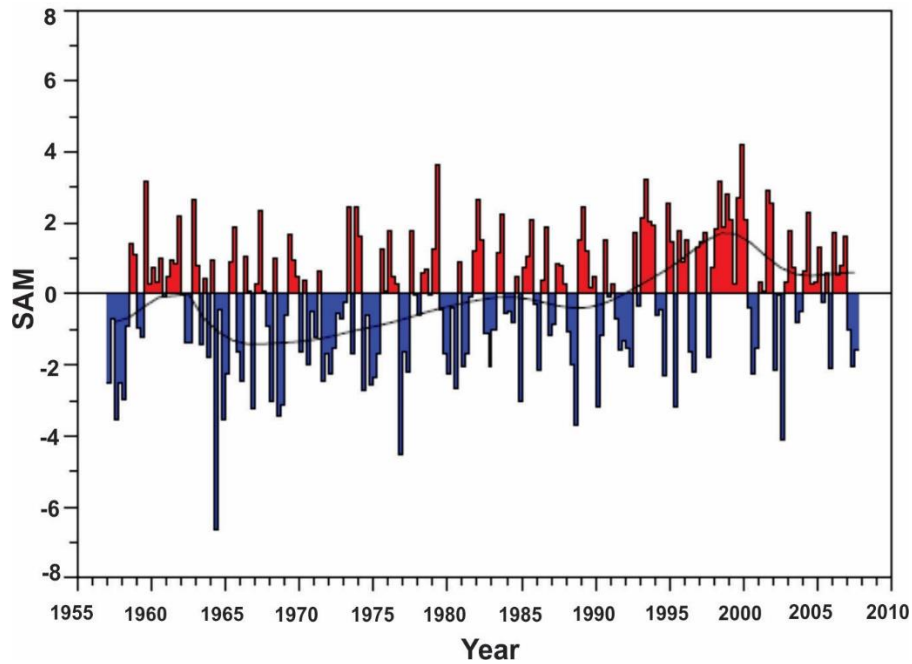


Figure 2.5: Seasonal values of the SAM index calculated from station data (Marshall, 2003). The smooth black curve shows decadal variations. Adapted from Turner et al. (2009).

The SAM index displays a significant positive long-term trend over the past 3-4 decades (Figure 2.5), particularly during austral summer, with a slightly smaller trend in autumn and winter and no trend in spring (Thompson and Solomon, 2002; Marshall, 2003; Fogt et al., 2009). This positive trend in the SAM has resulted in strengthening of the mean circumpolar westerlies by  $\sim 15\%$  (Marshall, 2003; 2007) and contributed to the spatial variability in Antarctic temperatures, specifically warming in the Antarctic Peninsula and West Antarctica, and cooling over East Antarctica (Kwok and Comiso, 2002; Marshall, 2007; Turner et al., 2009). A more positive SAM, associated with stronger circumpolar westerlies, isolates the continent more effectively from the advection of extra-tropical air masses into the coastal regions. In addition, a positive SAM reduces the speed of katabatic flow over much of East Antarctica leading to less disruption of the surface temperature inversion and colder temperatures over the continent (Van den Broeke and van Lipzig, 2003; Marshall, 2007).

Antarctic sea ice extent is consequently impacted by the strengthening (weakening) of westerly winds during positive (negative) phases of the SAM, however the trends in sea ice extent do not appear to be linearly correlated with the recorded changes in temperature (Liu et al., 2004; Yuan and Li, 2008). Numerous observational (Liu et al., 2004; Pezza et al., 2012; Turner et al., 2013) and modelling (Hall and Visbeck, 2002; Lefebvre et al., 2004) studies have

found a dipole response of sea ice to the SAM between the Ross/Amundsen and Weddell/Bellingshausen Sea regions, which they attributed to the pressure patterns associated with the negative and positive SAM phases. During positive SAM, the strengthening of the westerlies in the Antarctic region stimulates stronger cyclonic circulation of the Amundsen Sea Low ( $L_{AS}$ ) (Figure 2.8). This results in the Ross and western Amundsen Sea regions being exposed to stronger, cooler southerly winds, inducing cooling at the surface and promoting sea ice growth. Conversely, the Weddell/Bellingshausen and eastern Amundsen Sea regions are exposed to stronger, warmer northerly winds which serve to inhibit sea ice growth (Liu et al., 2004; Pezza et al., 2012; Turner et al., 2013). The relationship between SAM and sea ice offshore Adélie Land has been tested by Gregory (2012) who correlated the SAM index with sea ice concentrations in the region from 1978-2008. It was found that during positive SAM phases the region experienced increased sea ice concentrations ( $r=0.37$ ).

The positive trend of the SAM in recent decades has been related to both  $CO_2$  increases (Kushner et al., 2001; Marshall et al., 2004; Cai et al., 2005) and stratospheric ozone depletion (Thompson and Solomon, 2002; Roscoe and Haigh, 2007), both of which increase latitudinal temperature gradients in the upper troposphere which helps to shift high-altitude winds equatorward and sustain strong westerly winds and low pressure at high latitude regions.

## 2.6.2 The El Niño Southern Oscillation

The El-Niño-Southern Oscillation (ENSO) is the dominant mode of climate variability in the Pacific Ocean (Figure 2.6). It alters the Walker circulation cell and is the largest climatic cycle on decadal and sub-decadal time scales on Earth, with an influence on climate patterns well-beyond the low latitude Pacific where it is most marked (Turner, 2004). ENSO oscillates between a La Niña phase, which represents an intensification of normal conditions through strengthening of the Walker cell and an El Niño phase, which is caused by a weakening and an eastward migration of the Walker cell. The migration of the Walker cell during El Niño results in a redistribution of rainfall across the Pacific through changes to the Pacific SST gradient and depth of the thermocline (Fig 2.7) (Trenberth, 1991; Allan, 2000). The evolution of the ENSO cycle can be measured by a number of different indices (Turner, 2004), with the most common being the Southern Oscillation Index (SOI), which is the measured pressure difference between Darwin, Australia and Tahiti, French Polynesia (Parker, 1983). Analyses of ENSO

events during the instrumental period (Kirtman and Schopf, 1998; Timmerman and Jin, 2002) and through use of geological proxies (Moy et al., 2002; Conroy et al., 2008) have revealed that ENSO is an irregular climatic phenomenon with an average periodicity of 2-7 years, with each event lasting for an average of 18-24 months in modern records (An and Jin, 2004, Turner, 2004).

Over recent decades, the SOI has been reported to have a negative trend which corresponds to more frequent El Niño events in the equatorial Pacific (Kwok and Comiso, 2002; Yuan and Li, 2008). The recent El Niño trend is associated with negative sea ice cover anomalies in the eastern Ross and Amundsen seas and positive sea ice anomalies in the western Ross Sea and Bellingshausen/Weddell seas (Yuan and Martinson, 2000; Kwok and Comiso, 2002; Yuan, 2004; Pezza et al., 2012). Two main processes may be responsible for the transmission of the ENSO signal to the high latitudes. The warming of tropical SSTs during El Niño enhances tropical convection which strengthens (weakens) the subtropical jet stream and weakens (strengthens) the polar front jet in the South Pacific (South Atlantic). Consequently, more (less) heat is transported into the polar region in the South Pacific (South Atlantic) via the westerly winds (Figure 2.7). This pattern is reversed under La Niña conditions (Yuan, 2004; Lachlan-Cope and Connolley, 2006). The same tropical warming (cooling) during El Niño (La Niña) results in a Rossby wave train of alternating meanders in high altitude winds to be established between the central Pacific and the Bellingshausen-Amundsen Sea sector-termed the Pacific-South American Association pattern (Hoskins and Karoly, 1981; Ding et al., 2012).

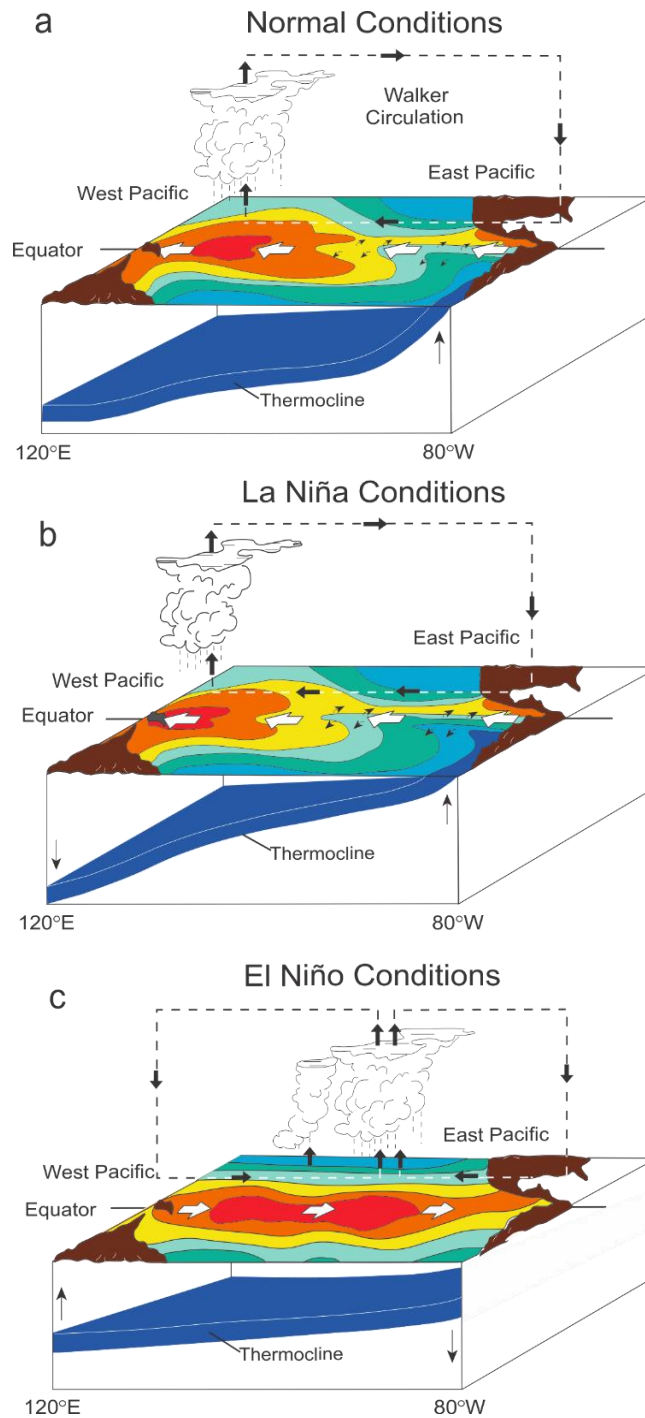


Figure 2.6: Schematic diagram of the Pacific Ocean under (a) Normal Conditions; (b) La Niña conditions; (c) El Niño conditions. The colour gradient indicates relative sea surface temperatures (SSTs), with red equating to warmest and blue coolest SSTs. White arrows represent the flow direction of surface waters. Modified from McPhaden (2015).

In response to weakening (strengthening) of the polar front jet during El Niño (La Niña) the low pressure centre in the Amundsen-Bellingshausen Sea sector is weakened (strengthened) and is shifted further east (west). During El Niño, this results in the Amundsen and Ross Sea sectors receiving warmer northerly winds which act to restrict sea ice growth while the Weddell/Bellingshausen seas are exposed to more southerly winds which cool the SSTs and enhance sea ice growth. This pattern is reversed during La Niña events (Figure 2.8; Yuan, 2004; Turner et al., 2013; Hosking et al., 2013). This dipole expression of ENSO in the Atlantic and Pacific sectors of Antarctica has been termed the Antarctic Dipole (Yuan and Martinson, 2000; Kwok and Comiso, 2002). The eastward (westward) shift of the L<sub>AS</sub> during El Niño (La Niña) has also been found to encourage katabatic wind flow from the West Antarctic Ice Sheet into the western (eastern) Ross Sea inducing (inhibiting) sea ice advance, thereby creating a dipole response to ENSO in the Ross Sea (Bertler et al., 2004; 2006; Figure 2.8).

Correlation of the SOI index and sea ice concentrations in Adélie Land region by Gregory (2012) reveal that sea ice advance is greater during El Niño events, suggesting that the influence of the enhanced katabatic wind strength extends out of the Ross Sea region and into East Antarctica. Together these studies indicate that a teleconnection exists between climate patterns in the southern high latitudes and the tropics, and that these climate patterns exert a control on sea ice distributions in Antarctica.

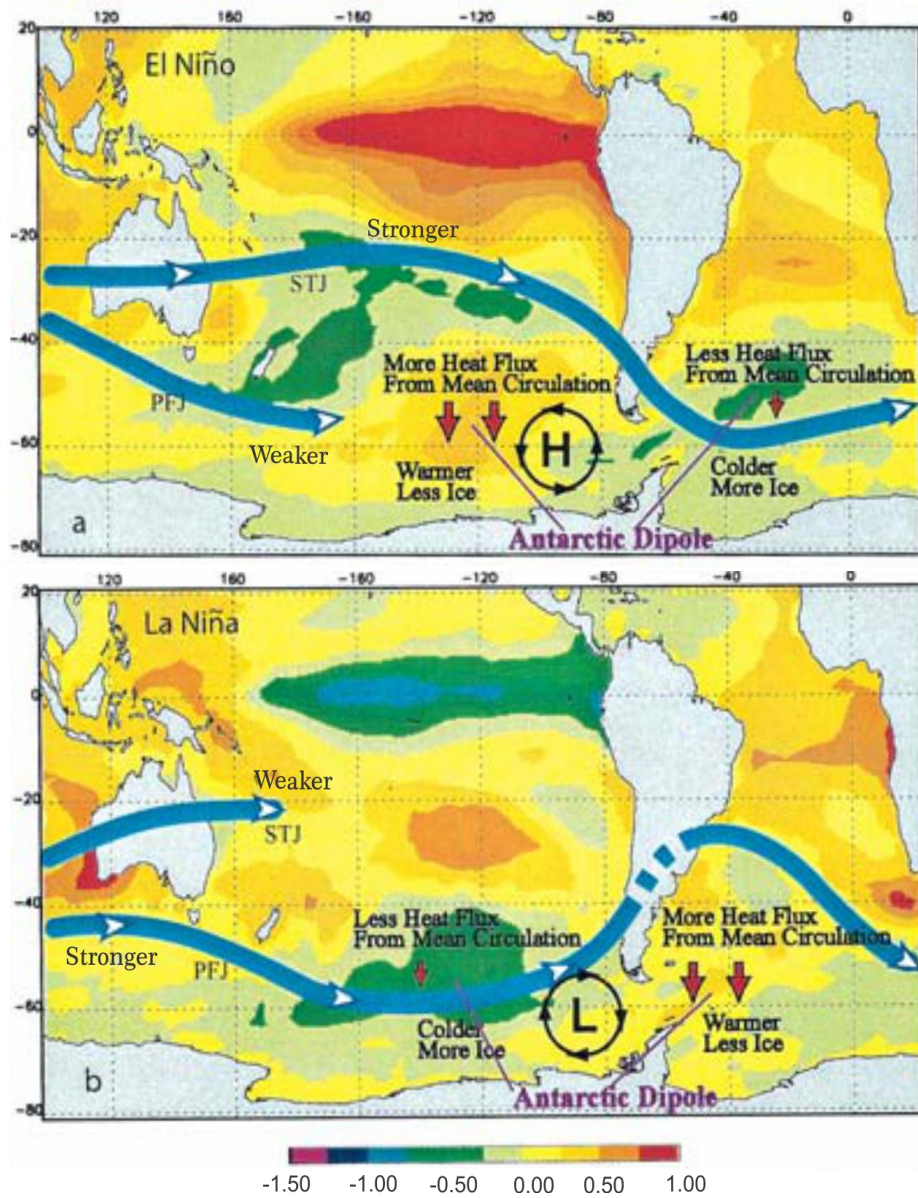


Figure 2.7: Sea surface temperature composites ( $^{\circ}\text{C}$ ) for El Niño and La Niña conditions showing the position and strength of the subtropical jet stream (STJ) and polar front jet (PFJ), resultant pressure anomalies and movement of air cold/warm air masses (modified from Yuan et al., 2004).

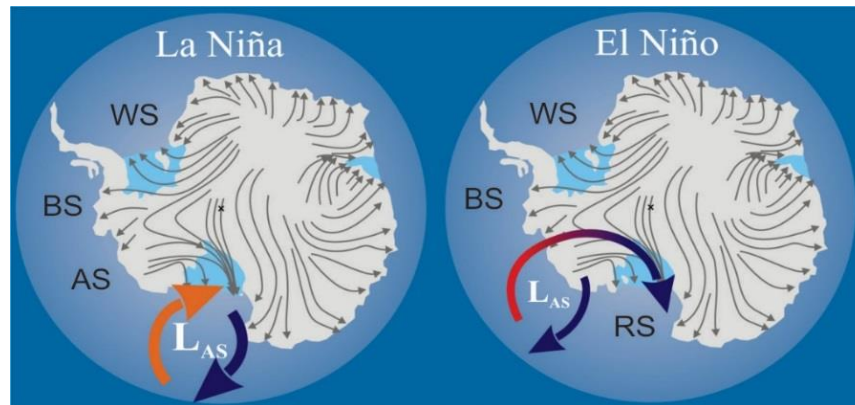


Figure 2.8: Schematic diagram showing the east-west movement of the Amundsen Sea Low ( $L_{AS}$ ) during La Niña/El Niño. Blue arrows represent cooler air flow while red arrows indicate flow of warmer air masses. Size and thickness of the arrows indicates strength of the  $L_{AS}$ . The grey arrows indicate katabatic wind flow (modified from Bertler et al., 2006). WS: Weddell Sea; BS: Bellingshausen Sea; RS: Ross Sea.

### 2.6.3 SAM and ENSO coupling

Statistically significant correlations between ENSO and the SAM and the extent of Antarctic sea ice are identified from comparison of satellite-derived sea ice data and climatological indices. These correlations show that the last four decades have seen a general increase in covariability between ENSO and the SAM (El Niño co-occurring with negative SAM, La Niña with positive SAM), particularly during austral spring and summer (Fogt and Bromwich, 2006; Stammerjohn et al., 2008; Fogt et al., 2011; Pezza et al., 2012). La Niña years with a positive SAM present the most favourable conditions for overall Antarctic sea ice growth. This relationship implies that SAM and ENSO act in synergy to produce the sea ice anomalies, although the original forcings for the two climatic modes are quite different. This association has been tested in Adélie Land by Gregory (2012) who correlated ENSO and SAM indices with sea ice concentrations in the region from 1978-2008. It was found that there is a moderate (95% confidence) negative correlation ( $r=-0.368$ ,  $n=30$ ) between the SOI, the SAM index and sea ice concentrations (i.e. negative SAM and positive SOI [La Niña] values correlate to reduced sea ice), which is particularly evident in the spring period.

There is no general agreement on which of the two modes has a greater influence on Antarctic sea ice and whether a forcing mechanism exists between the two (Pezza et al., 2012). An eventual reversal in the positive Southern Hemisphere sea ice trends is projected by most

climate models as a result of anthropogenic-induced climate change, even if the projected trends in ENSO and SAM remain unchanged (Sen Gupta et al., 2009).

## 2.7 Site Summary

Site U1357 is located in the Dumont d'Urville Trough, ~35 km offshore (Figure 2.9). The Adélie Land region is dissected by several glaciers which may contribute terrigenous sediment into the coastal zone with the core site located 40 km to the north of the Astrolabe Glacier, and ~75 and 300 km northwest of the Zéléé and Mertz glaciers respectively. Presently, sea ice covers the core site 7-9 months of the year with more open marine conditions existing during the Austral summer between January and March (Arrigo and van Dijken, 2003). Sea ice advances rapidly from April to June, reaching its maximum extent between July and September, then retreats slowly during spring melting attaining its minimum extent in February. The site is located within the Dumont d'Urville polynya (139.31°E, 66.11°S) during the summer season which has an area of 13,020 km<sup>2</sup>. However, in winter only a small portion of the polynya (960 km<sup>2</sup>) remains ice-free to the north-west of the core site. U1357 is also directly downwind and downcurrent of a much larger polynya system to the east – the Mertz Glacier polynya (MGP; 144.04°E, 66.37°S) which has a winter area of 5,900 km<sup>2</sup> (Arrigo and van Dijken, 2003).

The Adélie Land coast is influenced by several water masses (Figure 2.9) (Rintoul, 1998; Bindoff et al., 2000, Williams and Bindoff, 2003; Williams et al., 2008): (1) Antarctic Surface Water (AASW), a relatively fresh surface layer on the continental shelf which flows westwards via the Antarctic Coastal Current (AACC); (2) Modified Circumpolar Deep Water (MCDW), a variety of Circumpolar Deep Water which has mixed with AASW while upwelling from the deep ocean onto the continental shelf; (3) Dense Shelf Water (DSW) which forms through brine rejection during sea-ice formation and flows down the continental shelf as cascading plumes or gravity currents, but is not dense enough to contribute to Adélie Land Bottom Water (ALBW) formation; (4) High Salinity Shelf Water (HSSW), the densest, saltiest of the shelf water masses formed through brine rejection during sea-ice formation and cooling of the MCDW, flows northward down the continental slope and is modified to become part of ALBW; (5) Ice Shelf Water (ISW), formed by interaction of HSSW water with the undersides of floating ice tongues (most notably the Mertz Glacier Tongue).

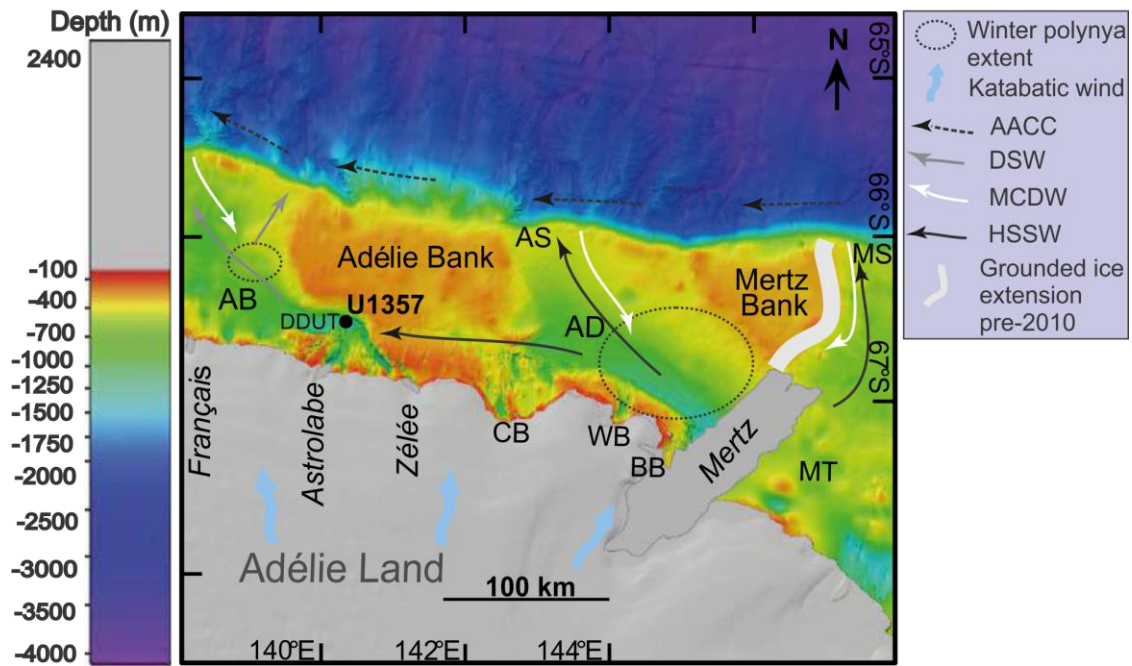


Figure 2.9: Bathymetric map of the Adélie Land region modified from Beaman et al. (2011) showing: winter extent of the Dumont d'Urville and Mertz polynyas; detail of oceanographic currents: Antarctic Coastal Current (AACC); different water masses: Dense Shelf Water (DSW); Modified Circumpolar Deep Water (MCDW); High Salinity Shelf Water (HSSW) and katabatic wind directions. Major glaciers are indicated in italics; coastal bays: Commonwealth (CB); Watt (WB); Buchan (BB); bathymetric features: Adélie Basin (AB); Adélie Depression (AD); Adélie Sill (AS); Mertz Sill (MS); Mertz Trough (MT).

## 2.8 Antarctic Bottom Water formation and ocean circulation offshore Adélie Land

### 2.8.1 Bottom water formation in Antarctica

The main formation centres of AABW in Antarctic coastal waters occur in four distinct regions, the Weddell Sea, the Ross Sea, Mac.Robertson Land, and the Adélie Land coast in East Antarctica (Rintoul, 1998; Ohshima et al., 2013). The Adélie Land coast is supplied by two sources of AABW, which both later drain into the Australian Antarctic Basin. The relatively warmer and more saline Ross Sea Bottom Water (RSBW), which is advected into the region via the easterly Antarctic Slope Front Current, and the colder, fresher, more oxygen-rich Adélie Land Bottom Water (ALBW) that is formed locally in the region (Figure 2.10) (Rintoul, 1998, Fukamachi et al., 2000; Williams et al., 2008). Most recent volumetric estimates of AABW summarised by Meredith (2013) reveal that the Weddell, Adélie, Ross and Mac. Robertson Land sources are respectively 40%, 30%, 20% and 10% by volume making the Adélie

Land coast the second largest formation region. ALBW formed offshore Adélie Land is therefore an important contributor of bottom water to the meridional overturning circulation—a north-south directed system of surface and deep currents encompassing all ocean basins which together with the ACC transport heat, gas, salt and nutrients around the world (Jacobs, 2004; Carter et al., 2008).

AABW is typically formed by overflows of HSSW at the shelf break. These flows mix with AASW (produced locally and advected from the Ross Sea region), MCDW and sometimes ISW to create modified shelf water (MSW), which is dense enough to be transported down the continental slope to the abyssal ocean (Rintoul, 1998, Bindoff et al., 2000; Jacobs, 2004). In the Weddell and Ross seas, the cooling and freshening influence of melting beneath the large ice-shelves together with brine expulsion from sea ice during winter, are essential for export of HSSW and thus AABW production in those regions (Smethie and Jacobs, 2005; Orsi and Wiederwohl, 2009). The Adélie Land coast has no continental ice-shelves and the main source of AABW are discrete coastal polynya regions where HSSW forms due to brine-rejection from enhanced sea ice production (Rintoul, 1998; Bindoff et al., 2000).

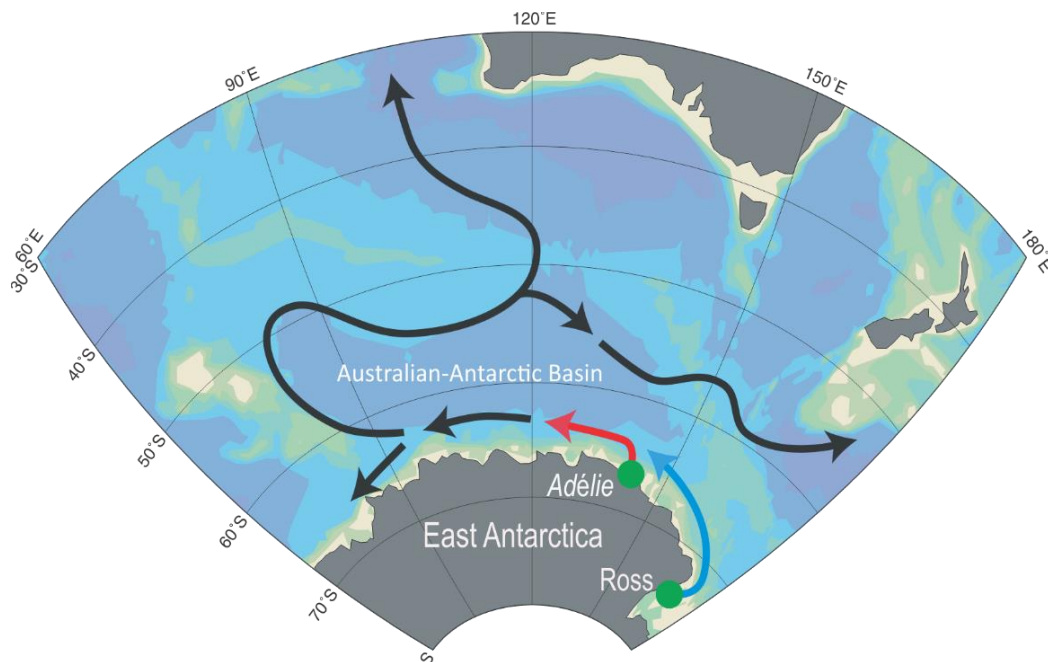


Figure 2.10: Large-scale map of the East Antarctic sector of the Southern Ocean with major Antarctic Bottom Water pathways: Ross Sea Bottom Water (RSBW) (blue); Adélie Land Bottom Water (ALBW) (red); and RSBW/ALBW mixture. Modified from Rintoul (2007).

## 2.8.2 Bottom Water Formation offshore Adélie Land

In winter, the Dumont d'Urville and Mertz Glacier polynyas are maintained by particularly strong katabatic winds in the region that freeze the surface waters and advect newly formed ice away from the coast, continually creating space for further sea ice production (Adolphs and Wendler, 1995; Wendler et al., 1997b). While polynya size depends on wind direction and strength, it is also greatly influenced by blocking features that can form barriers to ice advection (Massom et al., 2001). Until 2010, the much larger size and extent of the Mertz Glacier polynya, compared to the Dumont d'Urville polynya, was attributed to the Mertz Glacier floating ice tongue, and associated grounded icebergs on the Mertz Bank (Figure 2.9), which provided a barrier to the westward advection of sea ice associated with the Antarctic Coastal Current (Massom et al., 2001; Williams et al., 2008). Each winter, fast ice formed between the grounded icebergs on the Mertz Bank to the north of the Mertz Glacier ice tongue and significantly increased the length of this barrier to near the shelf break (Lytle et al., 2001).

In February 2010, the Mertz Glacier underwent massive calving after a collision with an iceberg which removed 80% of the Mertz Glacier ice tongue, leaving only a 20 km-long stub (Young et al., 2010; Tamura et al., 2012). Iceberg calving has been proven to alter polynya dynamics and decrease HSSW production as found by Nøst and Østerhus (1998) following calving of icebergs from the Filchner Ice Shelf in the Weddell Sea.

Following the calving event, Tamura et al. (2012) used remote sensing data and atmospheric analyses to calculate that the total sea ice production for the region in the winter of 2010 (2011) was reduced by 14% (20%) relative to the 2000-2009 mean. This finding supports model simulations by Kushara et al. (2011b) who also suggested that the reduced sea ice formation decreased the export of dense shelf water by 23% in the following year. Observational studies by Shadwick et al. (2013) and Lacarra et al. (2014) confirm that the salinity and density of dense shelf water declined abruptly after the calving event, consistent with a reduction of sea ice formation in the polynya. However, the 23% reduction in dense shelf water formation estimated by Kushara et al. (2011b) is about the same amount as the interannual variability found in pre-calving ice-ocean simulation models by Marsland et al. (2004) and Kushara et al. (2011a). In addition, recent observations of local sea ice conditions by Campagne et al. (2015) found a ~70 year periodicity in at least the last 250 years associated with large calving events of the Mertz Glacier, suggesting that long-term AABW production in

the region experiences a fairly large variability. Modelling studies suggest that the interannual variability and long-term AABW formation is expected to weaken in response to surface water freshening and warming as future atmospheric and oceanic temperatures rise (Marsland et al., 2007). After the Mertz Glacier calving event and reduction of Mertz Glacier polynya, reduced sea ice and dense shelf water production over the Adélie Depression was estimated to be partially compensated by the new production over the area formerly occupied by the Mertz Glacier ice tongue (Tamura et al., 2012; Lacarra et al., 2014).

### 2.8.3 Circulation of water masses offshore Adélie Land

Prior to the calving of the Mertz Glacier ice tongue several transect and mooring station observations were made offshore Adélie Land to collect temperature, salinity and velocity data in order to define water masses and their circulation. Using the definition of key water masses as defined by Whitworth et al. (1998) (Figure 2.11b) Rintoul (1998) analysed hydrographic data between 138°E and 165°E and showed that most stations on the continental shelf and slope were characterised by a benthic plume of dense shelf water. Rintoul and Bullister (1999) also noted such a plume at 136.43°E, 64.93°S on the continental shelf at ~900 m water depth which extended from the shelf break, but was not dense enough to reach the sea floor on the continental rise. Rintoul (1998) identified the Adélie Depression situated above the Mertz Glacier polynya and the Mertz Glacier ice tongue as a location with shelf waters high enough in salinity and density in order to reach the sea floor and contribute to ALBW formation. In addition, the Adélie Depression was the only site where intrusions of MCDW were identified which act to enhance shelf water salinities.

Table 1: Mean and standard deviation values of current meter data at Mooring C (139.5°E, 65.1°S) collected for two time periods in 1994-1995. Season variability is remarkable only at the current meter near the bottom. Adapted from Fukamachi et al. (2000).

Depth (m)	Period	Speed (cm s <sup>-1</sup> )		Temperature (°C)	
		Mean	Standard Deviation	Mean	Standard Deviation
1075	Jan-Jul	4.6	3.5	0.81	0.09
1075	Aug-Dec	6.4	4.8	0.76	0.09
1778	Jan-Jul	4.4	2.5	0.16	0.06
1778	Aug-Dec	5.8	3.1	0.13	0.06
2632	Jan-Jul	14.1	3.4	-0.28	0.08
2632	Aug-Dec	19.8	6.2	-0.55	0.13

Temperature and velocity measurements analysed by Fukamachi et al. (2000) from a mooring station at 139.5°E, 65.1°S on the continental slope to the north of the U1357 site (Figure 2.11a) support the Adélie Depression as being the primary source of ALBW. Measurements show that temperature and velocity near the bottom are not correlated well with those from intermediate depths indicating that the lower temperature and faster speed is not caused by deep convection at the mooring site, but rather ALBW transport from the Adélie Depression (Table 1). Winter and year-round observations of water mass properties in the Adélie Depression and Adélie Sill confirm the Adélie Depression as the source of dense shelf water capable of forming ALBW, with the Adélie Sill acting as the export pathway of these waters into the abyssal ocean (Williams and Bindoff, 2003; Williams et al, 2008). The flow direction was observed to align with bathymetry with a mean northward flow of 10  $\text{cms}^{-1}$  just above the sill depth and a mean zonal flow at near zero  $\text{cms}^{-1}$ . Williams et al. (2010) also identified the Mertz Depression as a significant contributor to the total dense shelf water export. The overall system was described as a “conveyer belt” transporting MCDW into the depressions along the western side of Metz Bank and east of Mertz Sill where mixing with AASW and HSSW occurs, and a return flow of this modified shelf water along the coast and out through the Adélie and Mertz sills (Figure 2.11a). An ice-ocean modelling study within the Adélie and Mertz depressions by Kusahara et al. (2011a) showed a similar circulation pattern. The export of modified shelf water from the depressions is greatest in winter due to enhanced brine rejection in the Mertz Glacier polynya inducing convection in the upper water column. In summer, water column restratification results in a decrease of HSSW production which increases the influence of MCDW allowing these intrusions to penetrate further southward into the depressions (Williams et al., 2008; 2010).

In the Dumont d’Urville Trough, intrusions of MCDW were thought to be non-existent (Rintoul, 1998; Bindoff et al., 2000; Fukamachi et al., 2000). However, recent summer observations by Lacarra et al. (2011) showed that MCDW penetrates into the trough reaching maximum depths of 1200 m. Water masses at the base of Dumont d’Urville Trough are warmer and fresher than HSSW in the Adélie depression indicating that the dense shelf water formed in this depression does not contribute directly to ALBW formation. In contrast, waters at the base of the Adélie Depression display a HSSW signature consistent with export of modified shelf water and ALBW formation in summer (Lacarra et al., 2011).

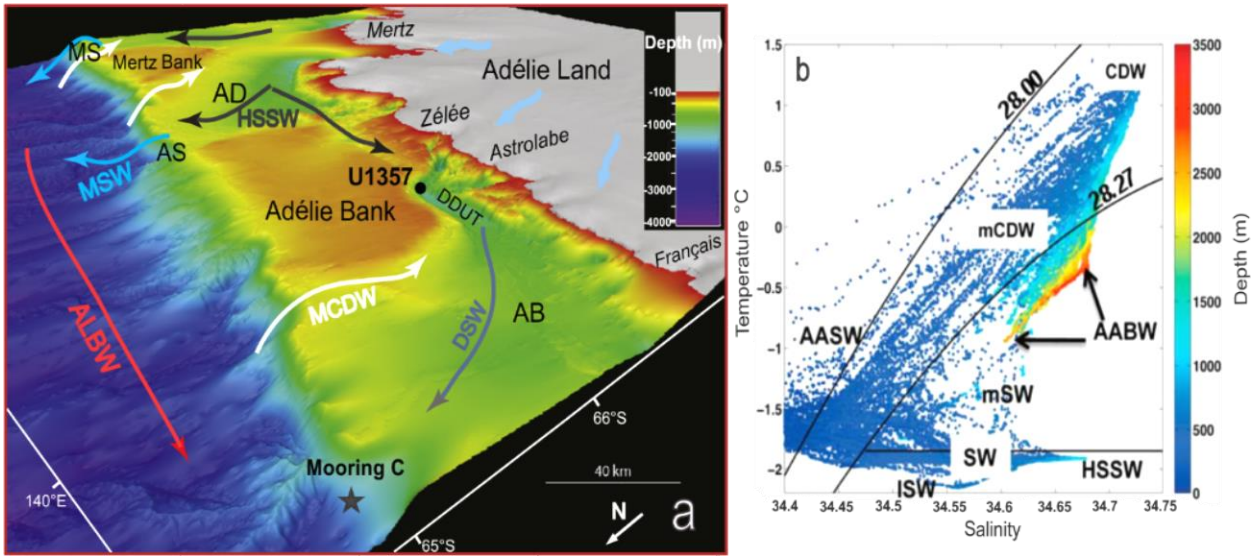


Figure 2.11: (a) Bathymetric map of the study area (modified from Beaman et al., 2011) showing the flow of different water masses in the region indicated by arrows positioned offshore; katabatic winds (light blue arrows on land); major glaciers in italics; bathymetric features: Adélie Basin (AB); Dumont d'Urville Trough (DDUT); Adélie Sill (AS); Adélie Depression (AD); Mertz Sill (MS); location of U1357 core site and Mooring C from Fukamachi et al. (2000). (b) T-S data from Williams et al. (2010) showing key water masses as defined by Whitworth et al. (1998). Main water masses include: Circumpolar Deep Water (CDW); Modified CDW (MCDW); Antarctic Surface Water (AASW); Shelf Water (SW); Ice SW (ISW); Modified SW (MSW); High Salinity SW (HSSW) and Antarctic Bottom Water (AABW). The two black curves indicate neutral density surfaces ( $\text{kgm}^{-3}$ ).

## 2.9 Holocene climate in Antarctica

The long-term climate history of Antarctica during the Holocene is largely attributed to Earth's orbital changes, most notably precession (~19,000-21,000 year cycle), which alters the timing of the seasons. Orbital variations alter when the poles and the equator receive maximum solar insolation, and thus the latitudinal insolation gradient, and seasonal duration and intensity (Vimeux et al., 2001; Lorenz et al., 2006; Davis and Brewer, 2009). It is hypothesized that the long-term Holocene cooling of Antarctica may be the consequence of decreasing local (i.e. Southern Hemisphere) summer duration through the Holocene (Huybers and Denton 2008; Shevenell et al., 2011), independent of linkages with the Northern Hemisphere high latitudes on orbital timescales as previously suggested (Steig et al., 1998; Nielsen et al., 2004). However, lags or non-linear responses of global climate to these orbital changes are believed to be the consequence of various feedbacks between the atmosphere, sea ice and ocean regimes (i.e. shifting of zonal winds, changes in the carbon cycle, changes in the overturning

oceanic circulation) and thermal inertia of the climate systems (Bentley et al., 2009 and references therein).

### 2.9.1 Long-term Holocene trends in East Antarctica

Environmental reconstructions based on ice cores (Masson et al., 2000; Masson-Delmotte et al., 2011), marine sediments (Hodell et al., 2001; Presti et al., 2003; Nielsen et al., 2004; Crosta et al., 2007) and terrestrial records (Verleyen et al., 2011) reveal that generally East Antarctica shows four contrasted climatic intervals during the Holocene reported as evolving from: (1) a warm early Holocene between ~11.7-9 ka; (2) a cool event between ~9-8 ka; (3) a warm mid-Holocene between ~8-4 ka, but which also occurs between 7-5 kyr for the Ross Sea sector and between 6-3 ka for some East Antarctic sites; and (4) a cold Neoglacial from 4-3 ka to the present day. Some East Antarctic sites show a cooling from ~6.5 to 4 ka (Cremer et al., 2003; Wagner et al., 2004) and a warming between ~4 and 2 ka (Kirkup et al., 2002; Maddison et al., 2012). These climatic periods are not always synchronous in the different regions of Antarctica due to the different resolutions of the proxies used, dating uncertainties and the spatial heterogeneity in the intensities of the local and external forcing mechanisms (Masson et al., 2000; Verleyen et al., 2011).

### 2.9.2 Millennial to centennial Holocene variability in East Antarctica

A synthesis of eleven deuterium Antarctic ice core records (Figure 2.12), which have been interpreted to represent changes in air temperature, reveals nine aperiodic millennial-scale oscillations superimposed on the long-term Holocene trend (Masson et al., 2000). The average duration of warm events is ~1450 years for East Antarctica and ~1250 years in the Ross Sea sector (Figure 2.13). The succession of these climatic episodes has been suggested to be potentially tied to internal oscillations of the climate system produced by changes in the Northern (Bond et al., 1997; Bianchi and McCave, 1999) and Southern Hemisphere (Pierce et al., 1995) meridional overturning circulation (Masson et al., 2000).

Recently it has been proposed that the millennial-scale Holocene warm and cold events result from increased and decreased westerly wind strength/influence, based on SST proxies ( $TEX_{86}$ ,  $\delta^{18}O_{\text{planktic}}$ ) recovered from sediment cores off the coast of Australia and Antarctic Peninsula (Moros et al., 2009; Shevenell et al., 2011). Increased westerly influence in the Southern Ocean enhances  $CO_2$  ventilation from deeper waters and CDW upwelling, thereby promoting

early sea ice retreat leading to a rise in atmospheric temperatures. Conversely, weakened westerly wind influence reduces CDW upwelling which leads to later sea ice retreat and lower temperatures. This hypothesis is supported by westerly winds and CO<sub>2</sub> variability reconstructions from western Patagonia, South America, based on a suite of terrestrial ecosystem proxies (Moreno et al., 2010).

All of the ice core records also exhibit a high-frequency variability in the multidecadal mode (70-240 years) characteristic of internal oscillations most likely caused by solar variability (Masson et al., 2000).

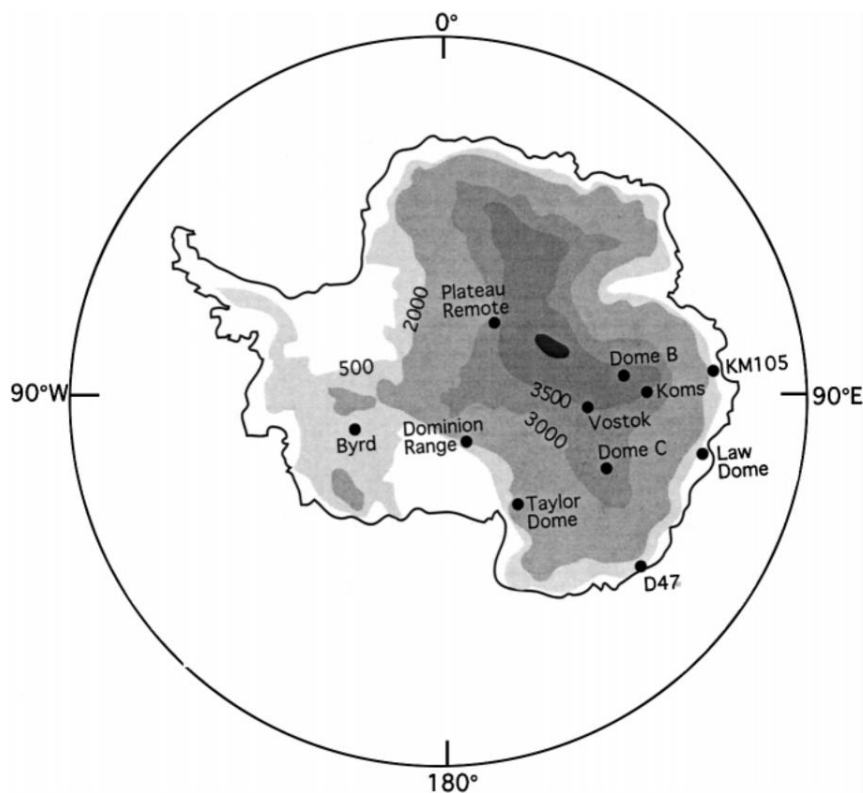


Figure 2.12: Map of Antarctica showing the location of ice cores used in Masson et al. (2000). Darker shading indicates higher elevation. Adapted from Masson et al. (2000).

Growing paleoclimatic evidence suggests that the climatic signals of Medieval Warm Period and the Little Ice Age events can be detected around the world (Mayewski et al., 2004; Bertler et al., 2011). The Little Ice Age and Medieval Warm Period are typically considered to be Northern Hemisphere climate phenomena of colder conditions between the 15<sup>th</sup> to mid-19<sup>th</sup> (Grove, 2013) century and warmer climatic conditions between 9<sup>th</sup> to 13<sup>th</sup> century (Hughes,

1994), respectively. Their reconstructions show highly variable patterns with marked regional differences, therefore the causes for these events are still debated between changes in solar output, increased volcanic activity, shifts in zonal wind distribution, and changes in the meridional overturning circulation (Crowley, 2000; Hunt, 2006). Detection of the equivalent of these events in Antarctica is thus important for understanding climate variability and its transmission between the two hemispheres. Masson et al. (2000) identified a warm event at ~1000 years followed by a cool event in East Antarctic ice cores (Figure 2.13). Geochemical proxies from Siple Dome ice core in the northwest of West Antarctica show that the L<sub>AS</sub> and westerly winds were stronger during the Little Ice Age but weaker during the Medieval Warm Period (Kreutz et al., 2000; Mayewski and Maasch, 2006).

Similar analyses of two ice cores drilled in the western Ross Sea sector infer ~2°C cooler SSTs, increased sea ice extent and stronger katabatic winds ( $\geq 55 \text{ ms}^{-1}$ ) during the Little Ice Age, and slightly warmer SSTs and reduced sea ice extent in the Ross Sea coincident with the timing of the Medieval Warm Period in this region (Bertler et al., 2011; Rhodes et al., 2012). During the inferred Antarctic Little Ice Age, the Ross Sea polynya experienced greater primary production and polynya extent due to stronger katabatic winds which may have acted to enhance sea ice production and AABW formation (Leventer and Dunbar, 1988; Bertler et al., 2011). Slightly colder than average temperatures, coincident with the Little Ice Age, were also detected from a 300 m borehole at the West Antarctic Ice Sheet Divide (Orsi et al., 2012). However, evidence for these climatic events is lacking in East Antarctica due to lower resolution records (Verleyen et al., 2011).

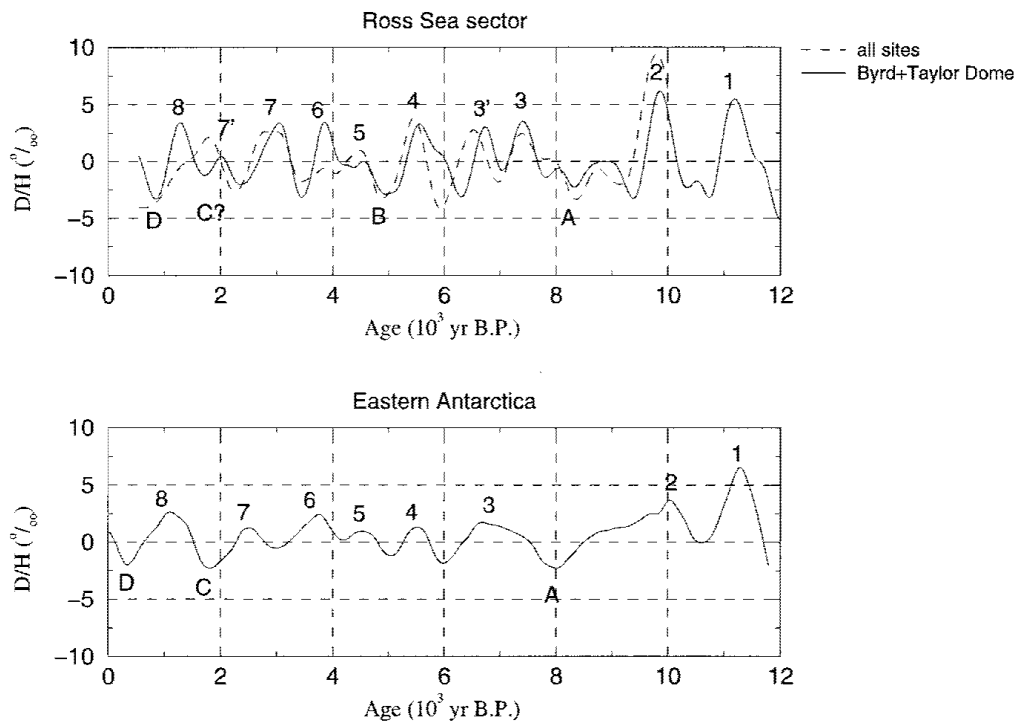


Figure 2.13: Common millennial-scale variability calculated from eleven ice core records in Masson et al. (2000). Curves are detrended and filtered in the millennial periodicities. Numbers 1-8 represent warm events, letters A, C, D represent cold events.

### 2.9.3 Holocene Climate Variability offshore Adélie Land

To date, limited research has been carried out on Holocene climate variability offshore Adélie Land. Interpretations of variations in sea ice extent, stratification, paleoproductivity and sedimentary input have been derived from diatom assemblages, grain size and geochemical proxies retrieved from sediment cores discussed in Section 2.4 (Figure 2.14). Based on these proxies, Holocene climate offshore Adélie Land has been separated into four distinct periods defined by warmer conditions from ~11.5 to 9 ka, cooler conditions between ~9 and 7.7 ka, warmer conditions between ~7.7 and 4 ka and cooler conditions from ~3.9 to 1 ka (Crosta et al., 2008; Denis et al., 2009a; Crespin et al., 2014). Figure 2.14 summarises the available literature of Holocene environmental change in the region.

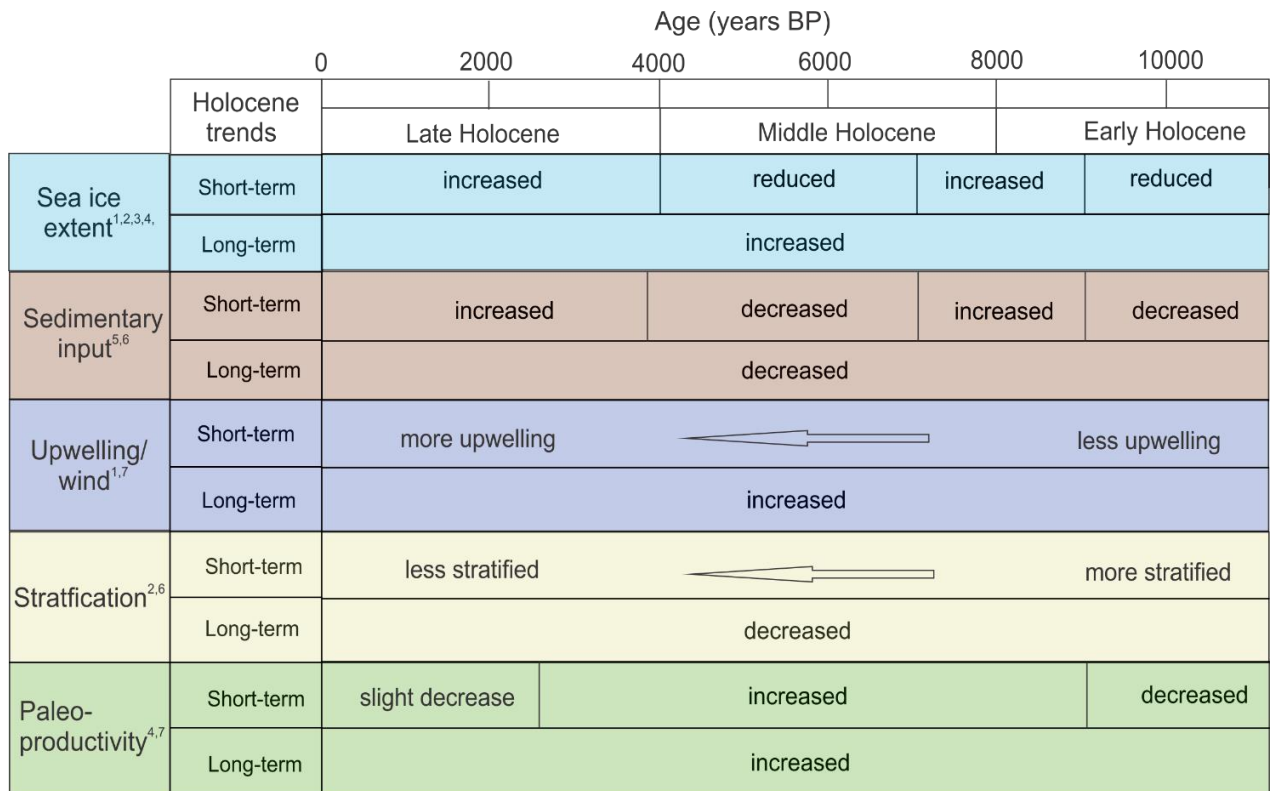


Figure 2.14: Summary figure of climate variability along the Adélie Land coast for the past 11,500 years. Superscript number refers to the original publication; <sup>1</sup>Denis et al. (2010); <sup>2</sup>Crosta et al. (2008); <sup>3</sup>Crosta et al. (2007); <sup>4</sup>Panizzo et al. (2014); <sup>5</sup>Denis et al. (2009a); <sup>6</sup>Crespin et al. (2014); <sup>7</sup>Denis et al. (2009b).



## Chapter 3: Methodology

### 3.1 Core recovery and drilling disturbance issues

IODP Site U1357 consists of three cored holes (U1357A, U1357B and U1357C) (Escutia et al., 2011). This triple coring strategy is commonly employed by IODP so that in the case of incomplete recovery in one hole, a complete composite “spliced” section could be constructed from additional holes. However, the extremely high biogenic opal content of the cores compromised the development of a spliced record as the physical properties data (e.g magnetic susceptibility, density) were at, or near to, instrumental noise levels (Escutia et al., 2011). An additional complication is that most cores contained sediments that vigorously degassed methane (CH<sub>4</sub>) and hydrogen sulphide (H<sub>2</sub>S) upon decompression, causing expansion of the sediment sections and loss of sediment from the base of each core run. Consequently, this gas expansion makes identifying original stratigraphic depth difficult, and three separate depth scales have been applied to the core (Figure 3.1).

The shipboard data (physical properties, lithostratigraphic description, line-scan photos) all use the CSF-A depth scale (core depth below seafloor), which is measured from the total core length (added to the top depth of each subsequent 9.5 m core run) and including any expansion. In holes U1357A, U1357B and U1357C, core recovery was recorded as 99%, 101% and 107%, respectively. This has the implication that where an individual core run has greater than 100%, there are overlapping depths between the bottom of one run and the top of the next core run in the CSF-A scale. This can be corrected by using the standard IODP-based CSF-B depth scale, which compresses the recovered interval back to 100% for each core run, if it exceeded this value in the CSF-A scale. If the CSF-B scale is used, recovery rates drops to 96%, 98% and 100% in holes A, B and C, respectively, though this does not correct for the discrete voids, which requires an additional correction prior to rescaling.

Visual examination of the core face suggests gas expansion effectively took two forms: 1) pervasive, uniform expansion characterised by mm-scale gaps gas pockets throughout the length of the core face; and 2) discrete gaps in the core sections, termed herein as voids. To correct for this, any void exceeding 1 cm was logged and the thicknesses of these voids were subtracted from the CSF-A depth at the top of each core run (this analysis was conducted independently by R. McKay (VUW) and will be presented in detail in Dunbar et al., in prep).

The new depth was then scaled back using the same method as a CSF-B scale –i.e. the length of the core was linearly compressed back to 100% recovery if it still exceeded that value after the “devoiding”. Using this devoided depth scale (herein termed CSF-D), recovery rates dropped to 93% and 90% for holes A and B, respectively (Hole U1357C was not devoided as it was a shorter section, and had whole round sampling prior to logging, so the location of voids is difficult to characterise). This approach assumes that the majority of lost core resulted from sediment being “pushed” out of the base of the piston core by gas expansion during the recovery of each core run, hence, the approach to “lock” the top of each core run to the original CSF-A scales, and rescaling depths below this. The maximum difference in depth-scale between the CSF-B and CSF-D scale is 0.91 m and 1.66 m for holes A and B, respectively. Given the scale of this error, and the high sedimentation in this core (~1.5 cm/yr), this correction is essential for time series analysis presented in this thesis investigating high frequency cycles of <100 years (Dunbar et al., in prep).

A number of cores from holes U1357A and U1357C ruptured due to the gas pressure but no cores from U1357B ruptured, and therefore U1357B forms the main basis for this research. The total core length recovered from hole U1357B was 170.7 m at a water depth of 1028 m.

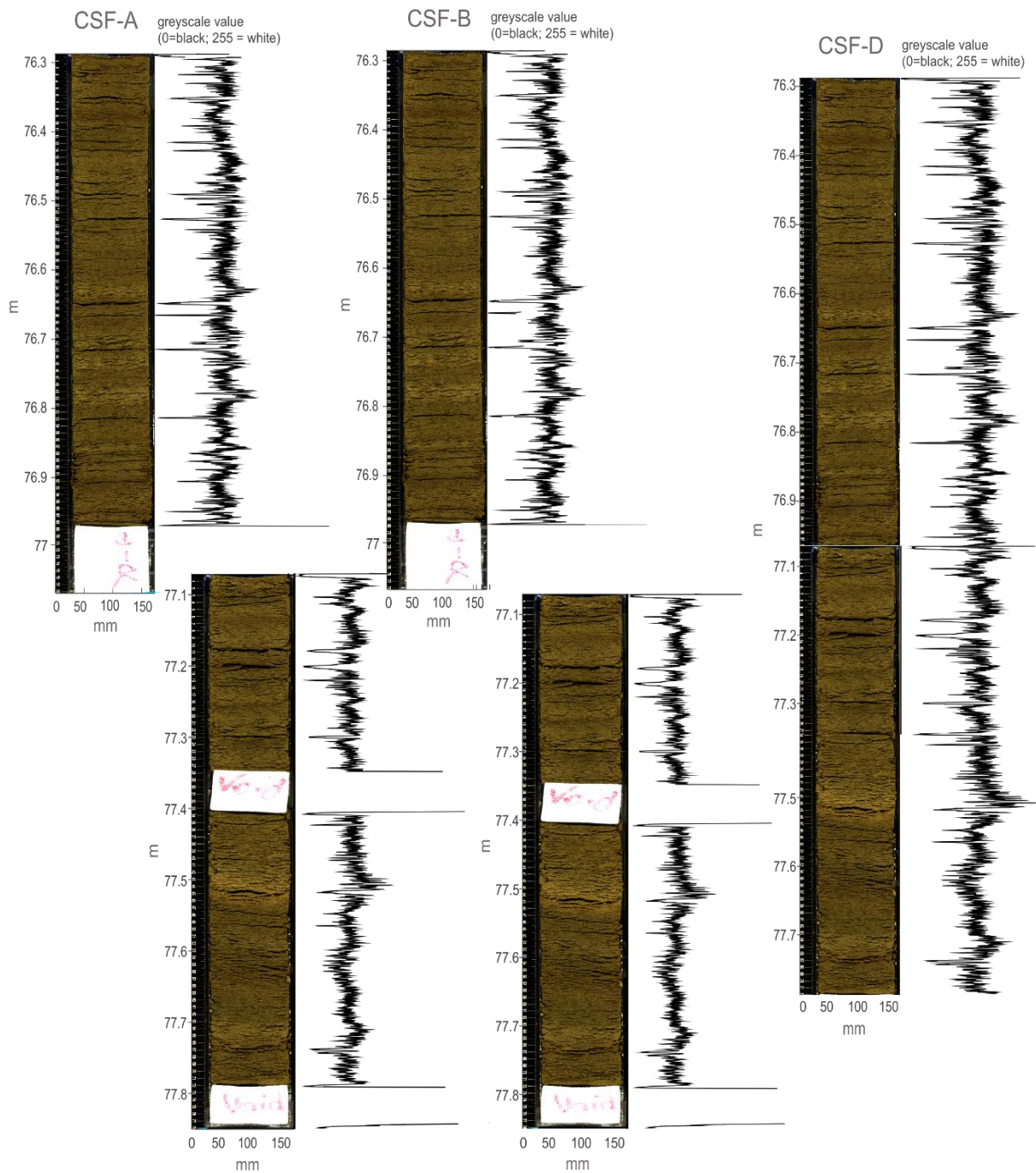


Figure 3.1: Schematic example of the three depth scales used in this study. (Left) In CSF-A depth scale, two separate cores are shown, and due to gas expansion after drill core recovery, recovery exceeds 100% and the depths (in mbsf), as measured during drilling, now overlap. (Centre) To correct for this, the standard IODP procedure applies a linear compression algorithm which is based on the assumption that expansion is uniform in the core. In U1357, expansion is present as discrete voids (noted as white foam infill in the photos for CSF-A and CSF-B. (Right) For the CSF-D scale, the voids are removed and the depth scale is adjusted prior to linear compression being applied (if recovery still exceeds 100%). This allows a continuous time series to be studied from these two core runs (as shown in the greyscale curves to the right of each photo).

### 3.2 Core Lithostratigraphy

The sediments were described by the shipboard party to consist of three distinct lithologic units. The uppermost Unit I (0-159.26 m in CSF-A) consists of laminated diatom ooze defined by repetitions of dark olive-brown and light green-brown laminae, initially interpreted to represent seasonal couplets of summer and following spring deposition, respectively. Laminae are generally defined as  $\leq 1$  cm thickness. For conciseness, this term is also used for any thin beds of 1-3 cm thickness in this thesis. Individual laminae range in thickness from  $<0.5$  to 3 cm and extend throughout the entire section. The diatom ooze is principally composed of diatoms, although silicoflagellates, radiolaria, foraminifera and fish bones are also present. Unit II (159.26-170.77 m in CSF-A) consists of sand and silt-bearing diatom ooze with distinct laminations as well as layers of structureless diatom-rich sandy silt. The boundary between Units I and II is marked by an abrupt increase in silt and sand content, and the presence of dispersed gravel clasts, and is interpreted to be a glacial retreat facies (Escutia et al. 2011). The basal Unit III, is a poorly sorted diamict that was only cored (by rotary coring methods) in U1357A (185-186.8 m in CSF-A), and is interpreted as the LGM till. Unit III was not recovered in U1357B, but is interpreted to be at or near the base of the cored interval, as the piston core refused to penetrate deeper than 170.77 mbsf (n.b. no rotary core was collected at the base of U1357B), and the thickness of Unit II in U1357B (11.51 m) is similar to that obtained in U1357A (15.35 m).

Units I and II contain large quantities of biogenic opal and organic biogenic detritus. Ship board inductively coupled plasma atomic emission spectroscopy measurements indicate  $\text{SiO}_2$  concentrations are high (76-91 wt%), accompanied by low concentrations of  $\text{CaCO}_2$  (1-3 wt%),  $\text{TiO}_2$  ( $\leq 0.3$  wt%) and  $\text{Al}_2\text{O}_3$  ( $\leq 6$  wt%), as expected for a nearly pure diatom ooze with some terrigenous input (Escutia et al., 2011).

### 3.3 Age Model

This thesis uses a preliminary age model that has been developed for core U1357B based on 87 <sup>14</sup>C analyses on bulk organic carbon taken from IODP 318 U1357B (Figure 3.2; Dunbar et al., in prep). This age model is preliminary and as it is currently unpublished, it may be subject to minor variation, although it is not anticipated to vary significantly (R. Dunbar, pers comm). The model was calibrated with a reservoir age correction of 1600±50 years and depth (in CSF-D) to age conversions achieved by using BACON. This is a Bayesian iteration scheme that invokes memory from dates above any given horizon, and produces a weighted mean and median age-depth curve (Blaauw and Christen, 2011). Unit III represents older glacial material that is not contiguous with the deglacial Holocene sediments, suggestive of a hiatus or reduced glacial deposition at the site, hence it was excluded from the age model. The top depth of 3 m (CSF-D) is consistent with the reservoir age in the Southern Ocean (Hall et al., 2010), indicating minimal sediment reworking, however this is expected to be more of an issue at the base of Unit II due to increased proximity to potential glacial influences during deglaciation.

The 170 dark and light laminae couplets were sampled at a ~1 m interval (a total of 340 samples), which represents an average of ~66 years between each couplet with a standard deviation of 33 years (a consequence of changes in sedimentation rate; see Appendix 1A for values). Note that the weighted mean age was used to display time in this thesis. Sample resolution calculated for the CSF-D depth scale is 0.95 m with a standard deviation of 0.42 m (see Appendix 1A). These samples are splits from samples collected by: Christina Riesselman (University of Otago) for diatom assemblages, stable isotopes ( $\delta^{13}\text{C}$  and  $\delta^{15}\text{N}$ ), and biogenic opal weight percent (BSi%); and by Dr. James Bendle and Kate Newtown (University of Birmingham, UK) for compound specific lipid biomarker analysis ( $\delta^{13}\text{C}_{\text{FA}}$  and  $\delta\text{D}_{\text{FA}}$ ) (see Section 3.8).

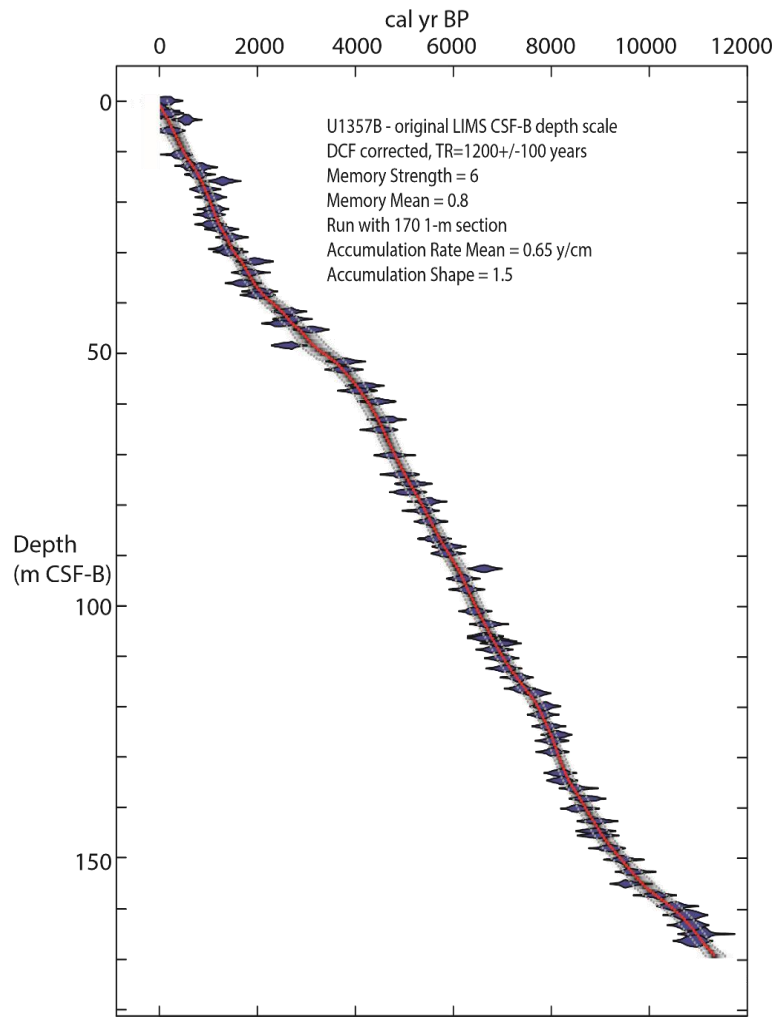


Figure 3.2: Age model for the U1357B core based on 87 radiocarbon analyses (Dunbar et al., in prep).

### 3.4 Data generated by this project

#### 3.4.1 Grain Size Analysis

A total of 349 samples were prepared for grain size analysis at Victoria University of Wellington following the method of Lewis and McConchie (2012). Samples were weighed (see Appendix 1B) before being treated for removal of biogenic opal with a 1M sodium hydroxide (NaOH) solution and incubated in a water bath at 80°C for 24 hours. This procedure was repeated twice due to an incomplete dissolution of diatoms observed in smear slides of randomly selected samples. The samples were then centrifuged three times with distilled water at 4700 rpm, before being treated with 27% hydrogen peroxide (H<sub>2</sub>O<sub>2</sub>) to remove organic material. Due to the high organic content of the sediment this procedure was carried

out in three stages to avoid sample loss as a result of very vigorous reactions. In stage one, the samples were treated with 5% H<sub>2</sub>O<sub>2</sub>, and in stages two and three with 10% and 27% H<sub>2</sub>O<sub>2</sub>, respectively. In each stage, samples were incubated in a water bath at 80°C for 24 hours. Between each stage, samples were centrifuged with distilled water for 10 minutes at 4700 rpm. Inspection of smear slides of randomly selected samples under an optical microscope after this step indicated that the majority of organic matter and diatoms had dissolved. However, broken fragments of sponge spicules remained and in rare instances wispy “spines” from diatoms also remained (Figure 3.4a). In this thesis, we assume that broken sponge spicules are part of the terrigenous fraction due to the advection of this material from the Mertz polynya (Denis et al., 2006), as sponges would not form a local benthos in the soft substrate at this site, and must be eroded and transported as suspended sediment from the seafloor upstream of the drillsite. The potential for the wispy “spines” of diatoms to influence the grain size distribution was assessed through the running of replicate samples (discussed below).

Prior to grain size analysis, samples were freeze dried, weighed and put into glass beakers. ~30 mL of 0.5 g/L Calgon (sodium hexametaphosphate) was added to the samples which were then sonicated and stirred for 15-20 minutes in order to disperse the grains and prevent clumping. Samples were measured using a Beckman Coulter LS 13 320 Laser Diffraction Particle Size Analyser (LPSA) at Victoria University of Wellington. The LPSA has a relatively narrow range of optimum obscuration which is determined by the sample surface area, in turn determined by sample concentration and sample distribution. The range in sample mass for most of the post-treatment samples varied from ~0.035-0.8 g and obscuration was sufficient enough for an aqueous liquid module to be used. Subsamples were taken from a total of 96 samples (selected on the basis of sufficient material being available from the treated sample) to test reproducibility of the data. Subsampling was conducted using the cone-and-quartering-method (Lewis and McConchie, 2012), which tries to ensure representative sub-sampling for the entire range of grain-sizes as the whole sample is mixed, heaped and then evenly divided into smaller quantities.

Random biases propagating through this process cannot be ruled out, especially when taking account of susceptibility of grains <10 µm to clump (McCave et al., 1995) and random cohesion of grains due to any remaining organic/biogenic content. Immediately prior to analysis and after sonication, samples were stirred by hand to keep sediment in suspension.

All of the samples were measured for 60 seconds and converted to size using the QuartzNatural.rf780d optical model, which assumes all material has a refractive index of quartz suspended in water. Standards were run at the start and end of each analysis session (i.e. morning and afternoon) and all samples were analysed at least twice to test the reproducibility of the instrument (Figure 3.3).

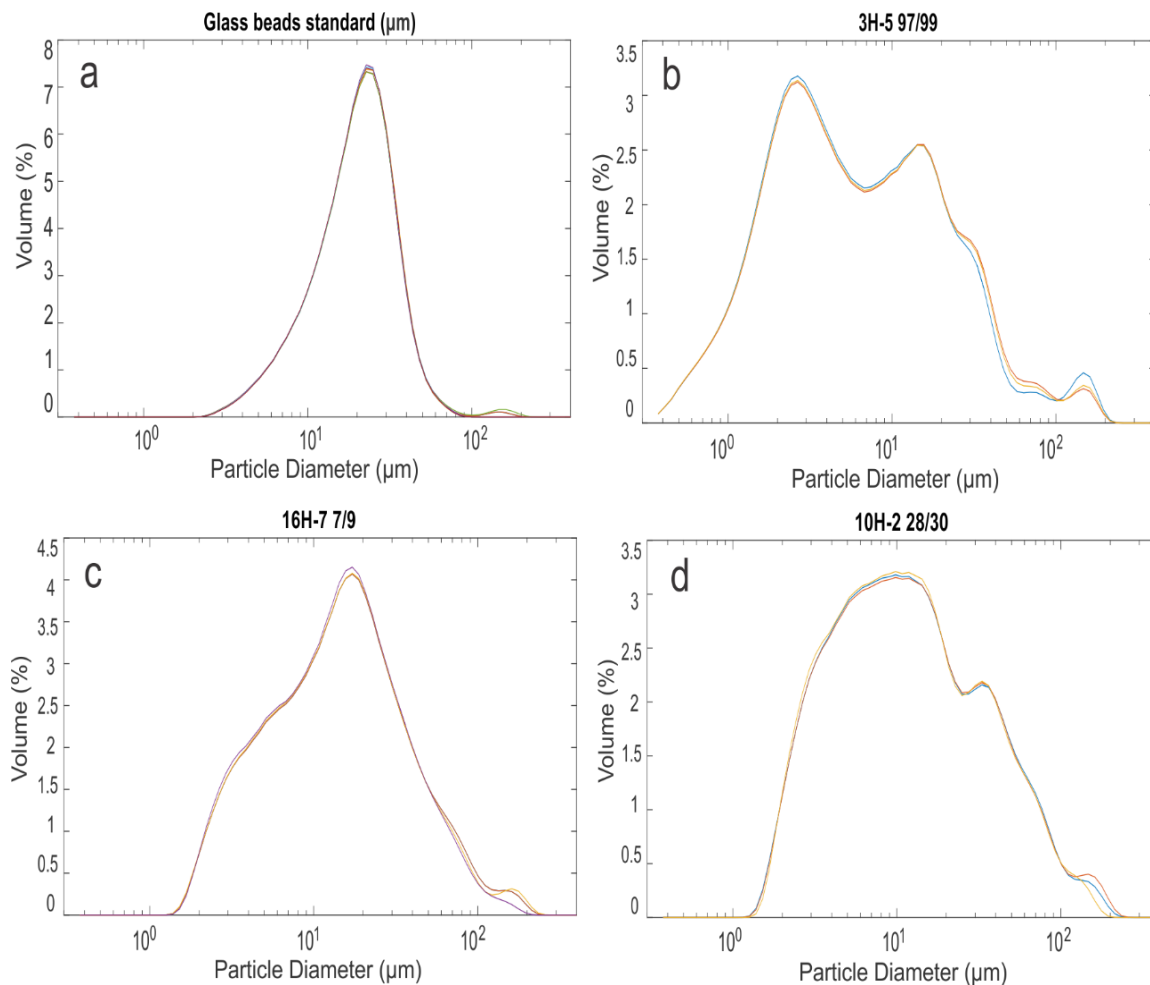


Figure 3.3: Replicate runs from a single sample loaded in the Beckman Coulter LS13 320 for: (a) 24  $\mu\text{m}$  spherical glass beads; and U1357B samples (b) 3H-5 97/99 (c) 16H-7 7/9 (d) 10H-2 28/30. This test highlights that a 60 second run is sufficient to reproduce near identical grainsize frequency curves from a single loaded sample.

After freeze drying, it was found that some samples had a noticeable white fluffy substance (Figure 3.4b), that consisted of very fine, “whispy spines” from diatom chains, which were previously observed when examining smear slides for undissolved diatoms (Figure 3.4a). For these samples, the diatom “whispy spines” were removed from the sample before being

stirred in Calgon and the first run on the LPSA was analysed without it. For the repeat run the fluff was added into the aqueous liquid module chamber to test whether it caused any clumping. This process was repeated for three other samples containing the diatom “spines”. No differences were observed in the grain size distributions of the initial and repeat runs, thus all other samples containing the diatom spines (52) were run following the standard procedure described above.

At the end of the grain size analysis a total of 341 samples (165 seasonal couplets) were analysed due to an accidental loss of 8 samples during an equipment failure. The ~66 year resolution of the dataset was not disturbed as only light couplets were lost. The data gathered from the LPSA (Appendix 2A) was then statistically analysed using the GRADISTAT programme (Blott and Pye, 2001; Appendix 2B). Note that for graphing and associated calculations the Wentworth grain-size scale (Boggs, 2006) was used to determine the percentages of grain size fractions from the raw LPSA data.

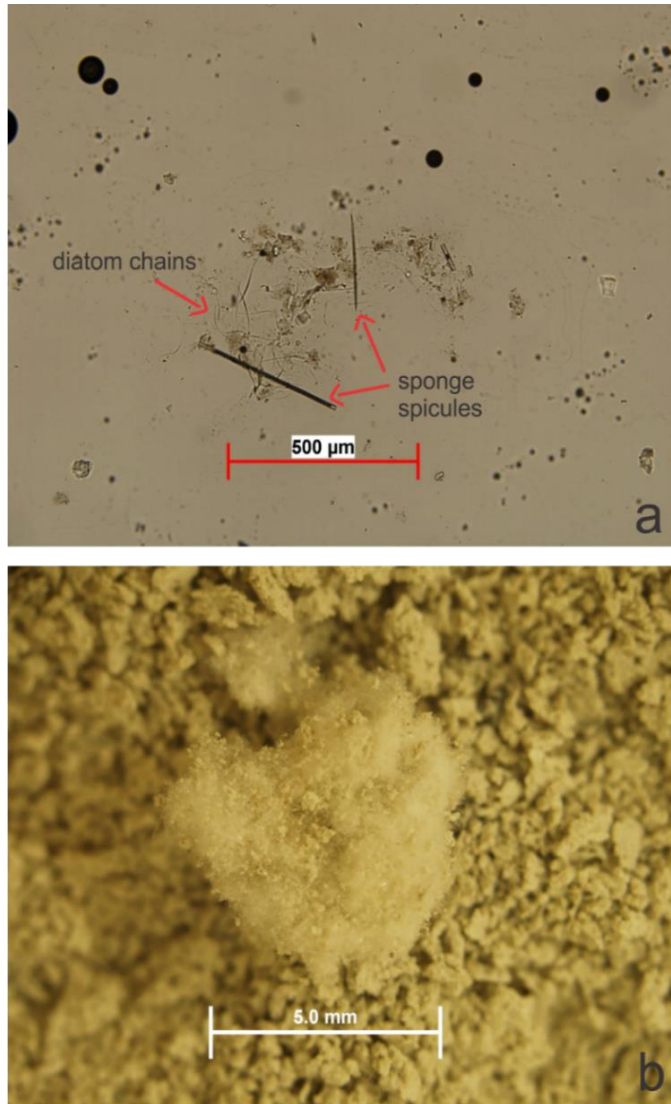


Figure 3.4: (a) Example of a smear slide image showing sponge spicules and wispy layers of diatom chains; (b) photograph of diatom fluff found in some samples. Both images are from sample 19-5H 43/45.

### 3.4.2 Subsampling reproducibility

84 samples were subsampled after NaOH and H<sub>2</sub>O<sub>2</sub> treatment, and an additional 12 samples were subsampled before the chemical treatment in order to test the reproducibility of both the treatment methodology and cone-and-quartering subsampling procedure. Least square regression of the sand% of the original and repeat samples displays a strong correlation of  $r^2=0.74$  (Figure 3.5b) and  $r^2=0.75$  (Figure 3.6b) for subsampling after and prior the chemical treatment respectively, providing confidence in the reproducibility of the data and the cone-and-quartering method of subsampling.

### 3.5 Additional uncertainties associated with grain size analysis using the LPSA

In addition to uncertainties associated with the subsampling method and potential for clumping of grains discussed above, the LPSA also presents some setbacks in accuracy. The aqueous liquid module in the LPSA does not accurately record the  $<2 \mu\text{m}$  clay that may compromise a significant part of the size spectrum. This is because platy minerals are measured by their largest projected area which causes them to be recorded as the same size as larger equant grains, although they have much smaller settling velocity and were likely deposited in aggregates. This yields results with weaker relationship to the dynamics of deposition (McCave et al., 1995; McCave and Hall, 2006). Consequently, interpretation of changes in flow speed when using the LPSA should be treated with some caution, as the coarse clay/fine silt fractions may be recorded in the medium silt/coarse silt grain size range – which is for example, the key size in the sortable silt mean method of inferring changes in flow speed (McCave et al., 1995). Konert and Vandenberghe (1997) have thus proposed a cut-off point of  $8 \mu\text{m}$  for clay when using the LPSA to measure grain size. In this thesis the cut-off point for clay was kept at  $4 \mu\text{m}$  as no significant differences in the trends of grain size distributions were found when using the alternative.

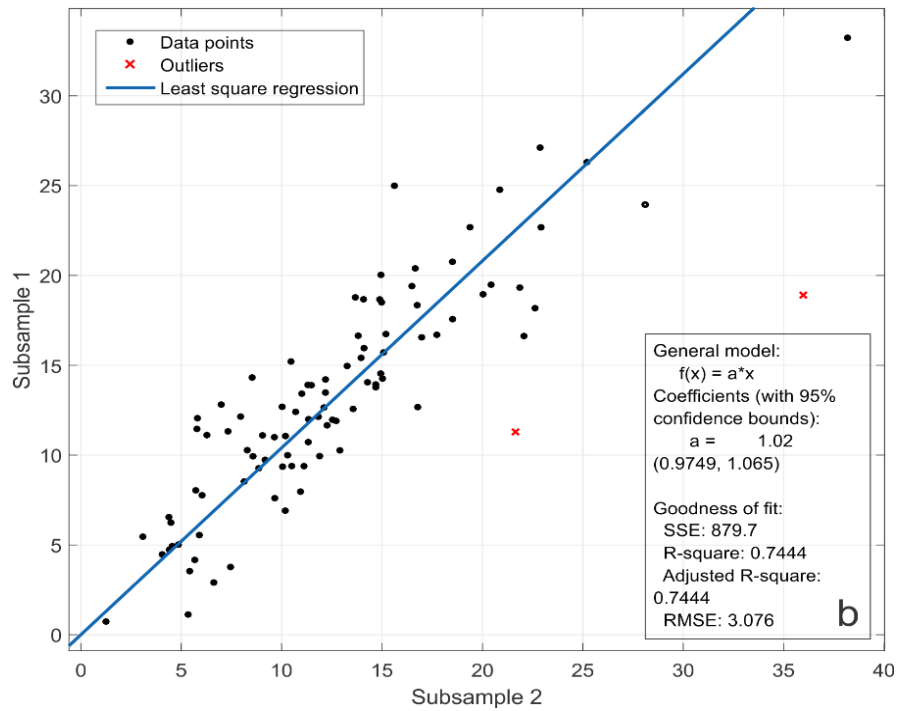
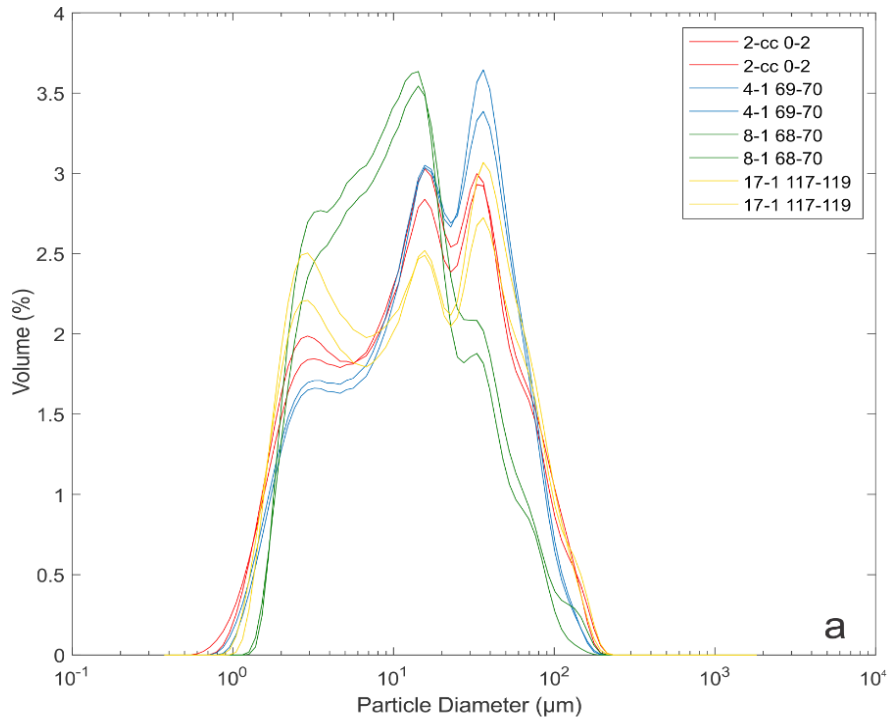


Figure 3.5: (a) Grain size curves of representative samples (original and repeat runs) that were subsampled after chemical treatment; (b) least square regression of sand% showing a high reproducibility with an  $r^2$  value of 0.744.

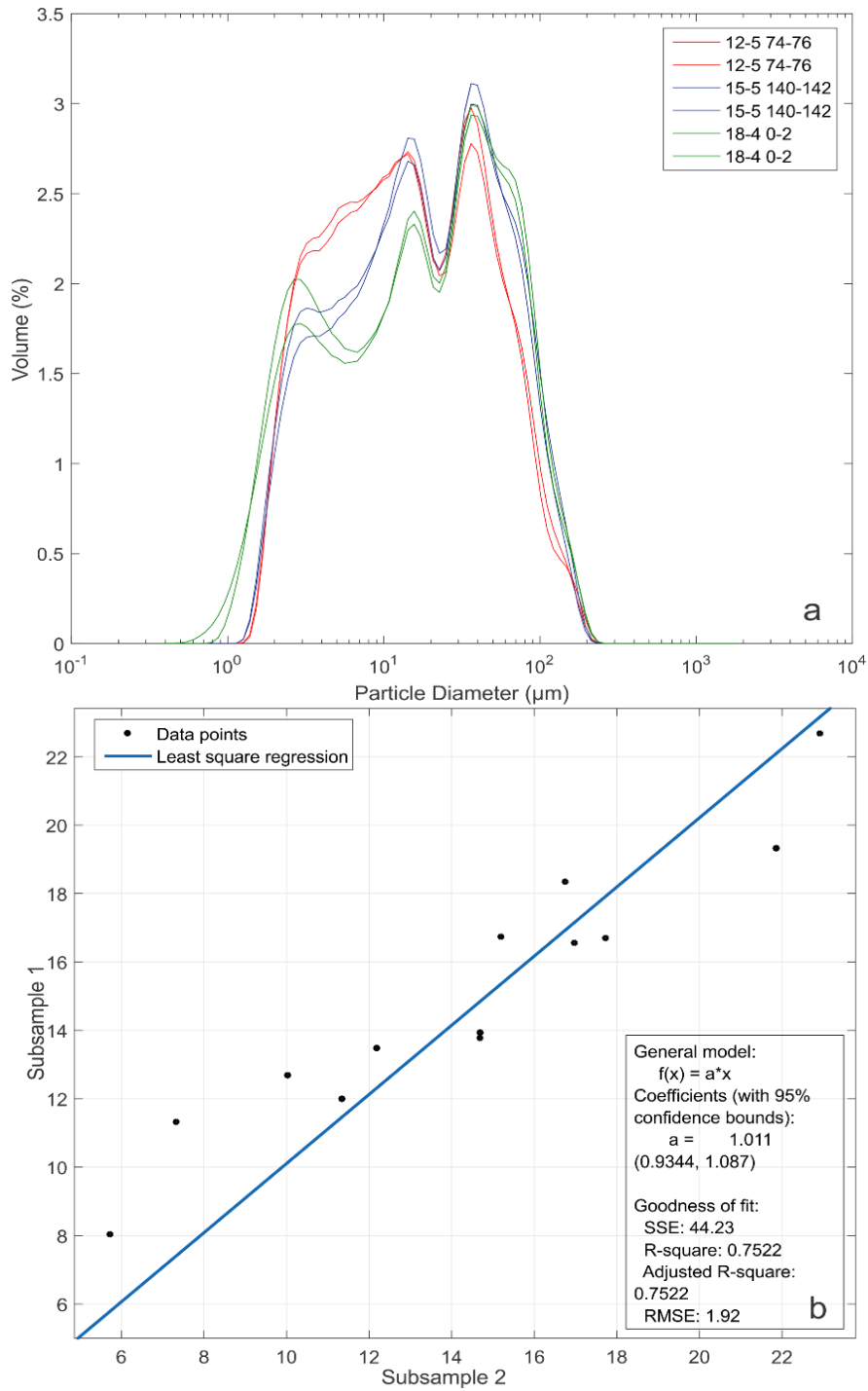


Figure 3.6: (a) Grain size curves of representative samples (original and repeat runs) that were subsampled prior to chemical treatment; (b) least square regression of sand% showing a high reproducibility with an  $r^2$  value of 0.752.

### 3.6 Linear sedimentation and mass accumulation rates

Linear sedimentation rates (LSR) were calculated using the age-depth (CSF-D) model for core U1357B (see Appendix 4). LSRs were calculated for every centimetre in the Bayesian age depth model and binned into 10 cm values. No bulk density measurements were made for U1357B, and line-scan density measurements have a high signal to noise ratio, therefore bulk densities (moisture and density [MAD]) of discrete sample from core U1357A were used (available from the IODP repository). These values were converted to age using the U1357A age-depth model based on 36 bulk organic carbon dates (using an identical Bayesian approach as U1357B; Dunbar et al. in prep) and a linear fit was taken through the data (Figure 3.7). This linear fit model was then interpolated onto the U1357B age scale to obtain an age versus density model. While this approach misses higher frequency variations in density, which are anticipated to be minor due to the consistent lithology, it does correct for downcore compaction. Mass accumulation rates (MARs; Appendix 4) for the terrigenous and biogenic silica fractions were calculated using the following formula:

$$\text{MAR} = \%X * \text{LSR} \times \text{BD}$$

Where MAR=mass accumulation rate (g/cm<sup>2</sup>/yr)

LSR=linear sedimentation rate (cm/yr)

X=the percent abundance of the component of interest

BD=bulk density (g/cm<sup>3</sup>)

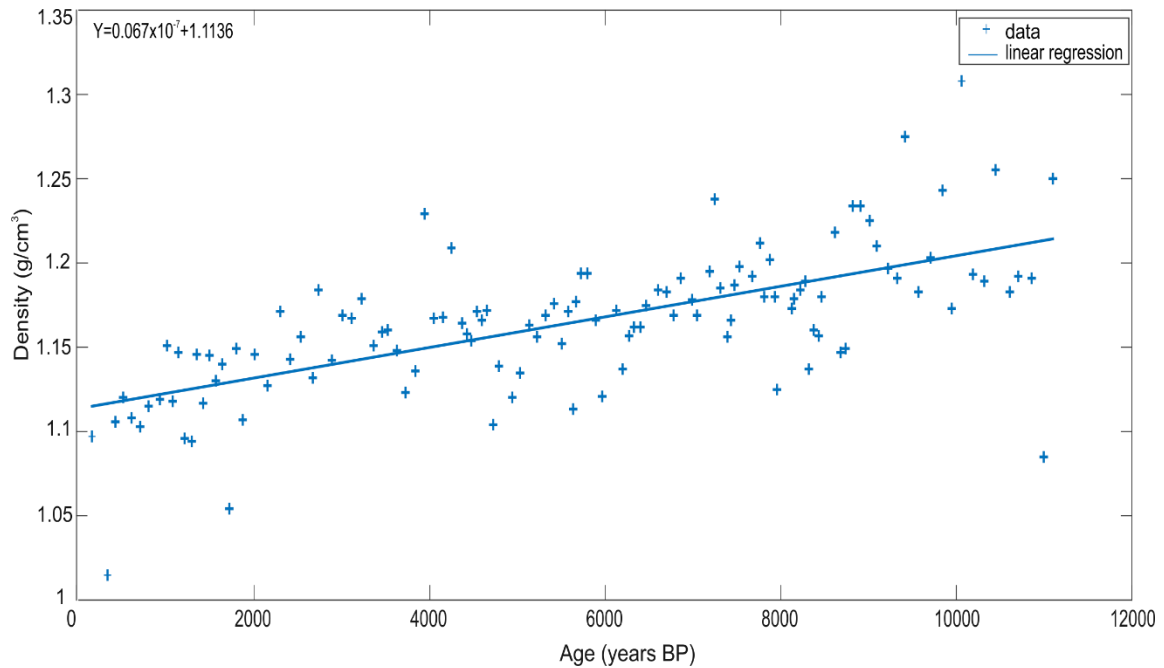


Figure 3.7: Moisture and density (MAD) values from discrete samples of core U1357A with a linear interpolation fitted through the data.

### 3.7 Image Analysis

Line scanned core photographs (available from the IODP 318 repository) were converted to a greyscale value (a total of 3,009,401 values) using MATLAB. The greyscale provides a discrete value between 0-255 for each pixel of the line-scan photograph, where 0=white and 255=black. These values were then averaged across the middle part of core face (x-axis) to provide a sub-mm grey-depth scale on the CSF-A (including core voids). This was then converted to CSF-D scale which removes the presence of voids. In order to make the dataset manageable for spectral analysis, the data were binned into 57,500 values (using median of every data point in a bin). The age model was then used to interpolate ages to the grey-depth scale producing a resolution of 0.2 years between each binned greyscale value. Some differential oxidation of the cores, after it was split, may affect absolute greyscale between cores but identification of laminae will still be evident in this approach.

Counting of light laminae (cores 2-19) was carried out by overlaying the grey-depth scale with the greyscale values on the core photographs (in MATLAB) and visually picking high values on the greyscale curves (i.e. peaks) as well as visual confirmation of a light laminae in the core photograph (Figure 3.8). Visual confirmation of the core photo proved essential as core gaps

could falsely represent an occurrence of a dark lamina if using automated methods. The final laminae counts were binned into 100 year bins and 1 m bins and linearly detrended as a first order correction for sediment compaction. Where a 100 year bin had an interval of no core recovery (i.e. at the base of core runs where recovery was <100%), any laminae counts in that partial bin were filtered from the dataset.

This method has several uncertainties which could undermine the accuracy of the results: 1) cores had varying periods of exposure to air before photographs were taken, thus each core has slight variations in the degree of the colour development of the laminae. Efforts were made during the scanning of U1357B to expose the core for a period ~5 hours, until a visually comparative level of oxidation was achieved (Figure 3.9); 2) subtle laminae may be hard to identify using this approach; 3) towards the bottom of Unit II, laminae displayed colour banding ranging from reddish brown to greenish grey (Escutia et al., 2011), making the process of identifying a 'bloom event' based on a greyscale value and visual examination of the core face slightly more ambiguous. All of these uncertainties could potentially lead to an incorrect counting of the light laminae. However, a conservative approach was taken, and the laminae counting in this thesis should be considered semi-quantitative, and likely to underestimate the true number of laminae. An X-ray computed tomography scan of the entire core would likely identify more subtle laminae in the core. However, at a first order, this core photo approach is internally consistent and will provide an indication of the frequency of the larger "bloom" events (i.e. light laminae) the occurred at the study site in the Holocene.

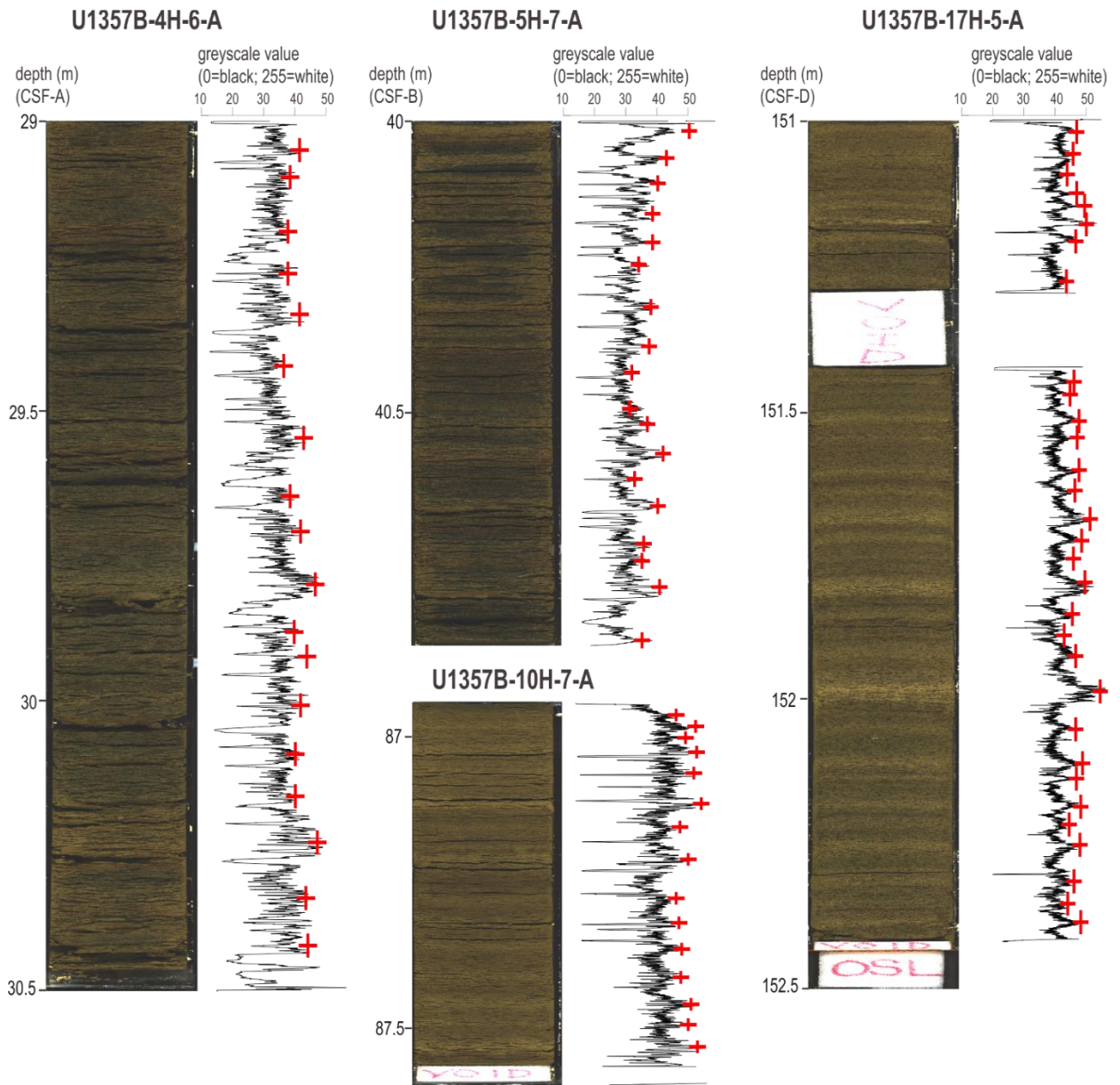


Figure 3.8: Visual example of lamina counting. The greyscale curve (black) is overlaid on core photographs for cores 4H-6, 5H-7, 10H-7 and 17H-5. Red crosses mark occurrence of light laminae.

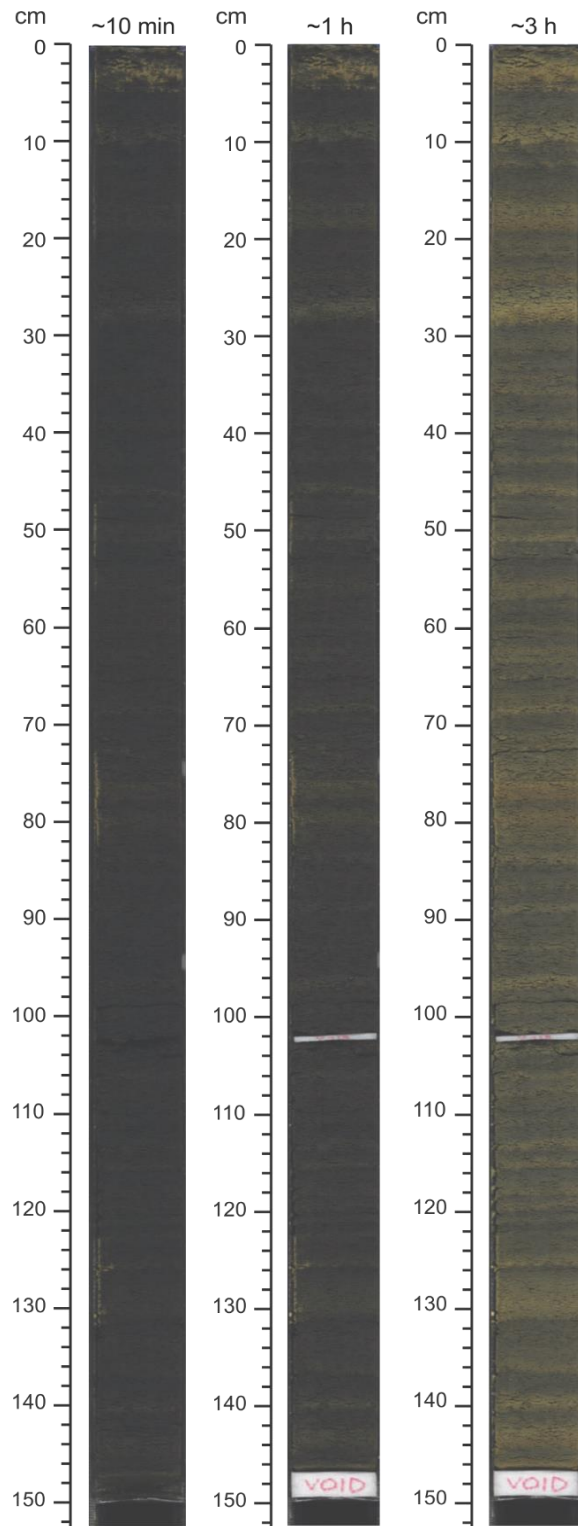


Figure 3.9: Images of colour development upon surficial oxidation in freshly split surfaces of core U1357A-6H-4. The colours develop more fully over a period of hours (after Escutia et al., 2011). For Hole U1357B, cores were routinely photographed after ~4-5 hours, once a consistent level of oxidation had been achieved.

## 3.8 Additional unpublished IODP-318-U1357B data used in the study

### 3.8.1 Natural Gamma Ray

NGR for U1357B was measured by IODP318 scientists on board JOIDES Resolution by running core sections through the Natural Gamma Radiation Logger (NGRL) at 10 cm intervals. NGR is a measure of the concentration of radioactive elements such as potassium, thorium and uranium, most often incorporated into clay minerals, thus it is often used as a proxy for clay concentrations (Escutia et al., 2011).

### 3.8.2 Carbon and Deuterium isotopes

Carbon isotope ( $\delta^{13}\text{C}_{\text{FA}}$ ) and deuterium isotope ( $\delta\text{D}_{\text{FA}}$ ) values from lipid biomarkers for U1357B (directly paired samples with the grain size analysis in this thesis) were obtained by Kate Newton, James Bendle and Heiko Moossen (University of Birmingham). Carbon isotope concentrations were determined using gas chromatography/mass spectrometry (GC/MS) analysis. These values are based on  $\text{C}_{24}$  fatty acids extracted from U1357B samples which were concluded to most likely be produced by non-diatom pelagic phytoplankton. The  $\delta^{13}\text{C}_{\text{FA}}$  record in this core was interpreted to represent a paleoproductivity proxy reflecting changes in  $\text{CO}_{2(\text{aq})}$  drawdown at the core site (see Newton, 2015). Deuterium isotope values were measured on  $\text{C}_{18}$  fatty acids and interpreted to largely reflect inputs of isotopically depleted glacial meltwater to the site from the proximal glaciers of the Adélie Land region (see Newton, 2015).

### 3.8.3 $\text{TEX}_{86}^{\text{L}}$

Sea surface paleo-temperature estimates are provided by the tetraether lipid-based  $\text{TEX}_{86}^{\text{L}}$  proxy derived from marine prokaryote micro-organisms. This proxy is based on the relationship between certain types of glycerol dibiphytanyl glycerol tetraethers (GDGTs) and the temperature at which they are produced (Kim et al., 2010). Kim et al. (2012) and Newton (2015) interpret this proxy to predominantly reflect subsurface temperature in Antarctica as marine organisms which produce these lipids (phylum Thaumarchaeota) are most abundant at a depth interval of 45-105 m.  $\text{TEX}_{86}^{\text{L}}$  was measured on 172 samples from core U1357B (paired to the grain size data presented in this thesis) at the Royal Netherlands Institute for Sea Research (NIOZ) by Veronica Willmont.

### 3.8.4 Biogenic Silica

Sedimentary biogenic silica concentrations (BSi%) were measured at the University of Otago by Christina Riesselman, and are direct splits (i.e. paired samples) from the grain size samples. Measurements were carried out using an alkaline extraction spectrophotometric method modified from Strickland and Parsons (1972) and Mortlock and Froelich (1989) by the Stanford University Stable Isotope Laboratory. All of the datasets mentioned in Section 3.8 are included in Appendix 6.

## 3.9 Time Series Analysis

The Mann and Lees (1996) robust red noise multi-taper method (MTM) was applied to the greyscale data (cores 2-19) and NGR data using the SSA-MTM toolkit for spectral analysis (Vautard et al., 1992). A red noise background model, where a time series shows a continuous decrease of spectral amplitude with increasing frequency, is usually a more appropriate null hypothesis for paleoclimatic data than the white noise model (Hammer et al., 2013b) *mtmML96* is based on the original algorithm of Thomson (1982), where a set of tapers are applied to the time series which act to suppress different parts of the series, and is designed to avoid spectral leakage. The spectrum is then based on the average generated from each tapered series. This method requires evenly spaced data, thus the greyscale values were first linearly interpolated to an equal sample spacing of 0.196 years and MTM analysis was run with 7 tapers to the data. For NGR analysis, samples were interpolated to an 8 year spacing and 5 tapers applied to the data for MTM analysis. Fewer tapers were applied to the NGR due to the coarser resolution sampling spacing.

As the grain size samples are irregularly spaced in the time domain (an average of  $66\pm 33$  years), interpolation of these data to an even time step for MTM time series would introduce a significant bias. Thus, spectral analysis was required to be run on an unevenly sampled dataset. This was overcome by using a Lomb Scargle Fourier Transform (Schulz and Mudelsee, 2002), as part of the REDFIT function in the PAST software (Hammer et al., 2001; 2013a), which like MTM assumes a red-noise background. REDFIT was performed on the mean sand% of dark and light laminae (average of a couplet). A linear detrend was applied to the data, and 'Welch oversampling segment averaging' was applied, which implies splitting the time series

into a number of segments overlapping by 50%, and averaging their spectra. This reduces noise but also reduces spectral resolution (Hammer et al., 2013b).

For the sand% data, the frequency oversampling resolution was set to three, and segment averaging to one, to provide the best trade-off between frequency resolution and background noise. A rectangular 'window' was applied which allowed the analysis to be carried out on the original data without fading out the time series near the ends. Before running the analyses, the data was successfully tested for the fit to the red-noise model by using the runs value and its 5% acceptance interval. This test was run by using the Monte Carlo simulation option and setting the oversampling frequency = 1, segment averaging = 1 and window = rectangle. The frequency of each spectral peak has an uncertainty of  $\pm \frac{1}{2}$  BW (resolution bandwidth). For both MTM and REDFIT analysis, confidence intervals at the 95 and 99% levels were calculated to identify significant spectral peaks.

To assess evolving periodicities in the time domain, a continuous Morlet wavelet transform (Torrence and Compo, 1998) was applied to the datasets using the software PAST. The significance of periodicities within the data is represented by a colour scale with warmer colours (red) reflecting more powerful periods. For each analysis, a cone of influence is produced which indicates the region in which results are not influenced by edge effects i.e. the signals in the wavelet transform at one end of the time series will get wrapped around to the other end since wavelet analysis assumes the time series is periodic, which results in attenuation of lower frequencies (Hammer et al., 2013b). As with REDFIT, the significance levels relative to the estimated noise background are calculated using a red noise model and a first-order autoregressive process.



## Chapter 4: Results

### 4.1 Grain size analysis

#### 4.1.1 Variations in mud and sand percentages

The grain size record for U1357B spans the last ~11.4 ka, and first order variations can be readily identified in the sand (>63  $\mu\text{m}$ ) and mud (<63  $\mu\text{m}$ ) content of the record (Figure 4.1). Three distinct intervals are identified, with an overall trend of decreasing sand% up core ranging from ~20-10% between ~11.4 and 8.2 ka, ~15-10% between 8.2 and 4.5 ka, and dropping sharply to ~10-5% at ~4.5 ka until present time. The mud% shows the opposite trend, which is expected with a two component system of mud versus sand%. Superimposed on these opposing long-term trends are shorter-term cyclical variations of ~400-500 and ~1200-1500 years. On the ~400-500 year scale the sand and mud contents vary by ~3-7% while the ~1200-1500 year scale appears to be expressed by larger variations of ~8-15%. Approximately 90% of all dark laminae contain a greater sand%, generally having double the volume, compared to the light laminae. The dark laminae also show consistently lower mud (5-10%) throughout the 11.3 ka record (Figure 4.1).

The NGR and the clay% (<4  $\mu\text{m}$ ) derived from grain size analysis, both show a long-term decreasing trend up core until ~4.5 ka, after which both datasets show a rapid and significant increase in values, followed once again by a long-term decreasing trend. These trends differ to that of the long-term increase in mud%, suggesting variations in mud are primarily representative of the silt fraction. The short-term variations superimposed on the long-term trends in the clay% and NGR appear to resemble the duration of the cycles observed in the sand and mud datasets (Figure 4.2).

Given that the LPSA produces data in volume percent, an increase in a particular grain size fraction will result in a decrease in another. To assess if the shift in terrigenous input is due to either a background increase in mud or sand content (or both), the sand and mud contents of the laminae were normalised to the overall terrigenous fraction (derived as 1 minus the BSi content; Appendix 5). This assumes an insignificant organic and calcium carbonate fractions (with wt% of ~1-3). The new long- and short-term trends for the sand and mud datasets are the same but the sudden drop in sand values at ~4.5 ka is more muted, while the rapid increase in the mud content during this time is increased in amplitude (Figure 4.3). Dark

laminae still contain a higher sand content compared to light laminae, however the mud% for the normalised values is now greater for the dark laminae rather than the light laminae.

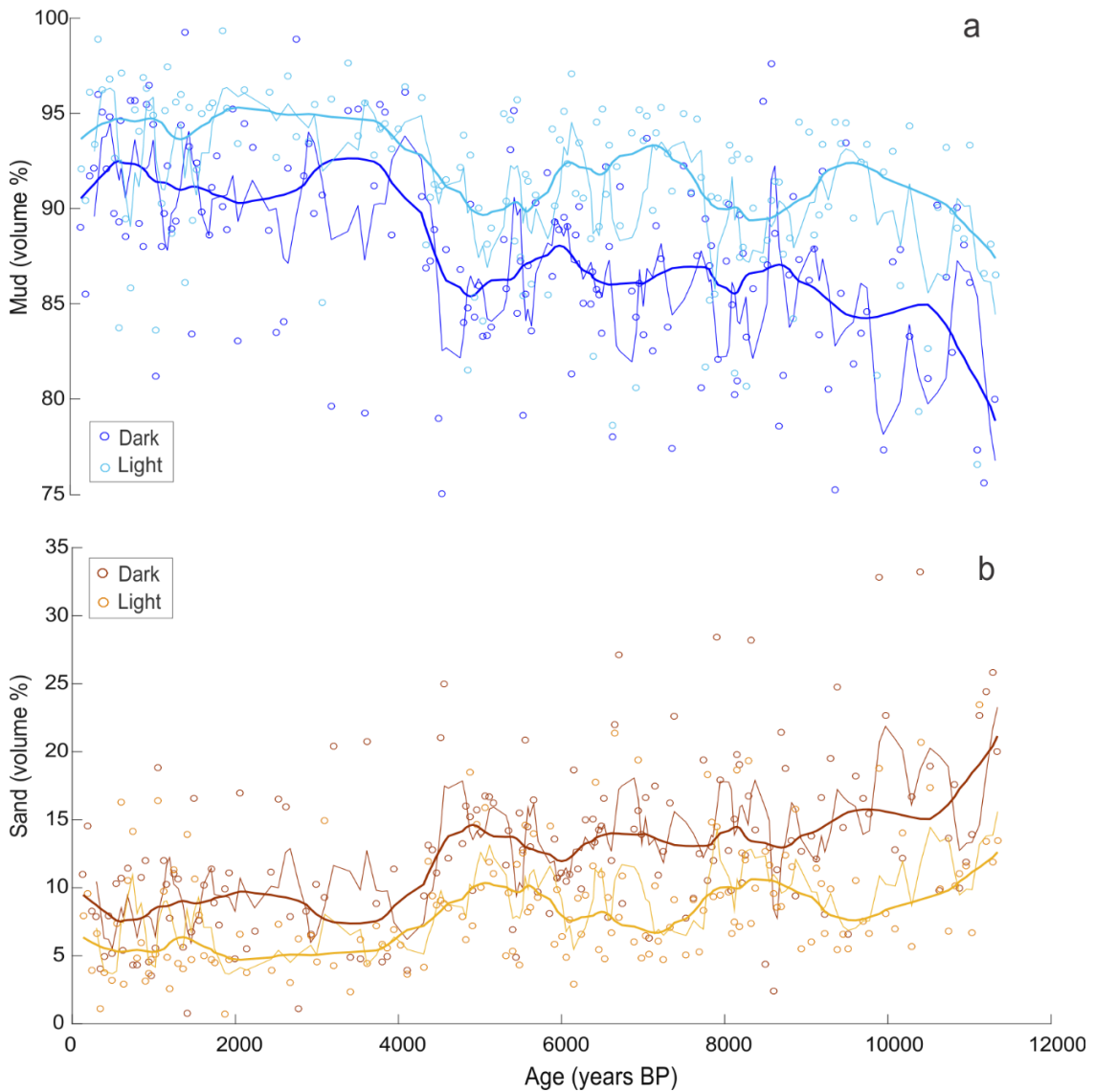


Figure 4.1: (a) Mud% of dark (dark blue) and light (light blue) laminae; (b) sand% of dark (brown) and light (orange). Thin lines through the data are 4-point moving averages, thick lines are a robust version of lowess smoothing (10%) that places less weight on outliers (rloess function in Matlab).

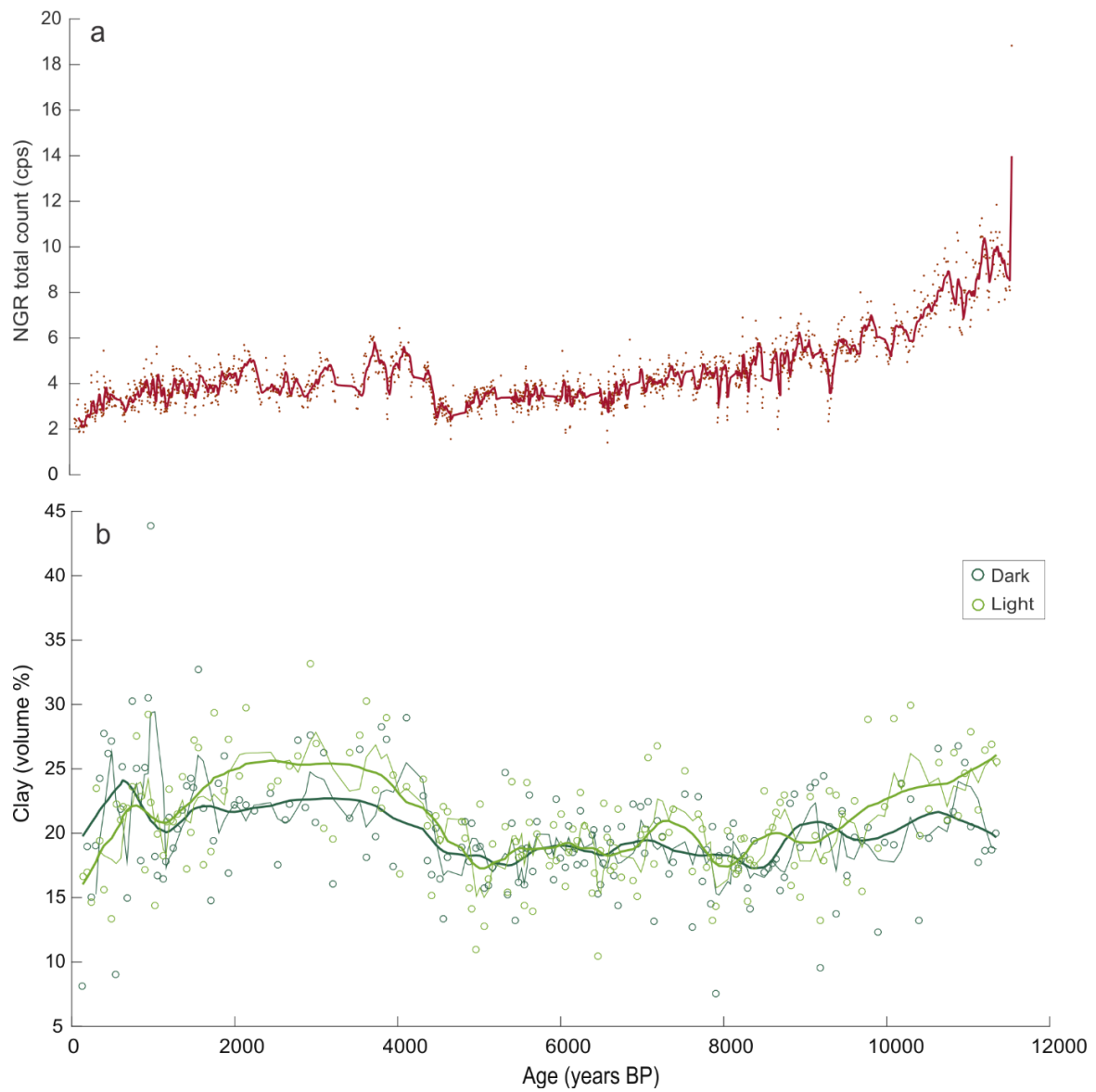


Figure 4.2: (a) NGR counts of U1357B with an 8-point moving average (data from Escutia et al., 2011); (b) clay% for dark (dark green) and light (light green) laminae. Thin lines are 4-point moving averages through the data, thick lines in (b) are a robust version of lowess smoothing (10%).

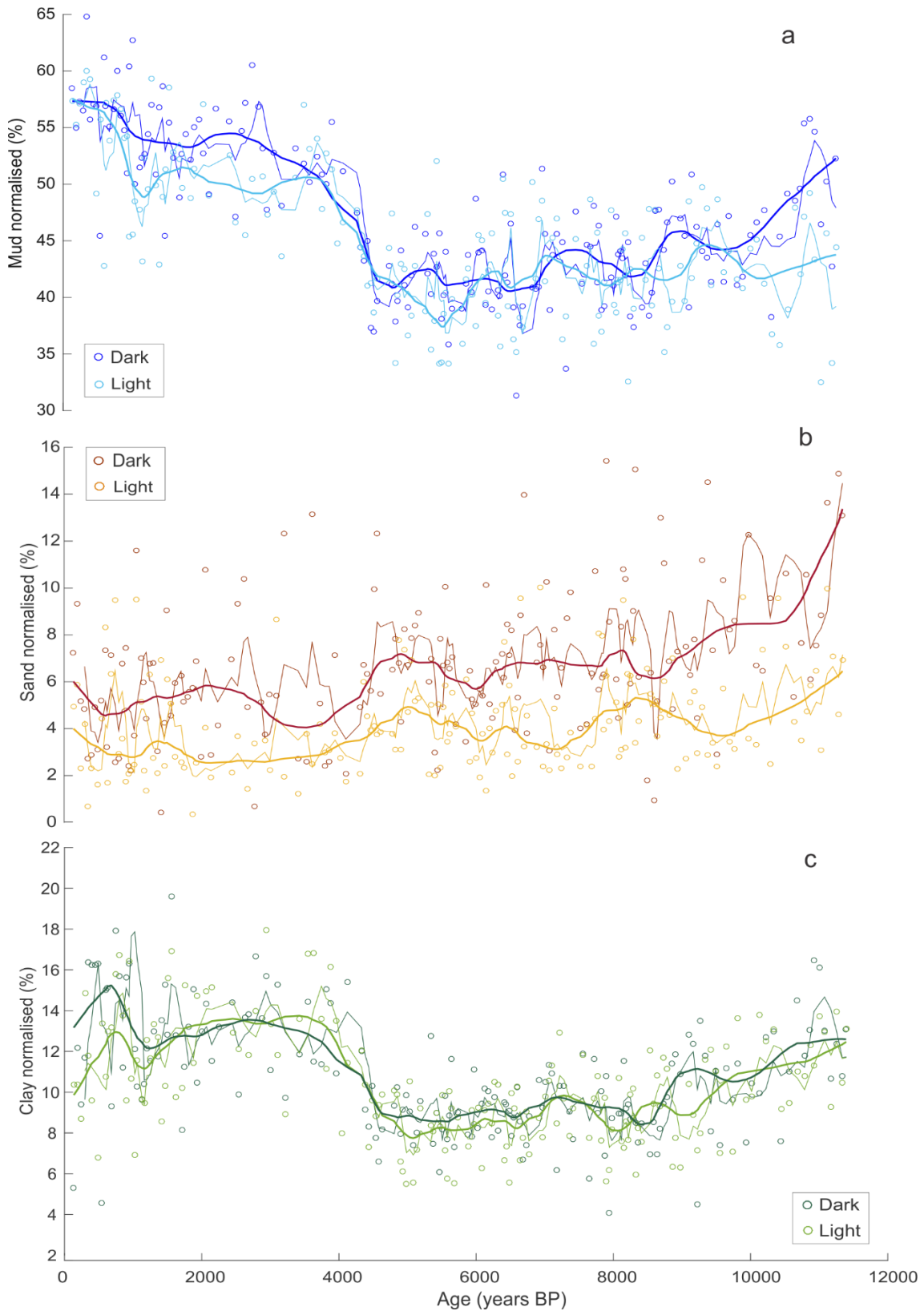


Figure 4.3: (a) Normalised (to the overall terrigenous content) mud% for dark (dark blue) and light (light blue) laminae; (b) normalised sand% for dark (brown) and light (orange) laminae; (c) normalised clay% for dark (dark green) and light (light green) laminae. Thin lines are 4-point moving averages through the data, thick lines are a robust version of lowest smoothing (10%).

#### 4.1.2 Mean grain size and sorting

The mean grain size and sorting trends show a long-term up core decrease and increase, respectively (Figure 4.4). Linear regression analysis between the two indices shows a weak-to-moderate correlation with an  $r^2$  value of 0.28 (Figure 1.1 in Appendix 2B). Superimposed on the long-term trend, the mean grain size of light laminae shows a very minor increase between ~11.4 and 8 ka, while the mean grain size of dark laminae shows a slight decrease during this time, after which the long-term decrease is resumed for both laminae with a sharp decrease to lower values at ~4.5 ka. For dark laminae, the mean grain size fluctuates from 10 to 30  $\mu\text{m}$  between ~11.4 and 8 ka, 10 to 25  $\mu\text{m}$  between ~8 and 4.5 ka and 7 to 20  $\mu\text{m}$  from ~4.5 ka to the present. For light laminae, this decrease is more muted, with the mean grain size fluctuating from 10 to 20  $\mu\text{m}$  between ~11.4 and 4.5 ka and 8 to 17  $\mu\text{m}$  from ~4.5 ka to the present.

Between 11.4 and 8 ka, sorting persistently increases, followed by a relatively stable distribution until ~1.5 ka, after which sorting again increases (Figure 4.4). The majority of grain size distributions fall within the poorly sorted category of Folk and Ward (1957), but some very poorly sorted samples are present before ~11 ka (see Appendix 2B). Throughout the record, dark laminae show consistently poorer sorting. The long-term trends and cyclic variations observed in the sorting and mean grain size are correlated with variations in sand%, whereby sand% correlates with increased sorting, and decreasing sand percent results in a decreased mean. Linear regression analysis of sand% versus sorting and sand% versus mean grain size shows a strong and a very strong correlation with  $r^2$  values of 0.61 and 0.82, respectively (Figures 1.2 and 1.3 in Appendix 2B).

#### 4.2 Linear sedimentation and mass accumulation rates

Linear sedimentation rates (LSRs) display a general long-term increase from 11.4 ka to the present (Figure 4.5). The LSR curve fluctuates between 0.7 cm/yr to 2.7 cm/yr on timescales of ~1000 yr. At longer timescales, there is an increase in LSR of ~0.8 cm/yr to ~2.5 cm/yr between 9.8 ka and 8.2 ka, after which point a sudden drop to ~1.3 cm/yr occurs. From ~7.8 to 4.5 ka, LSR remain relatively stable, oscillating between ~2 and 1.5 cm/yr approximately every 600-700 years. From ~4.5 to 3.8 ka, the LSR curve shows a sudden drop from ~2 cm/yr to 0.8 cm/yr. The LSR remain below 1cm/yr until ~2 ka, after which a sharp increase in values

to 2.5 cm/yr is observed. A ~600 year cyclicality whereby LSR fluctuates by ~0.5-0.8 cm is also observed during this period.

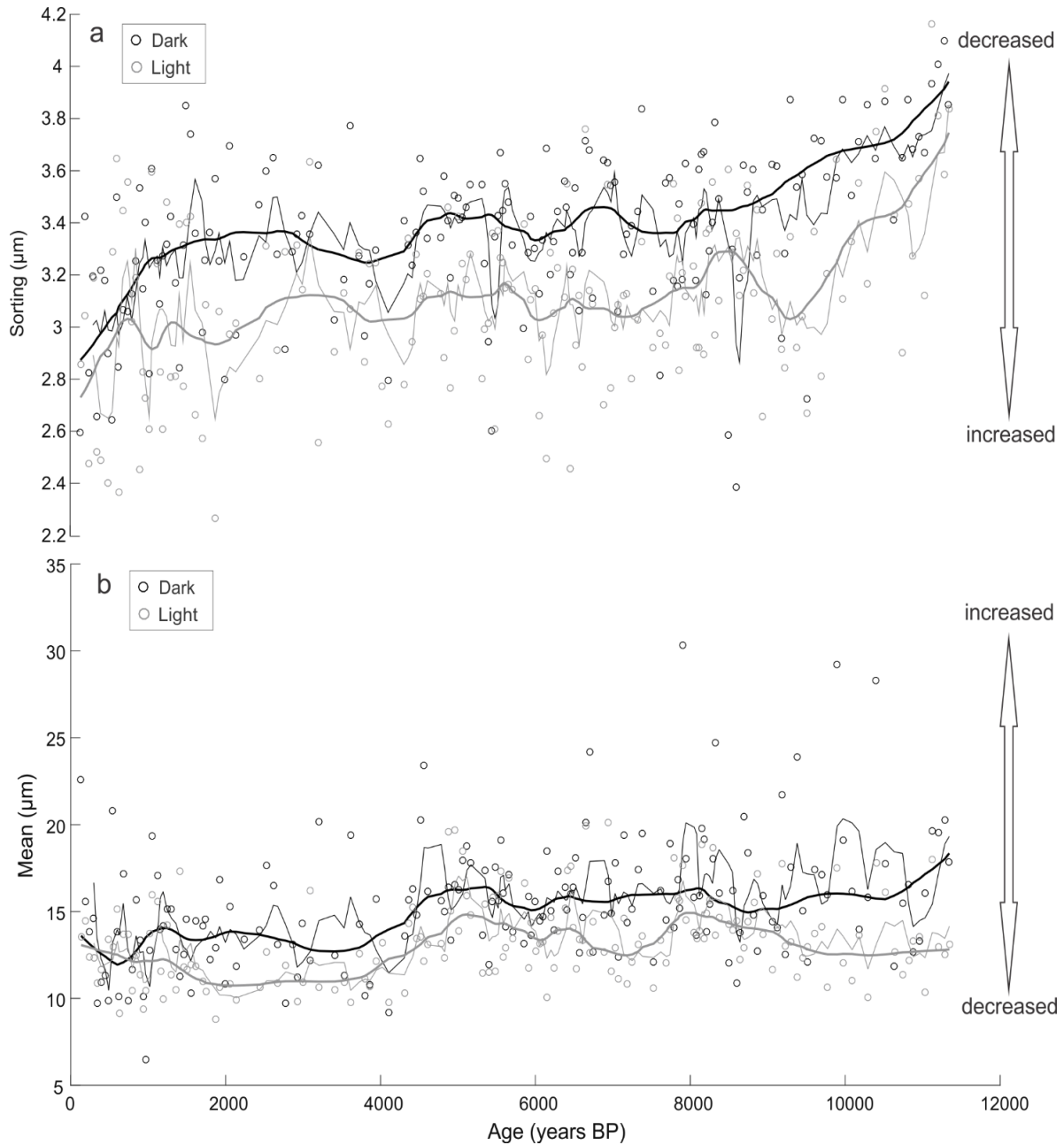


Figure 4.4: (a) Sorting for dark (black) and light (grey) laminae; (b) mean grain size for dark (black) and light (grey) laminae (Statistics use the Folk and Ward (1957) geometric method). Thin lines are 4-point moving averages through the data, thick lines are a robust version of lowess smoothing (10%).

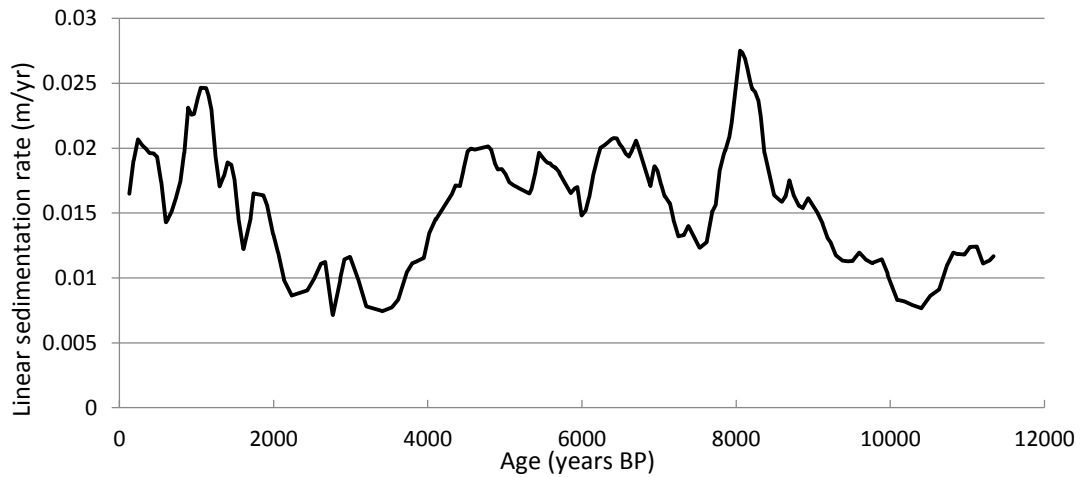


Figure 4.5: Linear sedimentation curve for U1357B.

Mass accumulation rates (MARs) for biogenic silica and the terrigenous fractions closely resemble the linear sedimentation curve (Figure 4.6). This relationship is expected due to the depositional setting at the site, as both terrigenous and biogenic sedimentation at the site likely being the product the same advection processes that have formed the drift in the Dumont d'Urville Trough. MARs for both components vary from  $\sim 0.4$  to  $1.8 \text{ g/cm}^2/\text{yr}$ . However, the long-term trends of the terrigenous and biogenic components are opposite, with the biogenic MAR displaying an overall weak long-term decline while the terrigenous MAR shows a weak long-term increase. This difference is most obvious at  $\sim 1.3 \text{ ka}$ , where the terrigenous MAR reaches its highest value of  $\sim 1.7 \text{ g/cm}^2/\text{yr}$ , while the biogenic MAR is considerably lower at  $\sim 1.2 \text{ g/cm}^2/\text{yr}$ .

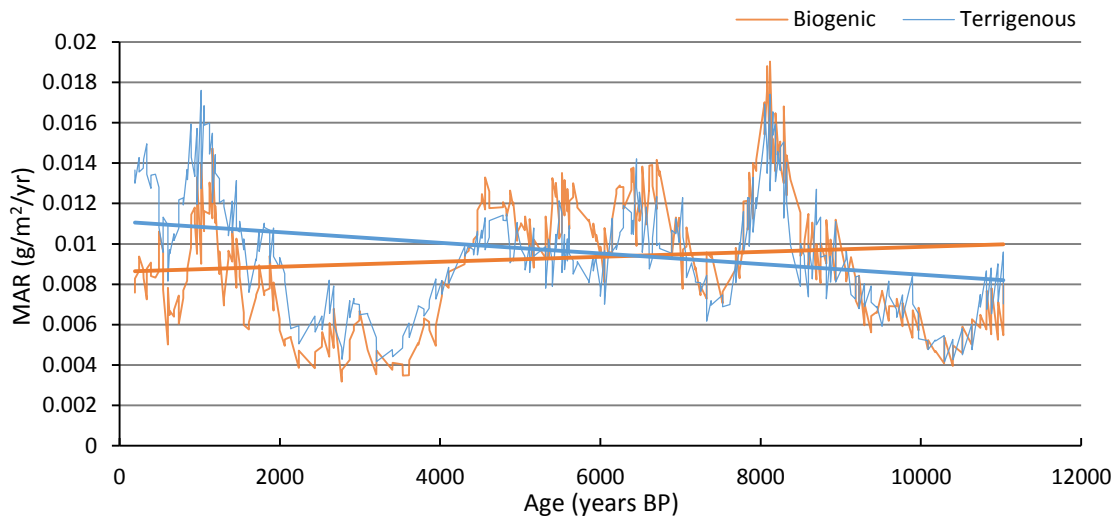


Figure 4.6: Mass accumulation rates (MARs) for the biogenic (orange) and terrigenous (blue) fractions of U1357B. Corresponding orange and blue straight lines are linear trends through the data.

The decoupling between biogenic silica and terrigenous MARs is well-illustrated when the biogenic silica and normalised mud percentages are plotted against time (Figure 4.7). The two curves show a gradual decrease until ~4.5 ka, after which point a rapid decrease in biogenic silica is observed. However, the mud percent continues to steadily increase. This suggests that after ~4.5 ka the opposing trends observed for biogenic silica and mud%, and the decoupling in the MARs may reflect variations in sediment focusing or a change in the sediment source. This is discussed further in Chapter 5.

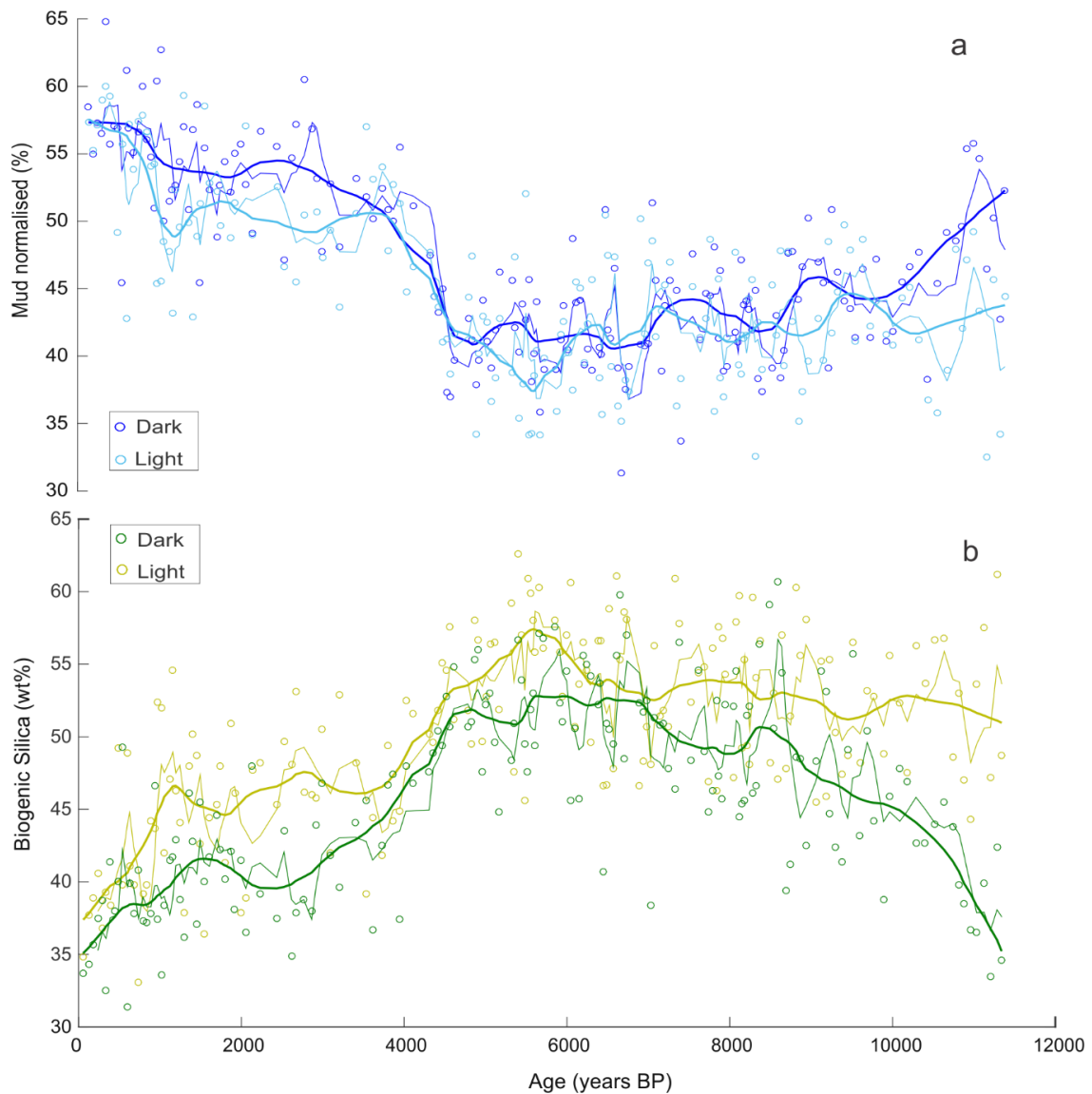


Figure 4.7: (a) Normalised mud% for dark (dark blue) and light (light blue) laminae; (b) biogenic silica% for dark (dark green) and light (light green) laminae. Note the decoupling trends of biogenic silica between dark and light laminae prior to 9.8 ka. Thin lines through the data are 4-point moving averages, thick lines are a robust version of lowess smoothing (10%). Biogenic silica data is unpublished and is courtesy of C. Riesselman (Otago University)

### 4.3 Grainsize frequency distributions

Based on the overall grain size statistics and terrigenous input, three distinct lithologic intervals have been identified: 1) a laminated muddy diatom ooze deposited from ~4.5 ka to the present; 2) a laminated diatom ooze with reduced terrigenous input deposited between ~4.5 and 8.2 ka; and 3) a muddy diatom ooze deposited between ~8.2 and 11.4 ka. This section discusses the detailed grainsize frequencies in these intervals. Each interval has a distinctive

polymodal grain size distribution described below, however the interpretation of changes to the environment of deposition is discussed in Chapter 5.

#### 4.3.1 Interval 1

The terrigenous component in this unit is dominated by mud for both dark and light laminae, with clay to coarse silt comprising >90% of the distribution. Grain size distributions display four modes within this size range. For the dark laminae the modes are; clay (2.8  $\mu\text{m}$ ), very fine silt (5.8  $\mu\text{m}$ ), medium silt (16  $\mu\text{m}$ ), and coarse silt (36  $\mu\text{m}$ ) (Figure 4.8). These modes are identical for the light laminae except for the very fine silt mode, which is slightly coarser (7  $\mu\text{m}$ ) (Figure 4.9). The light laminae also commonly display a more prominent medium silt mode, although there is considerable scatter in the very fine to medium silt range across all samples. The dominant mode for the dark laminae is in the coarse silt range (36  $\mu\text{m}$ ), while for the light laminae this mode drops off significantly and the dominant peak is observed in the medium silt range (16  $\mu\text{m}$ ). Both types of laminae show relatively small volume percent of grains greater than coarse silt, with the dark laminae on average having <9% very fine sand and <2% fine sand, while light laminae have <6% very fine sand and <1% fine sand. None of the samples measured had any grains exceeding fine sand size (250  $\mu\text{m}$ ) (see Appendix 3A).

#### 4.3.2 Interval 2

Very fine silt to coarse silt also make up the majority of the grain size distributions in this lithologic interval for both lamina types. However, in comparison to Interval 1 dark and light laminae show a slight increase in volume percentage of grains in the very fine sand fraction, with this size class representing ~9% and ~13% on average of the population for light and dark laminae, respectively (Appendix 3B). As with Interval 1, both types of laminae contain modes at 2.8, 16, and 36  $\mu\text{m}$ . Some samples contain an additional mode in the very fine sand fraction which occurs at 73  $\mu\text{m}$  for light laminae, but is relatively muted, and at 76  $\mu\text{m}$  for dark laminae where it is more pronounced. The dominant mode for both types of laminae is in the medium silt range (16  $\mu\text{m}$ ), particularly in the light laminae, where a very pronounced medium silt mode occurs in all samples. Compared to the other units in the core, Unit 2 contains the least sample-to-sample variability in the grain size distributions when light and dark laminae are considered separately. As with Unit 2, none of the samples measured had any grains exceeding fine sand size (250  $\mu\text{m}$ ).

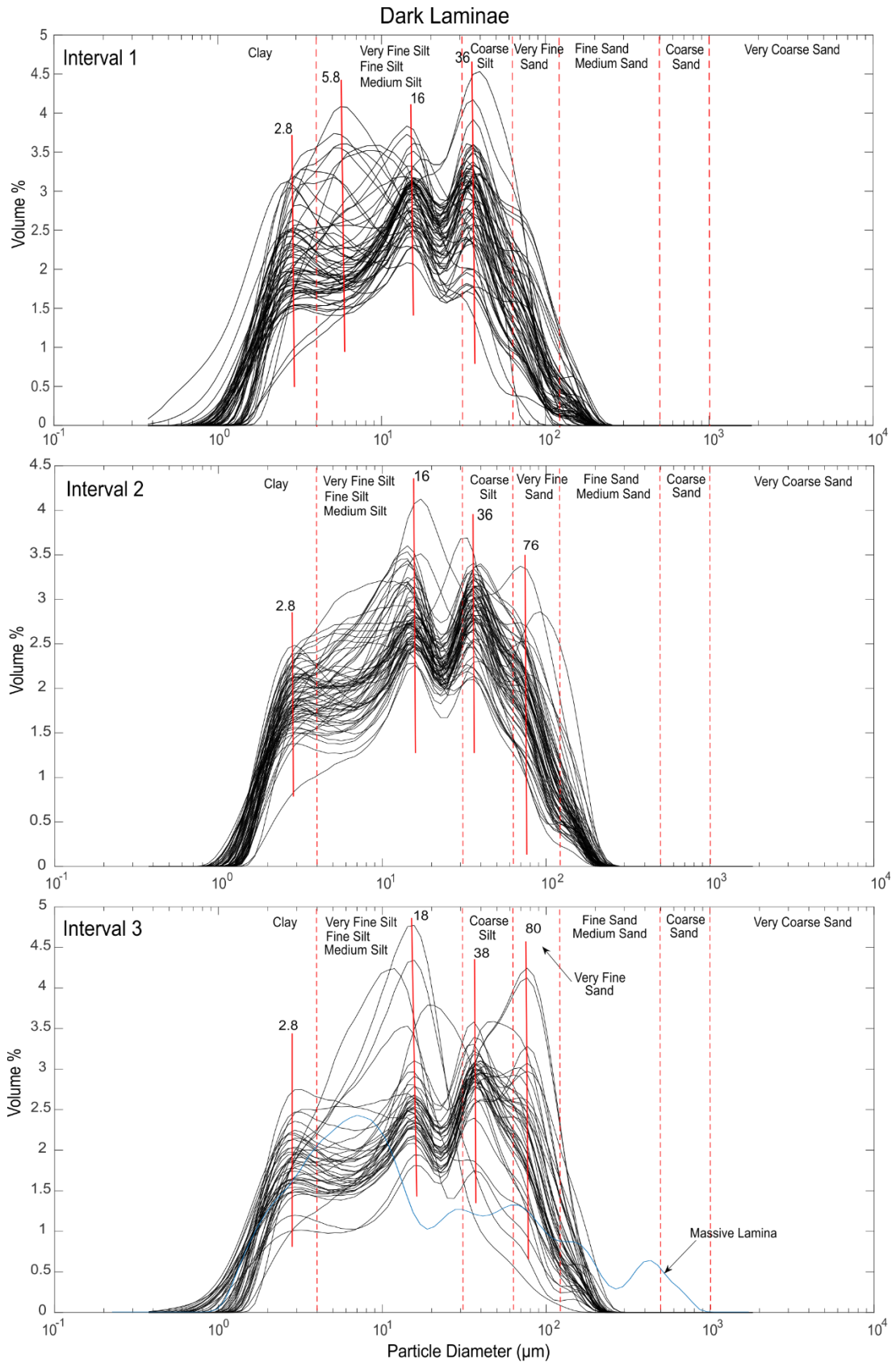


Figure 4.8: Grain size distributions of dark laminae for Interval 1, Interval 2 and Interval 3. Dashed red lines represent divisions between grain size ranges. Solid red lines highlight main grain size modes.

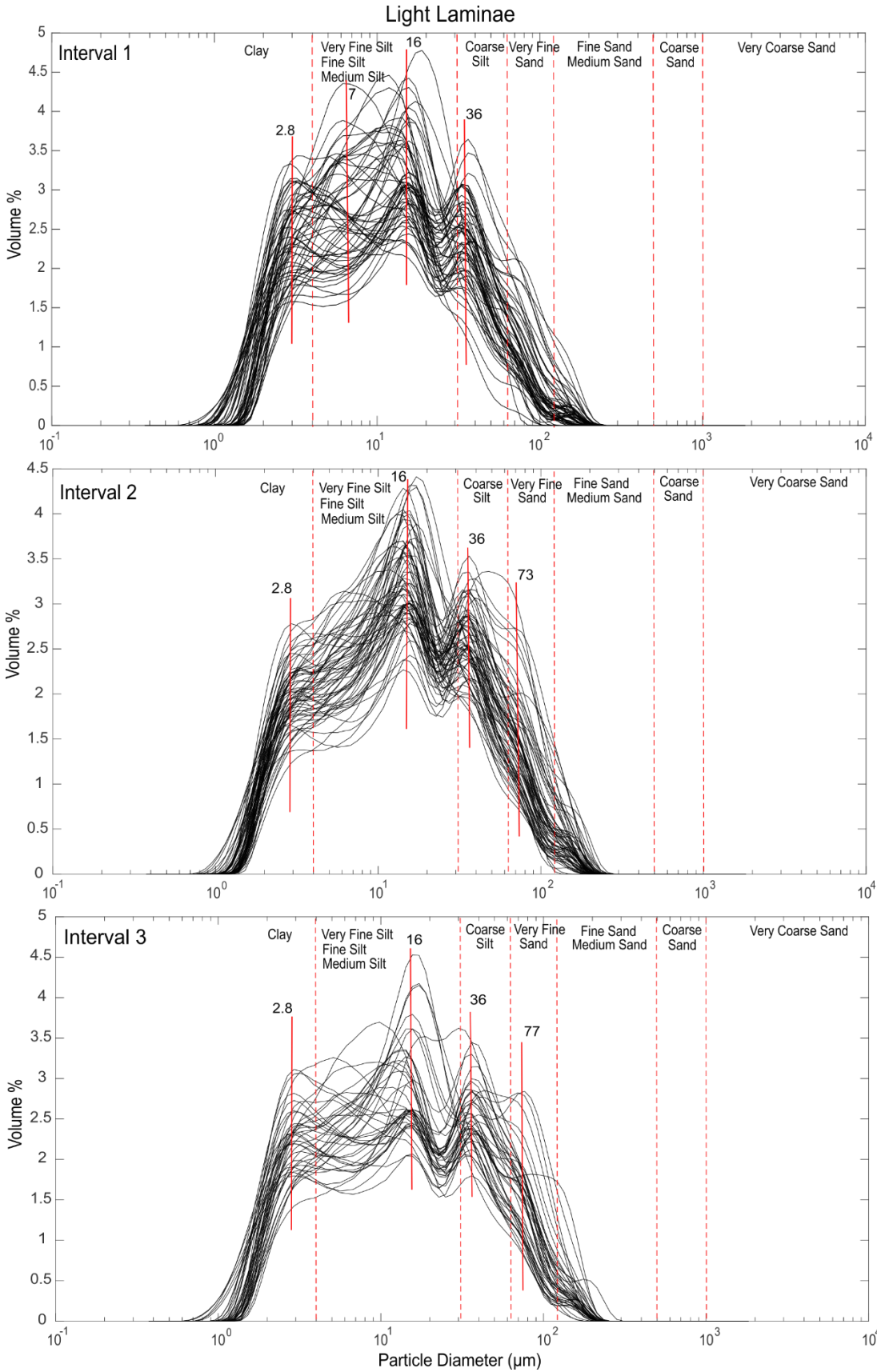


Figure 4.9: Grain size distributions of light laminae for Interval 1, Interval 2 and Interval 3. Dashed red lines represent divisions between grain size ranges written at the top of the graphs. Infilled red lines represent grain size modes.

### 4.3.3 Interval 3

Interval 3 is characterised by a greater abundance of coarse silt and sand. For dark laminae, the volume percent of grains in the fine and very fine sand fractions is greater than ~16%. For light laminae, the volume percent of grains in the fine and very fine sand fractions is less (~13%). Grains in the medium sand and coarse sand size range are observed in one sample, identified as a massive laminae (170 m CSF-D). The dominant mode for dark laminae is medium silt (18  $\mu\text{m}$ ), while the second largest mode is very fine sand (80  $\mu\text{m}$ ) (Figure 4.8). For light laminae the dominant mode is also medium silt, however slightly finer (16  $\mu\text{m}$ ), and the clay, coarse silt, and very fine sand modes are approximately of equal volume percent. No coarse sand grains are observed in the light laminae, although some medium sand is present (Figure 4.9; Appendix 3C).

## 4.4 Laminae counting

The laminae counts per 100 years closely follow the linear sedimentation curve, whereby more laminae per 100 years correspond to a greater sedimentation rate (Figure 4.10). The laminae counts per 100 years range from 10 to 35 throughout the record, indicating that preservation of the most pronounced diatom blooms do not occur every year. Laminae counts increase from ~10-20 laminae per 100 years between ~11.3 and 9.8 ka to 20-30 laminae per 100 years between ~9.8 and 4.5 ka. At ~4.5 ka laminae counts decrease rapidly to 10-15 laminae per 100 years until ~2 ka, after which higher numbers occur.

The number of laminae per metre (including a linear detrend to provide a first order correction for down core compression) is also presented. This is done to assess if age model artefacts bias the laminae per 100 year counts. If deposition of laminae per year were uniform through time, an increase in LSR should result in less laminae per metre. However, the opposite pattern is evident, with intervals of higher LSR containing more laminae per metre. Consequently, this suggests that the relationship of laminae increasing with higher sedimentation rates could either be a consequence of higher sediment accumulation at the site inhibiting sediment reworking (either by bioturbation or bottom currents) and better preservation of laminae, or that more biogenic bloom events (i.e. light laminae) occur as a consequence of the same process that result in higher sedimentation rates (i.e. sediment advection to the site).

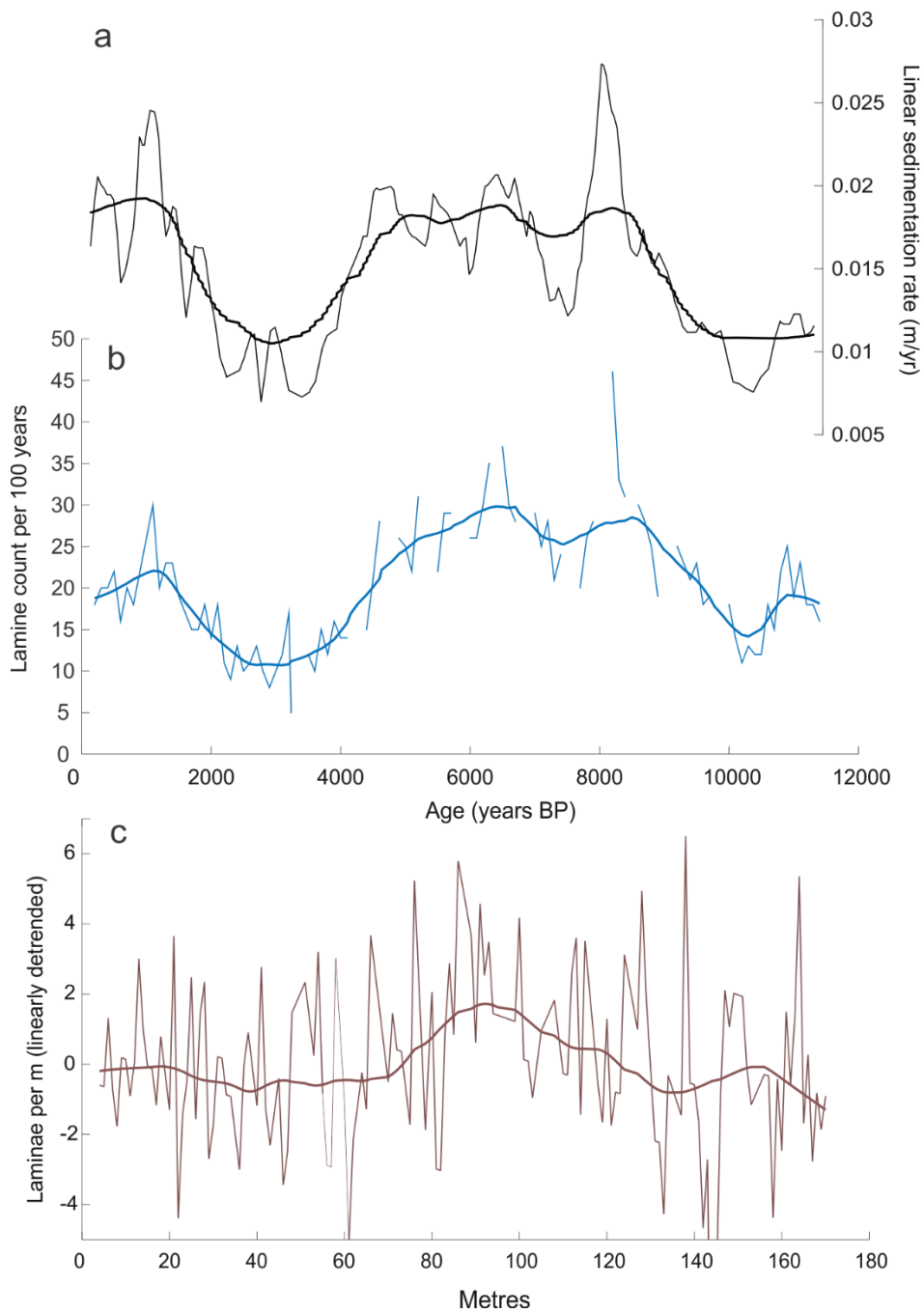


Figure 4.10: (a) Linear sedimentation rate curve for U1357B; (b) laminae counts per 100 years and; (c) laminae counts per metre. Thick lines through the data are a robust version of lowess smoothing (10%).

## 4.5 Spectral Analysis

REDFIT analysis of the mean sand% identified 11 peaks, 8 at the 95% confidence level (~1666, 1250, 770, 500, 470, 80, 163, 140) and 3 at the 99% confidence level (~625, 270, 135). Many of these cycles are also identified by wavelet analysis with the ~270 and ~625 cycles persisting clearly throughout all of the Holocene (Figure 4.11). Cycles at ~1250, 470, 163 and 140 were also identified in Wavelet analysis, however these show irregularity in their persistence throughout the Holocene. The ~1250 cycle is strongest between ~9 and 2 ka, while the 470, 180 and 140 year cycles appear to be strongest between ~11.3 and 7 ka and ~4 ka to the present. Two additional possible cycles at much lower frequencies of 2200, and 3320 were also picked up by wavelet analysis. The 2200 cycle is strongest between ~11.3 and 2.5 ka, but is absent after. The 3320 cycle is outside the cone of influence, and the time series length of ~11.4 kyr is not long enough to robustly identify if this is a periodic cycle. REDFIT analysis shows a cluster of peaks just below the 95% confidence interval indicating the presence of 470 and 770 year cycles. The largest of these peaks occurs near the centre of this cluster at 625 years. This cluster may represent a quasi-periodic cycle centred on 625 years, or a cycle with a high noise-to signal-ratio associated with the variations in sample spacing (i.e. sample resolution of ~66 years  $\pm$ 33 years (1 std)).

The ~1666-1250 and ~625 year duration cycles noted in the spectral analysis can be visually observed in the grain size curves suggesting these cycles are a real periodic component (Figure 4.3). However, cycles picked up by REDFIT and Wavelet analyses at ~135 and 270 years are not readily observed, and the decreasing height of these peaks with decreasing frequency suggest they may be a harmonic of the 66 year sample spacing and should thus be interpreted with caution.

To investigate the higher-frequency variations in the terrigenous content, multi-taper (MTM) analysis of the NGR data was carried out. Peaks at ~125, 105, 64 and 55 years were identified above the 99% confidence level (Figure 4.12a). The 125, 105 and 64, 55 year peaks may once again represent a variation of the same cycles. Additional peaks at ~333, 166 and 45 years were identified above the 95% confidence level. Due to the baseline shift in the NGR data at 4.5 ka and the overall short duration of the record (11.3 ka), cycles at periods greater than ~333 years display a high signal-to-noise ratio. Wavelet analysis identified similar cycles at ~120, 64 and 42 year periods which show a somewhat weak persistence between ~11.3 and 7 ka and ~4.5 ka to the present (Figure 4.12b). Additional cycles with periodicities at ~180,

250, 590, 1620, 2300 and 4700 were also identified. The 250 and 180 year cycles occur between ~11.3 and 7.8 ka and between ~5 and 2 ka. The 590, 1620 and 2300 year cycles occur throughout the whole record with the 1620 cycle showing the strongest signal. Most of the 4700 year cycle sits outside the cone of influence.

MTM analysis of greyscale data (cores 2-19) revealed peaks in the 2-10 year band above the 95% confidence level in all of the cores. Spectra of cores 2-16 (~8.4 ka to the present) revealed a greater frequency of peaks in the 3-6 year band whereas spectra of cores 17-19 (~11.3 to 8.4 ka) displayed more peaks in the 8-33 year band (Figure 4.13).

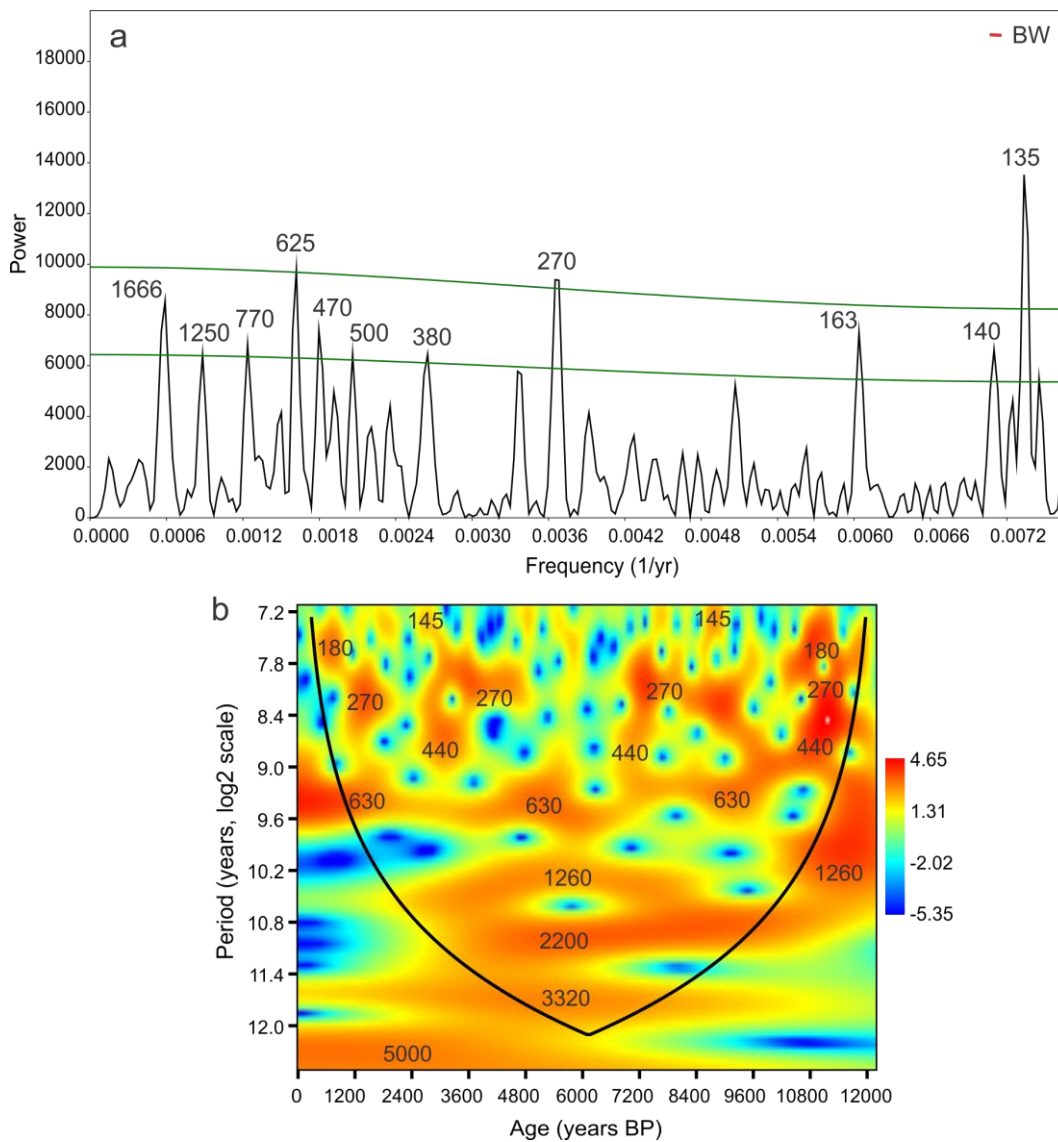


Figure 4.11 (overleaf): (a) REDFIT analysis of the mean sand% of U1357B. Labels indicate the periods of peaks significant at the 95% and 99% confidence levels, represented by the two green lines; bandwidth (BW); (b) Wavelet analysis of the mean sand% with periodicity of significant cycles labelled. The colour scale indicates the strength of the cycle with more positive numbers indicating greater strength. Curved black line represents the cone of influence.

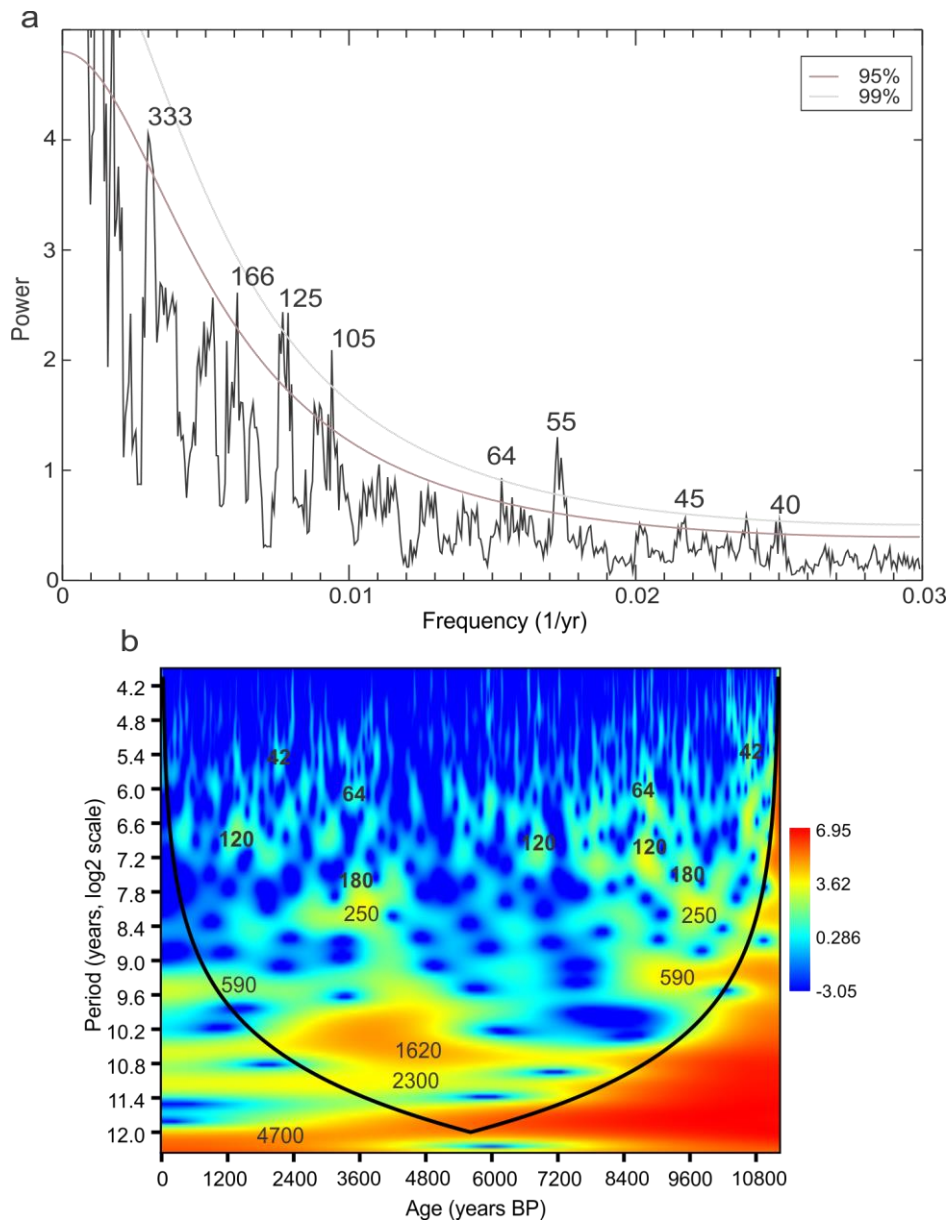


Figure 4.12: (a) Multi-taper analysis of the NGR content of U1357B. Labels indicate the periods of peaks significant at the 95%, 99% and chi-squared critical confidence levels, indicated by the three green lines; (b) Wavelet analysis of the NGR with periodicity of significant cycles labelled. The colour scale indicates the strength of the cycle with more positive numbers indicating greater strength. Curved black line represents the cone of influence.

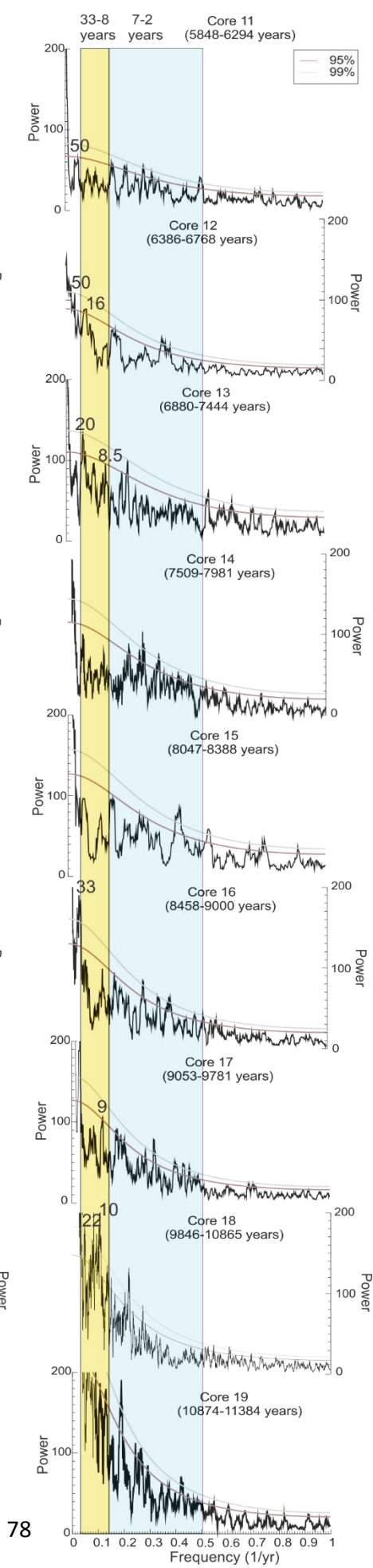
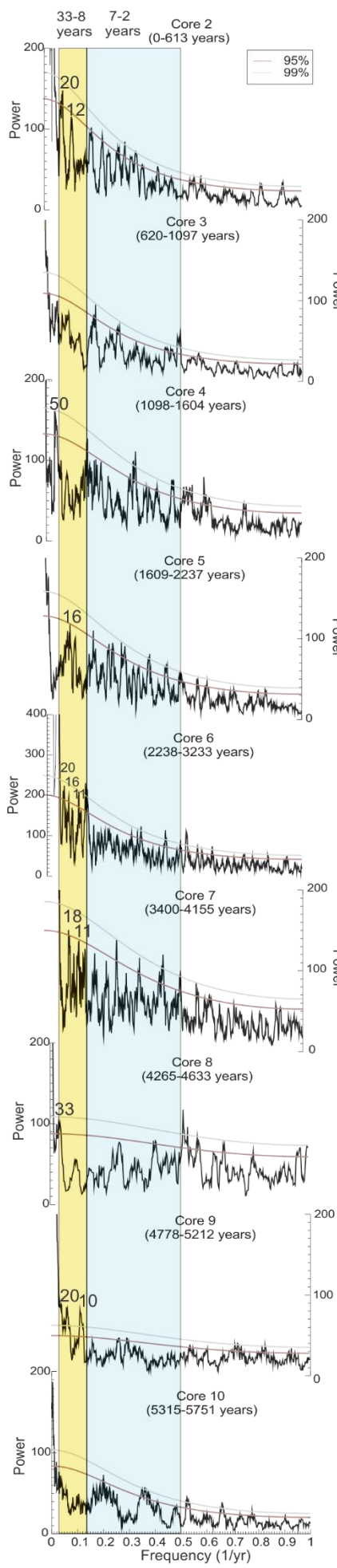


Figure 4.13 (overleaf): Multi-taper analysis of the greyscale data (cores 2-19). Blue shading indicates 7-2 year periods, yellow shading indicates 33-8 year periods.

---



## Chapter 5: Discussion

### 5.1 Sedimentary processes at IODP Site U1357

#### 5.1.1 Interval 3 (early Holocene ~11.4-8.2 ka)

The diatom ooze in Interval 3 has a large terrigenous component (i.e. high NGR content and low BSi%) than the overlying intervals and is characterised by poor sorting. Detailed analysis of the grain size distribution (see Section 4.3) indicates the presence of a coarse tail of fine (125-250  $\mu\text{m}$ ) to medium sands (250-500  $\mu\text{m}$ ), including one sample with coarse sands (>500  $\mu\text{m}$ ). In deep sea settings, grains >250  $\mu\text{m}$  are commonly interpreted as being IBRD (Krissek, 1995; Patterson et al., 2014), although in a coastal proximal setting other processes, including storm deposits, sea ice rafting, and gravity flows could account for grains of this size (Powell and Domack, 1995). Core photographs and seismic imaging of the core site show continuous sediment layering with no evidence of structures supportive of turbidity currents and other sediment density flows delivering sediment to the site (Figure 5.2). However, shipboard description of the core face suggest the presence of small isolated faceted and striated pebbles (lonestones) within this interval (Escutia et al., 2011), which is supportive of this coarse grained tail being of ice-berg rafting origin. The fine grained sands and muds have a distribution with similar modes to overlying intervals, albeit with an increase in the size of the coarse silt and very fine sand modes. In a glacial proximal setting, poorly-sorted sediment can be transported by surface and subglacial meltwater plumes with subsequent suspension settling within the water column (Powell and Domack, 1995; McKay et al., 2009). The increased sorting upcore in Interval 3 (from very poorly to poorly sorted) is consistent with an increasingly more distal setting from a glacial grounding line (McKay et al., 2009).

Glaciers in the Adélie Land region are inferred to have relatively clean basal layers due to the solid bedrock (Kleinschmidt and Talarico, 2000; Denis et al., 2009a). In general, the depositional environments offshore of polar tidewater glaciers are sediment starved and provide very low inputs of glacial marine terrigenous sediments (Powell and Domack, 1995; McKay et al., 2009). Therefore the release of terrigenous material through glacial melting is low (to absent) when glacier activity is steady and distal from the site, but is anticipated to increase with increased proximity to the glacier front or with enhanced dynamic ice discharge (which may occur either during a retreat or advance).

The presence of IBRD, decreased terrigenous sediment upcore with enhanced sorting indicate that this diatom ooze was deposited with a significant glacial influence which gradually decreases between ~11.4 and 8 ka. Interval 3 is interpreted to reflect the post-LGM retreat of local EAIS outlet glacier grounding lines from a proximal to more distal setting from the site. It is likely this distal setting was close to the modern day grounding line, as the Dumont d'Urville Trough is overdeepened between Site U1357B and the modern day grounding line and this bathymetry configuration is inherently unstable for marine-based ice sheets (Thomas and Bentley, 1978; Mackintosh et al., 2014). The preservation of well-defined alternations of biogenic and terrigenous-rich laminae with some IBRD can be explained by the calving bay reentrant model proposed by Domack et al. (2006) and Leventer et al. (2006). In this model, as the ice sheet begins to melt the retreat occurs much more rapidly over the deeper troughs while ice remains grounded on shallower banks and ridges (Figure 5.1). This type of bathymetry allows for the development of calving bay embayments in the retreating ice margin, which manifest as ice walled fjords. The converging margins of these fjords would have focused surface and subglacial melt into large volumes of low salinity, low density meltwater creating a strongly stratified water column. The terrigenous content of the meltwater containing iron-rich dust potentially promoted large diatom blooms in the spring. In summer, more melt provided additional terrigenous material, while ice-bbergs calving from retreating outlet glaciers were focussed within the embayments, helping to concentrate ice rafted debris.

Although seismic profiles taken across the site are spatially limited and contain noisy artefacts, the sediment drift at the core site appears to show a change in geometry at ~155 m below sea floor (Figure 5.2). Below this depth, sediment appears to be delivered from the south by the Zélée and Astrolabe glaciers where it appears to downlap onto the massive seismic unit at the base of the drift (i.e. the glacial diamict). In contrast, sediment in Interval 2 looks to be delivered from an east/southeast direction, onto the glacial diamict, with the crest of the mounded deposit to the north of the site. This is suggestive of either a different sediment source or a change in oceanic currents direction delivering sediment to the site, or a combination of both. The 1000 m deep Adélie Basin is surrounded by shallow banks, including the Adélie Bank immediately to the east, therefore rapid ice retreat from the basin with ice remaining grounded on the banks to create calving embayment seems likely during the initial phase of ice sheet retreat and sea level rise. Thus, the shift from a restricted calving bay environment to a more open marine setting may account for this shift in the architecture of

the drift with a decreasing glacial marine sedimentary influence as glaciers retreat to the south, and enhanced oceanic advection from the east.

An overall increase in Interval 3 in the  $\delta^{13}\text{C}_{\text{FA}}$  (from -32 to -30‰), BSi% (from 35% to 45%) and relatively lower  $\delta\text{D}_{\text{FA}}$  values (generally <-200‰) from the fatty acid biomarkers (Figure 5.3) in this interval are suggestive of increasing paleoproductivity and a significant glacial meltwater input, respectively (Newton 2015). This is also consistent with the grain size interpretation of Interval 3 being deposited during a glacier retreat stage. In a glacial proximal setting, high terrigenous input from sediment-laden meltwater plumes would have restricted light availability for diatom productivity. A persistent increase in primary production and biogenic accumulation upsection in Interval 3 is inferred to be due to reduced sediment supply by meltwater plumes and migration of the EAIS grounding line to a more distal setting.

The interpretation of a calving bay depositional environment with a significant meltwater input is also supported by the  $\text{TEX}^{\text{L}}_{86}$  data (Figure 5.3) which shows a high variance of temperatures ranging from 1 to 6°C (average, ~2°C) from ~11.4 to 8.2 ka, which may reflect meltwater induced stratification. Such fluctuating temperatures have been measured today in regional fjords during meltwater induced stratification events (Shevenell et al., 2011). Increased CDW influence at the Antarctic continental shelf margin in the early Holocene may also be responsible for these large fluctuations in subsurface temperature (Shevenell and Kennett, 2002). The stratified water column most likely reduced MCDW upwelling at the continental shelf margin, trapping the warmer water mass at depth (Golledge et al., 2014), which could explain such warm  $\text{TEX}^{\text{L}}_{86}$  subsurface temperatures during this time.

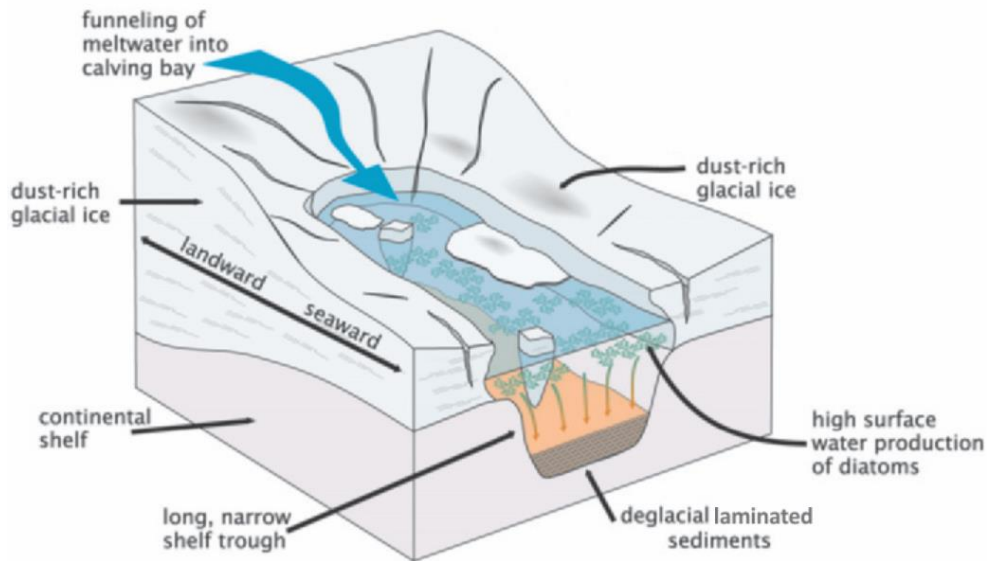


Figure 5.1: Generalised calving bay reentrant model modified from Leventer et al. (2006). Focusing of glacial meltwater results in a stratified water column and provides iron for diatoms to bloom in spring. In summer more terrigenous material results in a laminated sequence of seasonal deposition.

#### 5.1.2 Interval 2 (mid-to-late Holocene ~8.2 to 4.5 ka BP)

Interval 2 is characterised by an apparent absence of IBRD, increase in paleoproductivity ( $\delta^{13}\text{C}_{\text{FA}}$ , BSi%) and a significant increase in MARs (both biogenic and terrigenous; Figure 5.3). The mean grain size and sorting of the terrigenous material is relatively stable throughout the entire interval. This suggests that ice sheet grounding line retreat processes that are interpreted to have influenced the upcore changes in Interval 3 are not operating during Interval 2, and sediment input from grounding line processes remained comparatively stable through this interval. Thus, it is tentatively inferred that local glaciers had retreated to their present day grounding line position by 8.2 ka, and the site was no longer in a calving bay environment. Once grounded ice retreated from the shallow banks surrounding the core site, particularly the Adélie Bank, an overall increase in sediment supply to the core site was likely the consequence of increased advection from the east via the Antarctic Coastal and Slope Front Currents. Diatom frustules and sponge spicules are mainly in the 16 to 63  $\mu\text{m}$  range, much of which is maintained in suspension by weak currents (a few  $\text{cm s}^{-1}$ ; Dunbar et al., 1985). The greater area of open water for primary production during the summer, combined with an open pathway for advection of biogenic matter from the Mertz Glacier polynya can thus

explain the significant rise in linear sedimentation and mass accumulation rates for both biogenic and terrigenous material. In addition, time-series measurements of suspended particulate matter concentrations in McMurdo Sound, Ross Sea, reveal that particles  $<63 \mu\text{m}$  are kept in suspension and are swept westwards by the coastal currents, suggesting that some of this sediment and sediment from coastal outlets eastwards of the core site could contribute to the grain size population observed in U1357B as a suspended sediment load (Carter et al., 1981).

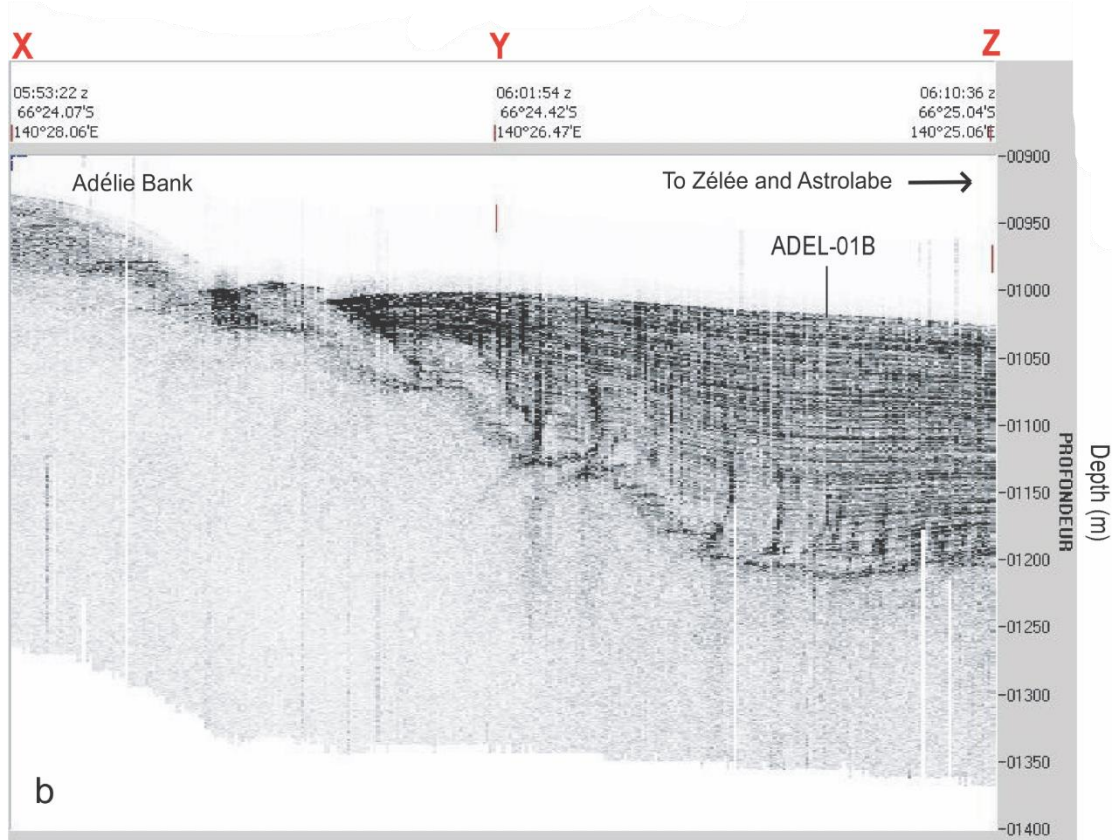
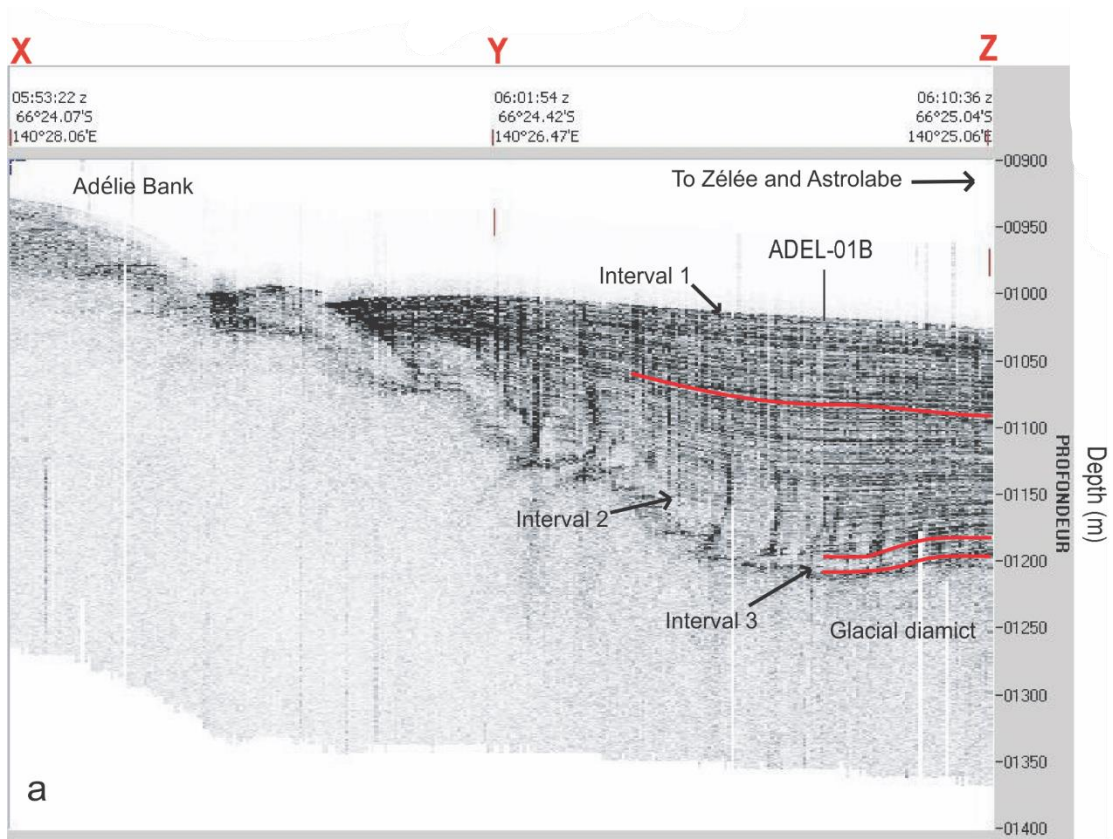


Figure 5.2: Seismic image of U1357B core site modified from Escutia et al. (2011). Red lines in (a) indicate boundaries between Intervals 1, 2 and 3; (b) image for unaltered self-analysis.

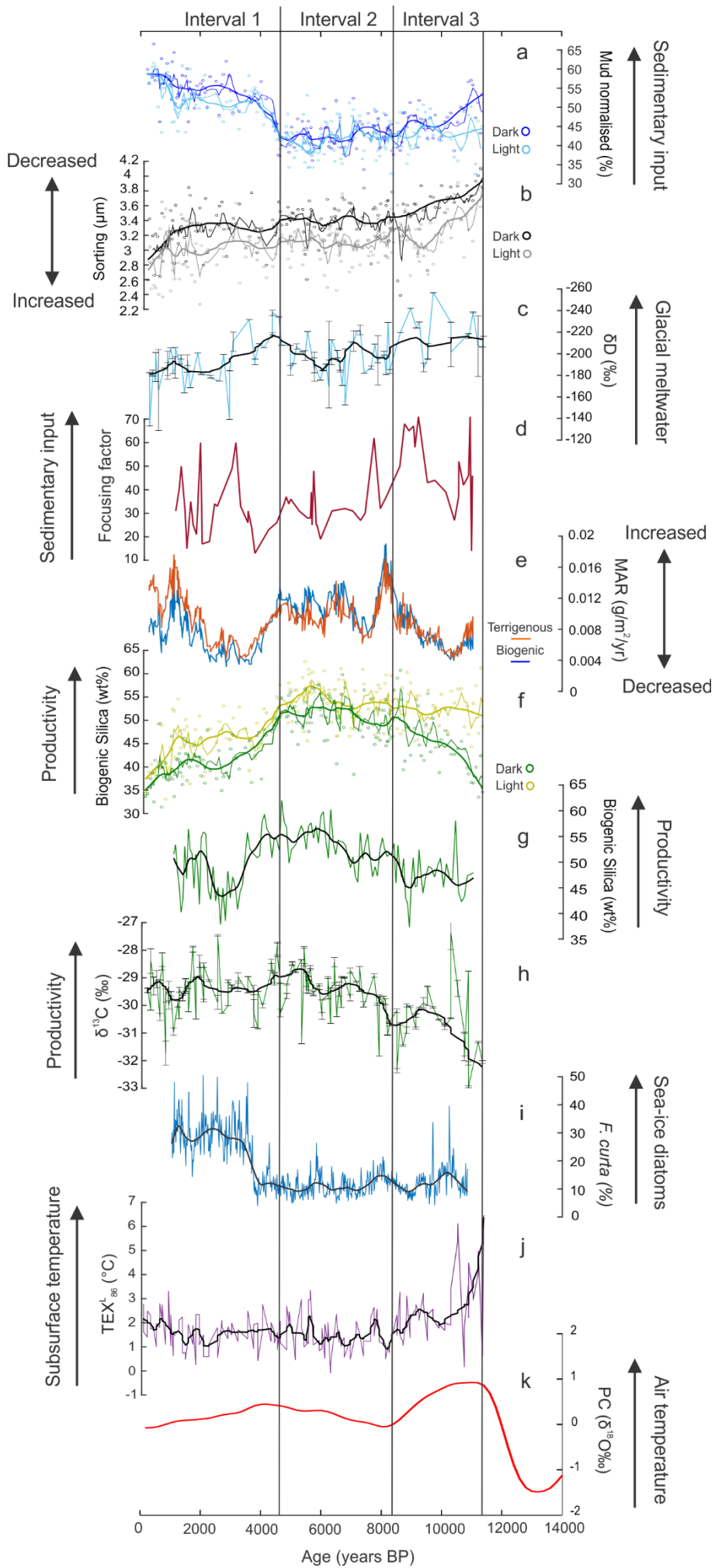


Figure 5.3: (overleaf): (a) Normalised mud% of dark (dark blue) and light (light blue) laminae from U1357B, thin lines are 4 point moving averages and thick lines are a robust version of lowess smoothing (10%); (b) sorting of dark (black) and light (grey) laminae from U1357B, thin lines are 4 point moving averages and thick lines are a robust version of lowess smoothing (10%); (c)  $\delta D_{FA}$  from U1357B, with robust lowess smoothing (10%) (Newton et al., 2015); (d) focusing factor based on the  $^{230}\text{Th}$  excess method from MD03-2601 (Denis et al., 2009a); (e) terrigenous (orange) and biogenic (blue) mass accumulation rates (MARs) from U1357B; (f) biogenic silica% for dark (dark green) and light (light green) laminae from U1357B, thin lines are 4 point moving averages and thick lines are a robust version of lowess smoothing (10%); (g) biogenic silica% from MD03-2601 with robust lowess smoothing (10%) (Panizzo et al., 2014); (h)  $\delta^{13}\text{C}_{FA}$  from U1357B with robust lowess smoothing (10%) (Newton et al., 2015); (i) group abundances from MD03-2601 with robust lowess smoothing (8%) (Crosta et al., 2007); (j) TEXL86 subsurface temperature measurements from U1357B; (k) principal component one (PC1) from four East Antarctic ice cores (Masson-Delmotte et al., 2011). Vertical lines indicate boundaries between Interval 1, 2 and 3.

---

Investigations of grain size distributions offshore Wilkes Land margin by Dunbar et al. (1985) revealed that surface sediments on shallow banks have a grain size distribution that generally exceeds 125  $\mu\text{m}$ , indicating that material in the fine sand and clay range is winnowed from these banks by bottom currents. Analyses of sediment grab samples and seismic imaging of the Mertz Drift and Mertz Bank region by Harris and Beaman (2003) showed an absence of Holocene sediment cover from the inner shelf, apart from the Mertz Drift, supporting the interpretation of winnowing of terrigenous and biogenic material from shallow banks. In addition, the Mertz Drift displays a mounded and drape-and-fill architecture with an elongate geometry, much like the Adélie Drift (Figure 5.2), indicating that sediment advection and focussing by oceanic current is occurring (Harris and Beaman, 2003).

The size of the material winnowed implies that maximum current velocities in the region are greater than 18-20  $\text{cms}^{-1}$ , the minimum velocity required to transport fine sand by intermittent suspension and suspension in poorly sorted glacial marine settings (Singer and Anderson, 1984; McCave and Hall, 2006). Modal peaks in the fine silt, coarse silt and very fine sand size ranges (see Section 4.3) support the hypothesis that these fine sediments are winnowed off the surrounding shallow banks, and indicate that bottom currents eroding sediment off Adélie Bank are generally less than 18  $\text{cms}^{-1}$ . However, a small percent of grains in the fine sand range suggests that brief periods of bottom current velocities exceeding 18  $\text{cms}^{-1}$  could deliver fine sand to the core site. The largest modal peak by volume percent for dark and light laminae is at 16  $\mu\text{m}$ , suggesting that the most common bottom current

velocities flowing across the Adélie Bank are of the order of between 10-15  $\text{cm s}^{-1}$  (Singer and Anderson, 1984; McCave and Hall, 2006).

Dark laminae display coarser modal peaks in the very fine sand and coarse silt, and greater percent of fine sand compared with the light laminae, suggesting greater bottom current strength during deposition of the dark laminae. In the modern day, during spring and summer, export of HSSW from the Adélie Depression is decreased due to water column restratification. Towards late summer and autumn, increased sea ice extent enhances HSSW production (Williams et al., 2008; 2010). Thus in spring, decreased HSSW production and export probably led to decreased velocities of bottom currents flowing across the Adélie Bank, parallel to the coast (Figure 2.11; Section 2.8.3), while in late summer and autumn increased HSSW export would have led to stronger bottom currents which presumably entrained and deposited slightly coarser terrigenous material. Thus, the modal peaks in the grain size distributions could reflect an integrated signal of varying speeds of bottom currents across the Adélie Bank through the season. The lower mean grain size in the light laminae could alternatively be the consequence of a shorter depositional time relative to the darker laminae (as they are seasonal diatom bloom events), and thus provide a shorter time window to be exposed to high intensity currents (i.e. periodic storm events). The flocculation of terrigenous particles in glacial marine, biogenic-rich settings could also contribute to the polymodal signal, although this would probably result in less well defined modes than observed.

Mud-sized terrigenous material could also be delivered by glacial meltwater from the Astrolabe and Zélée glaciers, while the contribution of sand sized grains delivered by glacial meltwater plumes is expected to be minimal due to the distance of the core site from the coast (~40 km). In the Antarctic Peninsula, a significant percentage of sand (7%) delivered by a tidewater glacier in a fjordal setting was recorded 20 km away from the head of the glacier (Domack, 1990), although whether such transport is possible for open waters offshore of the colder polar glaciers in East Antarctica is equivocal. Available multibeam data in the region suggest there is a distinct lack of large proglacial fans at the modern day mouths of the Zélée, Astrolabe and Mertz Glaciers (Beaman et al., 2011), indicating proglacial sediment discharge is minimal. Additionally, direct sediment discharge from the Mertz and Ninnis Glaciers is unlikely to be of significant quantity to sustain dense overflows (i.e. hyperpycnal flows), which could deliver sediment over the Adélie Bank and into the Dumont d'Urville Trough.

Most of the terrigenous material in Interval 2 is thus proposed to have been primarily eroded off the Adélie Bank by bottom currents, related to the easterly flow of the Antarctic Coastal and Slope Front Currents, into the Adélie Drift where sediment would have settled out from suspension. A potential change in sediment source is apparent in the 3.5 kHz seismic profiles, with a notable shift in the drift morphology, whereby the drift thickens at the northern margin of the Dumont d'Urville Trough and pinches out towards the Zélée and Astrolabe glaciers – the opposite to what appears to occur in Interval 3 (Figure 5.2). This change in the drift morphology suggests that Interval 1 and 2 were formed in a similar sediment delivery regime, with less of a local glacier sediment source.

Also notable is the complete lack of IBRD in the grainsize distributions or visual descriptions. Glaciers in the Adélie Land region are inferred to have relatively clean basal layers due to the solid bedrock (see Section 5.1.1), while icebergs calved from large ice shelves and ice tongues, such as the Ross Ice Shelf and advected into the region via the Antarctic Coastal Current usually lack basal debris (Patterson et al., 2014). The lack of IBRD can thus be explained as the consequence of the widespread development of the Ross Ice Shelf after ~8.6 ka (McKay et al. 2016) and no readvances of the Mertz Glacier, and other local outlet glaciers, onto the more erodible Cenozoic substrate of the Wilkes Land continental shelf. The lack of IBRD can also be attributed to Adélie and Mertz Banks (and Mertz Glacier Tongue) shielding Site U1357 from large iceberg passing over the site, as icebergs would have become grounded on the bathymetric highs and deflected north (Massom et al., 2011; Beaman et al., 2011; Figure 2.2, Section 2.3).

Aeolian contribution of terrigenous material is known to be of importance in Antarctic coastal areas affected by katabatic winds (Atkins and Dunbar, 2009; Chewings et al., 2014). However, due to lack of exposed, soft sediment in Wilkes Land (Kleinschmidt and Talarico, 2000) and the distance of the core site from the coast, input of aeolian sediment into the ocean from melting sea ice is likely to be a relatively minor component of the sediment population.

Based on the drift morphology, the prevailing easterly flow of the Antarctic Coastal Current, the coarse sediment grainsize distributions on the Mertz and Adélie Banks, and the overall lack of IBRD in this interval, the bulk of the terrigenous sediment in Interval 2 is interpreted to be the result of sediment advection to the site from the east rather than sediment-laden, glacial meltwater input from local outlet glaciers. The fatty acid biomarker proxies both show a stepped increase in baseline  $\delta^{13}\text{C}_{\text{FA}}$  and  $\delta\text{D}_{\text{FA}}$  values after ~8.2 ka (to >-28‰ and <200‰

respectively) (Figure 5.3), reflecting greater primary productivity and less glacial discharge respectively, while  $\text{TEX}^{\text{L}}_{86}$  also shows a stepped change in subsurface temperatures becoming more stable (ranging between 0-3°C, averaging ~1.5°C). BSi% for both U1357B and MD03-2601 also show an increase of ~15% in Interval 2 compared with Interval 3. The less depleted  $\delta\text{D}_{\text{FA}}$  values support the grain size inferences of an overall reduction in glacial meltwater input relative to Interval 3, suggesting local glacial retreat had largely ceased by this time. The stabilised  $\text{TEX}^{\text{L}}_{86}$  subsurface temperatures and higher productivity indicated by  $\delta^{13}\text{C}_{\text{FA}}$  and BSi% also reflect a water column with less variable input of glacial meltwater, and a less restricted oceanic circulation and water column mixing after ice retreat occurred on Mertz and Adélie Banks. A less turbid water column, combined with enhanced polynya size and mixing of surface and deeper waters helps to explain the enhanced primary productivity (Denis et al., 2009b) and more stable  $\text{TEX}^{\text{L}}_{86}$  subsurface temperatures, as the formation of cool dense shelf waters in the polynya and the establishment of the Antarctic Coastal Current passage over the core site carrying cold and fresh Antarctic Surface Water would have limited MCDW upwelling onto the continental shelf margin (Smith et al., 2012).

### 5.1.3 Interval 1 (late Holocene, ~4.5 ka to present)

Interval 1 is characterised by a rapid increase in mud content at 4.5 ka, coincident with a drop in very fine to fine sand (see Section 4.1.1). The increase in mud coincides with a reduction in MARs (both biogenic and terrigenous), though the terrigenous MAR curve shows higher accumulation rates than biogenic MAR curve. The decrease in biogenic MARs is reflected by a small reduction in fatty acid  $\delta^{13}\text{C}_{\text{FA}}$  (with most values >-29‰, with the exception of a higher productivity interval between 2.5 and 1.7 ka where  $\delta^{13}\text{C}_{\text{FA}}$  values are up to -27.4‰) and a significant decrease in BSi% (~55-35%), suggesting a shift to a lower productivity environment (Figure 5.3). After the rapid increase at ~4.5 ka, the normalised mud% continues to increase through to the present day, but sorting remains the same as Interval 2, until ~1.5 ka, after which it increases towards the present day. This increase in sorting after ~1.5 ka is associated with an increase in biogenic and terrigenous MARs. This could be the consequence of enhanced Antarctic Coastal and Slope Front Currents advecting more sediment into the site, with the relative decrease in BSi% being the consequence of reduced primary productivity. An increase in current strength can be explained by enhanced zonal winds (Renssen et al., 2005), while reduced productivity could be the consequence of sea ice intensification at this time,

which is supported by a rapid and sustained increase in the abundance of the sea ice diatom species, in the nearby core MD03-2601 after 4.5 ka (Crosta et al., 2007).

Notably, the increase in mud% between ~4.5 and 1.5 ka is not associated with an increase in sand% or increase in sorting, however this event is associated with a decrease in biogenic and terrigenous MARs. This suggests that the maximum current strength acting to winnow and advect material from the Mertz and Adélie Banks into the Dumont d'Urville Trough was reduced during this time. A reduction in maximum current strength could potentially be explained by more extensive sea ice, which would act to reduce wind stress on the ocean surface and thus the maximum strength of the easterly flow, despite enhanced zonal easterly winds that are predicted with a cooler Antarctic climate (Shin et al., 2003; Renssen et al., 2005; DeConto et al. 2007).

The start of Interval 1 is characterised by a pulse of depleted  $\delta D_{FA}$  values ( $< -200\text{‰}$ ) between ~4.5 and 3 ka, and a very low variance in subsurface temperatures (~1 to 2°C) in the  $TEX^L_{86}$  record, which has been interpreted to represent increased stratification in the region (Newton, 2015). This suggests that the interpreted baseline shift in sea ice and easterly current strength was associated with an initial glacial meltwater event. This could be explained by the final phases of deglaciation in the Ross Sea, which unlike the Adélie Land region is believed to have experienced continued glacial retreat into the mid-Holocene (Anderson et al., 2014; McKay et al. 2016). This is further addressed in Section 5.2.

## 5.2 Comparisons with other Antarctic records

### 5.2.1 Comparison of U1357B with other records in the Adélie Land region

*F* *F*

To date, the only other core recovered offshore Adélie Land and dated to a high enough resolution to resolve Holocene millennial scale climate variability is the 40 m-long MD03-2601 containing a record back to ~10 ka (Denis et al., 2006; Crosta et al., 2007; Section 2.4). The age of this core is constrained by nine  $^{14}C$  ages on bulk AIO matter and is prone to uncertainties relating to the reworking of older carbon into the sediment column (Mackintosh et al., 2014). This reworking is apparent in MD03-2601 with a raw  $^{14}C$  age of 2350 year at 2 cm depth, which is more than 1000 years older than the anticipated reservoir age in the Southern Ocean (Hall et al., 2010). Additionally, in the published age models there is an

assumption of a linear sedimentation (Crosta et al., 2007; Denis et al., 2009a; b), which on the basis of the U1357B record appears unlikely. Thus, differences of ~1000 year duration in the timing of events between U1357B and MD03-2601 could be explained by age model uncertainties and should be considered in the following discussion.

Denis et al. (2009a) evaluated sedimentary input in the region throughout the Holocene using the  $^{230}\text{Th}$  excess method to determine a sediment focusing factor, which estimates the contribution of lateral sedimentary input, and had been previously applied in the deep ocean (Anderson et al., 2009). Although Denis et al. (2009a) acknowledge complications of using this proxy in a continental shelf setting, as it is reliant on an accurate estimate of sedimentation rate, their results showed a long-term decline in sedimentary input through the Holocene that broadly matches that of U1357B record. The early Holocene saw a decreasing pattern of sedimentary input between ~11 and 8.5 ka, with two events of high terrigenous input dated at ~11-10.3 ka and ~9.4-8.6 ka. These events coincide with the timing of the EAIS deglaciation between ~12 and 8 ka (Mackintosh et al., 2014) and with higher *foraminifera* spp. abundances and lower *diatoms* abundances (recovered from MD03-2601; Crosta et al., 2007; Figure 5.3) leading Denis et al (2009a) to interpret these events as reflecting enhanced glacial meltwater input during the deglaciation. This interpretation is consistent with the observation of a decrease in mud and sand%, and poor sorting in Interval 3 of U1357B which is coincident with the early Holocene warm period recorded in East Antarctica between 11.7 and 9 ka (see Section 2.9.1).

*F* *k*

Between ~7 and 3.5 ka BP the sediment focusing factor is observed to decrease and is interpreted to reflect stabilisation of Adélie Land glaciers during a relatively warm and stable period (Denis et al., 2009a). During this time, *foraminifera* abundances are low and total BSi% (for both MD03-2601 and U1357B) are higher indicating increased primary productivity during a period of decreased sea ice extent. This time period is coincident with the mid-Holocene warm period recorded between ~8 and 4 ka at other East Antarctic sites (see Section 2.9.1). Mud% from U1357B also shows a decreasing trend during this time, however is suggested in this thesis to represent a decrease in bottom currents advecting sediment into the Adélie Drift during a period of decreased sea ice extent, and possibly reduced HSSW formation as suggested by Harris et al. (2001) and Presti et al. (2003).

F

Denis et al. (2009a) also identified a baseline increase in terrigenous input from the  $^{230}\text{Th}$  excess method after 3.8 ka. This time interval is associated with higher abundances and lower BSi% (Figure 5.3) suggestive of colder temperatures and higher sea ice concentrations, which led Denis et al. (2009a) to interpret the increase in terrigenous input as representative of local glacier readvances. Decreased biogenic accumulation and increased mud and IBRD content were also recorded at the top of cores recovered from the Mertz Trough (McMullen et al., 2006). Due to uncertainty in dating from this location (see Section 2.4) the timing for this is roughly bracketed between ~6 and 4 ka. McMullen et al. (2006) suggested a re-advance of the Mertz and Ninnis (further east of Mertz Glacier) Glaciers during a switch to colder conditions as a possible source for the increase in clay and IBRD, and an increase in sea ice extent, which lowered primary production as a reason for lower biogenic accumulation. The above explanations conflict with the interpretation reached in this thesis from the U1357B datasets. Even though there is an increase in mud% at all sites, there is no notable increase in IBRD, sand%, or decrease in sorting that would be predicted with increased glacial proximity. In addition, the biogenic and terrigenous MARs for U1357B both show a rapid decrease during this time. The fact that the increased mud% in U1357B is associated with a large pulse in  $\delta\text{D}_{\text{FA}}$  (i.e. glacial meltwater) at this time also argues against a glacial advance. Thus, this interval is primarily interpreted to represent a reduced flow of the Antarctic Coastal and Slope Front Currents due to a more extensive sea ice cover, which resulted in an enhanced advection of finer mud-sized material into the Adélie Drift relative to coarser-sized particles.

As noted in the previous section, these data can be reconciled by a phase of accelerated deglaciation of the WAIS in the Ross Sea, bringing freshwater into the Adélie Land region during the late Holocene (McKay et al., 2016). I propose this would have led to the enhanced stratification and sea ice noted in the diatom records and this event may have been pivotal for the onset of cold 'Neoglacial' conditions in the region. Such small-scale stratification events due to freshwater input from the Ross Ice Shelf have been observed in the modern day Ross Sea (Smith et al., 2008; 2012). In addition, the expansion of the Ross Sea polynya during the late Holocene due to enhanced katabatic flow (Cunningham et al., 1999) would have enhanced sea ice growth and AASW formation in the Ross Sea and this would have had a "downstream" response in offshore Adélie Land. Advection of the less saline AASW and the

disintegrated pack ice via the Antarctic Coastal Current from the Ross Sea region would have resulted in a freshening and contributed to the enhanced sea ice production offshore Adélie Land. This freshening is not apparent in the fatty acid  $\delta D_{FA}$  records, as that is only a measure of highly depleted glacial meltwater, not sea ice melt (Newton 2015).

The sedimentary proxies from MD03-2601 and U1357B show a systematic coherency. However, the focusing factor is only a measure of enhanced lateral sediment transport and is thus potentially linked to current transport rather than glacial meltwater input. The long-term decreasing trend of the focusing factor may reflect limited sampling of the MD03-2601 core (60 samples) and the fact that this proxy is measured from bulk terrigenous sediment, the relative abundance of which is the inverse of BSi% at the site. Based on this, the overall terrigenous fraction for U1357B shows a dominantly decreasing trend from  $\sim 11.3$  to 4.5 ka, after which an increasing trend is observed (inverse of the U1357B BSi% trend; Figure 5.3). The long-term decrease of the focusing factor thus represents a trend in relative proportions rather than absolute quantities, which may have resulted in a misleading interpretation.

Coarser silt modes of dark laminae in Intervals 1 and 2 are tentatively inferred to represent periods of increased bottom currents across the Adélie Bank due to enhanced HSSW formation (see Section 5.1.2). Therefore, time intervals characterised by colder temperatures and increased sea ice concentrations could potentially lead to enhanced HSSW flows across the Adélie Bank as is observed during the yearly annual cycle in the present day (see Section 2.8.3). Cascading gravity plumes of HSSW could thus have acted to entrain mud-sized terrigenous sediment from the Adélie Bank during the deposition of Interval 1, along with the reduced zonal flows of the Antarctic Coastal and Slope Front Currents. Therefore, inferences of increased HSSW formation during the late Holocene “Neoglacial” (post 4 ka), as made by Harris et al. (2001) and Presti et al. (2003), are in broad agreement (considering age model uncertainties, see Section 2.4) with enhanced mud advection to Site U1357B during this time. Modern day hydrographic observations reveal that shelf water formed in the Dumont d’Urville Trough does not contribute to Adélie Land Bottom Water and HSSW has not been detected within the Adélie Basin (Section 2.8.3). Inferences made about bottom water formation from cores located within the Adélie Basin should thus be treated with caution. However, Site U1357B lies directly in the path of bottom currents coming from the Adélie Depression, and therefore overflows of HSSW spilling over the Adélie Bank may have contributed to terrigenous sediment advection to the core site, during the colder time

interval. Comparison with other proxies (e.g. diatom assemblages) from U1357B will help determine if this inference is correct.

### 5.2.2 Far field Antarctic records

Correlation of the grain size record derived in this thesis with other U1357B and MD03-2601 records of climate variability offshore Adélie Land has revealed the following pattern of Holocene climate evolution: a warm early Holocene (~11.4-8.2 ka), a stable warm mid-Holocene between ~8.2 and 4.5 ka and a colder period from 4.5 ka to the present. This pattern correlates well with a synthesis of four East Antarctic  $\delta^{18}\text{O}$  ice core records, which have been interpreted to represent changes in air temperature (Masson-Delmotte et al., 2011; Figure 5.4). The derived temperature curve shows rapidly rising temperatures from 13 to 9 ka, a cooling between 9 and 8 ka, gradual warming between 8 and 4 ka, after which temperatures begin to decrease until the present (Figure 5.3). This relationship suggests that oceanic surface water changes at the Adélie margin are recorded in atmospheric temperatures, recorded in the high elevation ice cores, and there is scope for further work to investigate these atmospheric and oceanic links.

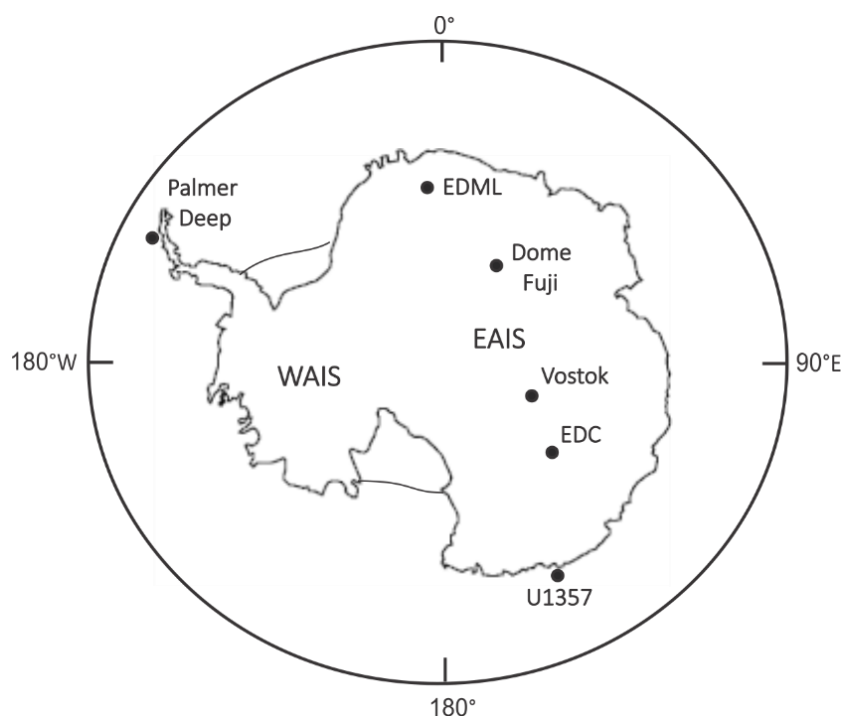


Figure 5.4: (overleaf): Shows the location of four ice cores used by Masson-Delmotte et al. (2011) to make a synthesis of  $\delta^{18}\text{O}$  records representative of air temperature changes through the Holocene across East Antarctica; Site U1357 and the Palmer Deep record; East Antarctic Ice Sheet (EAIS); West Antarctic Ice Sheet (WAIS); EPICA Dronning Maud Land (EDML); EPICA Dome C (EDC). Black dots represent the location of the ice cores.

---

Well-dated marine sedimentary cores from Antarctic continental shelves, which record the transition from the LGM to the Holocene and span the entire Holocene time interval, are still rare. A diatom ooze recovered from Palmer Deep (ODP site 1098; Figure 5.4) in the northwest of Antarctic Peninsula contains a high-resolution, 50 m record spanning the past  $\sim 13$  ka. Magnetic susceptibility (proxy for terrigenous input), mass accumulation rates, IBRD and diatom assemblage records from the well dated (51 carbon dates) marine sediment core have been used to reconstruct Holocene climate evolution for the region (Domack et al., 2001; Leventer et al., 2002). From the chronological constraints and the above mentioned proxies, four prominent Holocene time intervals were proposed: (1) a deglacial episode of high primary production and iceberg rafting from 13.2 to 11.4 ka; (2) a climatic cooling (reversal) between 11.4 and 9 ka; (3) a mid-Holocene climatic optimum from 9 to 3.3 ka; and (4) the Neoglacial between 3.3 ka to the present.

These time intervals are broadly similar to the pattern of Holocene climate change suggested for East Antarctica based on the synthesis of four ice core records (Masson-Delmotte et al., 2001) and the U1357B records discussed in this thesis. There is a discrepancy in the timing of the early Holocene cooling event which occurs at  $\sim 9$ -8 ka in East Antarctica, however is recorded between  $\sim 11.4$  and 9 ka in Palmer Deep and the beginning of the mid-Holocene warm period which occurs 1 kyr earlier and continues for 1 kyr longer in the Palmer Deep than in East Antarctica. The discrepancies in the climatic records observed between East Antarctica and the Antarctic Peninsula could be explained by the spatial heterogeneity in the intensities of the local and external climatic and oceanic forcing mechanisms. Palmer Deep is located more than 6000 km to the northeast of Adélie Land at the most northerly part of the Antarctic continent, and as such it is more subject to mid-latitude influences of the southern westerly winds and is exposed to strong marine influences from the South Pacific and South Atlantic Oceans. In addition the Antarctic Peninsula acts a barrier to the flow of ACC, restricting its passage through the Drake Passage. As such, the continental shelf of the peninsula is likely to

be directly affected by any variations in the flow of the ACC (Anderson, 1999; Bentley et al., 2009), whereas the U1357B record is inferred to have a strong Ross Sea and East Antarctic Ice Sheet influence. Age model uncertainties may also account for some of the differences, as the published records for ODP site 1098 age model is based on a 3<sup>rd</sup> order polynomial regression through 51 radiocarbon dates, rather than the Bayesian approach used for U1357B (Dunbar et al., in prep). However, the broad change of Holocene climate evolution across Antarctica appears to follow a similar pattern suggesting that the different regions of Antarctica are responding to similar climatic forcings.

Domack et al. (2001) also suggested that a period of cold conditions starting at 700 years BP and ending at 100 years BP could be a signal equivalent to the Little Ice Age observed in the Northern Hemisphere during this time. Geochemical analyses of two ice cores drilled in the western Ross Sea sector infer slightly warmer sea surface temperatures and reduced sea ice extent in the Ross Sea between 1000 and 700 years BP and ~2°C cooler temperatures, increased sea ice extent and stronger katabatic winds ( $\geq 55 \text{ ms}^{-1}$ ) between 700 and 200 years BP (Bertler et al., 2011; Rhodes et al., 2012). Mud% for U1357B shows an increased variance after 1600 years BP (Figure 5.3), with decreasing mud% from 1600 to 1000 years BP, indicating reduced sediment advection to the site. From 1000 years BP, mud% shows an increasing trend, indicative of enhanced sediment advection to the site, which flattens out at 300 years BP. Whether these signals are related to the Medieval Warm Period and the Little Ice Age or are representative of cycles related to internal ocean and/or solar variability discussed below should be investigated in future work.

### 5.2.3 Millennial-to-centennial climate variability

Multi-taper (MTM) analyses of the greyscale data (a measure of the laminae frequency) are noisy. However, they reveal a lack of an obvious annual cycle, and instead display peaks in the 2-7 year band, which fall into the known ENSO frequencies (Turner, 2004; Figure 4.13). ENSO influence offshore Adélie Land in the late Holocene has been recognised by Costa et al. (2007) and Gregory et al. (2012) who imply similar frequencies through MTM analysis of the Barium (Ba) content and diatom assemblages (productivity proxies), respectively, from sediment cores collected offshore Adélie Land (U1357B, MD03-2601 Figure 5.3 and JPC17B 66°24.852'S, 140°25.164'E [Leventer et al., 2006]). Research on ENSO activity in the Holocene through the use of precipitation proxies such as grain size and hydrogen isotope ratios in the Galápagos

Islands and Ecuador reveal that ENSO was weak in the early Holocene, but increased in intensity and frequency throughout the middle and late Holocene, with stronger and more frequent El Niño events occurring in the latter time interval (Moy et al., 2002; Conroy et al., 2008; Zhang et al., 2014).

Sea ice offshore Adélie Land is impacted by modern variations in the ENSO, with El Niño (La Niña) events inducing (inhibiting) sea ice growth (see Section 2.6.2). If this was the case offshore Adélie Land throughout the Holocene, time periods dominated by El Niño events should be characterised by lower rates of biogenic accumulation and lower laminae counts per m, as greater sea ice extent and/or duration at the core site would limit the area of open water for primary production. This relationship appears to hold throughout the Holocene as periods of low biogenic accumulation are correlated with time intervals dominated by an increased frequency of El Niño events when the ENSO frequency curve derived by Zhang et al. (2014), based on hydrogen isotope ratio of lipids produced by the green alga

which blooms during El Niño years in the Galápagos Islands, is compared with U1357B terrigenous and biogenic MARs (Figure 5.5). Laminae counts per m also match this trend with time intervals of higher light laminae counts (i.e. large bloom events) correlating with time periods characterised by greater occurrences of La Niña events (Figure 5.5). The correlation between the records is particularly evident in the late Holocene, suggesting that the ENSO may have exerted a significant control on Holocene climate variability in the region during this time.

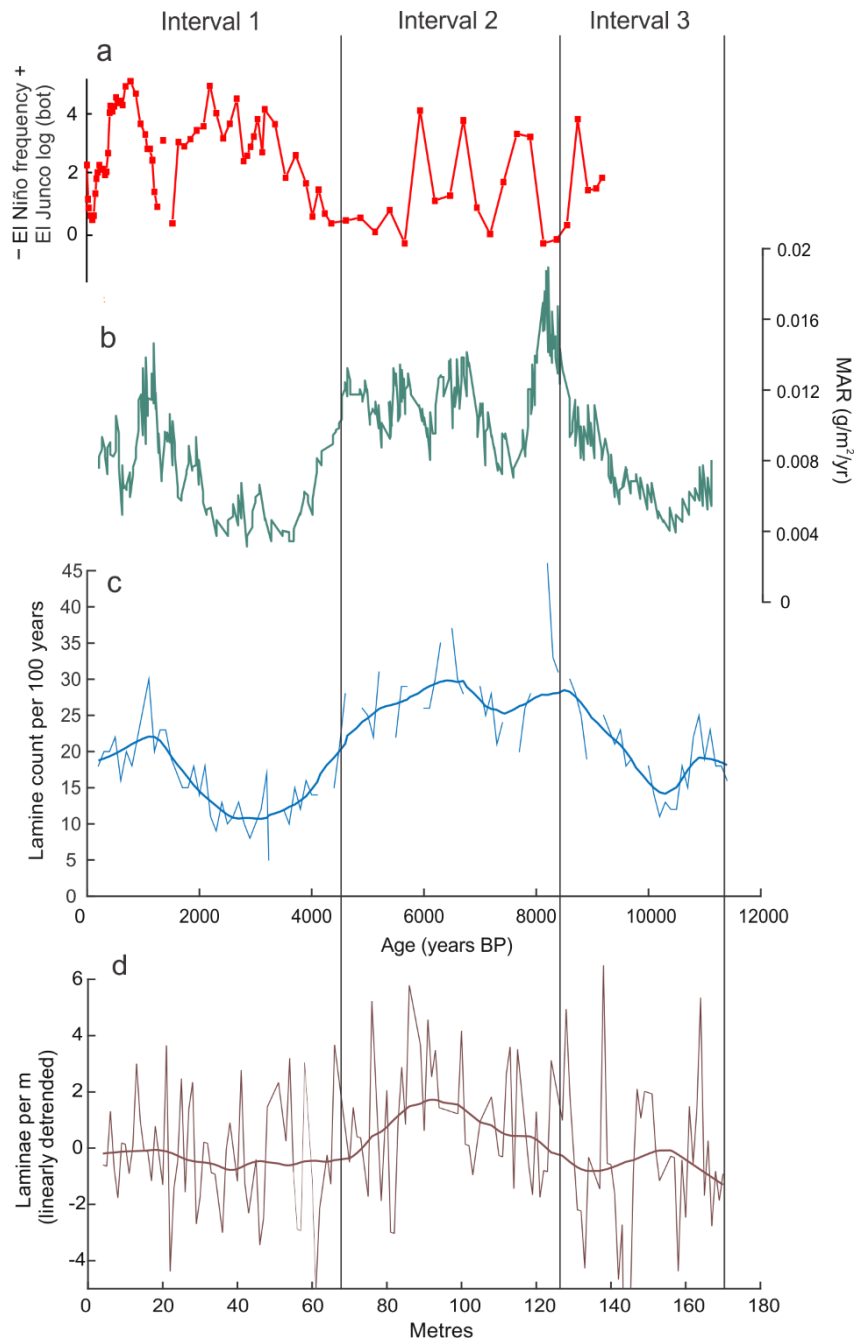


Figure 5.5: (a) Botryococcene concentrations in El Junco sediment, Galápagos Islands (highly branched isoprenoid hydrocarbons produced by *Botryococcus braunii*) indicative of El Niño frequency (Zhang et al., 2014); (b) mass accumulation rate (MAR) of biogenic sediment at Site U1357B; (c) laminae counts per 100 years for U1357B; (d) linearly detrended laminae per metre for U1357B.

Variations in the ENSO have been closely linked with orbitally induced changes in seasonal insolation (i.e. precessional forcing), which have been attributed to amplifying the ENSO cycle in the middle and late Holocene (Clement et al., 2000; Cane, 2005; Conroy et al., 2008). MTM

spectra of the greyscale data show an increase in the ENSO band frequencies between ~9 and 7.4 ka and after ~4.2 ka (Figure 4.13; Section 4.5) providing support for the above interpretation. These time intervals are also characterised by an increase of cycles at ~50, 33, 20 and 10 year periods. By changing the seasonal insolation between low and high latitudes and consequently the meridional sea surface temperature gradient, precession is also thought to exert an important control on the position of the Southern Hemisphere westerly wind belt (Renssen et al., 2005; Gomez et al., 2011). Thus, these longer periodicities may be indicative of changes in the SAM on decadal timescales (Thompson and Wallace, 2000; Jacobs and Giulivi, 2010) or may represent cycles consistent with solar variability (Stuiver et al., 1993; Cook et al., 1996; 2000) which have previously been noted in Antarctic paleoceanographic records (Domack et al., 2001; Warner and Domack, 2002; Costa et al., 2007). Furthermore, a connection between ENSO and SAM during the Holocene has been established in the mid-latitude Pacific, alternating at a millennial timescale, whereby the ENSO teleconnections to the extratropics strengthen when ENSO and SAM are in phase (i.e. La Nina with positive SAM; Gomez et al., 2011). A gradual change from a negative to a positive SAM index over the past 1000 years has been noted, coincident with an increasing frequency of ENSO events in the late Holocene (Abram et al., 2014). Based on correlation of diatom assemblages with ENSO and SAM indices, Gregory (2012) suggested that a multidecadal to centennial variability in this connection may exist in the middle and late Holocene. The presence of ENSO band frequencies with the ~50, 33 and 20 year cycles in U1357B suggests that this may well be the case throughout the Holocene.

Periodicities in the 20-30 year band have also been associated with the Pacific Decadal Oscillation (PDO) which modulates climate in the North Pacific, with positive PDO events exhibiting similar climatic conditions to El Niño (Zhang et al., 1997; Gedalof et al., 2002). The PDO has been shown to modulate climatic teleconnections between the north and equatorial Pacific during El Niño and La Niña events (Brown and Comrie, 2004). The 33 and 20 year cycles may thus also represent ENSO expression in the Antarctic, modulated by the PDO.

Currently there is some consensus between models that the recent trend in increasing El Niño frequency will experience little change (Meehl et al., 2007), though some models suggest a further increase in the amplitude and frequency of El Niño events with increasing global temperatures (Santoso et al., 2013). With continued greenhouse gas increases, it is predicted that the trend towards a positive SAM in summer will continue (Marshall et al., 2004; Cai et

al., 2005), though it may be mitigated to some extent by recovery of the ozone hole (Shindell and Schmidt, 2004; Cai and Cowan, 2007). If the projected trends for ENSO and SAM continue as predicted by some models mentioned above, the teleconnection between the two mechanisms may strengthen, with implications for sea ice extent, bottom water formation and Antarctic ice sheet stability.

MTM analysis of the NGR content in U1357B picked out cycles in the 40-60 year band, with a significant peak centred at 55 years. Wavelet analysis showed that these cycles persist throughout the entire record. Campagne et al. (2015) found a ~70 year periodicity in at least the last 250 years associated with large calving events of the Mertz Glacier. These cycles may thus represent calving events, which resulted in slightly increased mud advection to the Adélie Drift. However, similar periodicities in the 50-70 year bands have been identified in a magnetic susceptibility record from the Antarctic Peninsula and in tree ring records from Tasmania, South Pacific. These bands have been related to the expansion and contraction of the circumpolar vortex around Antarctica, which is also known to have variations at this time frequency (Domack et al., 2001; Cook et al., 1992; 1996). The cycles of 40-60 years may thus reflect the Adélie land glaciers response to a combination of processes such as internal mass balance dynamics and an atmospheric variability signal, both of which impact coastal sea ice growth and glacier extent.

Cycles picked up by spectral analysis in the NGR and sand content at 163, 180, 250 and 270 years are observed to have a strong signal in the early and late Holocene and are similar to the periodicities of known solar variability of ~200 years (Stuiver and Braziunas, 1993; Cook et al., 1996). Periodicities in the 200-300 year band, attributed to solar variability, have been identified in terrigenous and biogenic proxies from the Antarctic Peninsula in the middle and late Holocene (Leventer et al., 1996; Domack et al., 2001; Warner and Domack, 2002). Cycles of 590-625, 1200-1600 and 2200-2400 years in duration are also evident in the NGR and sand content throughout the Holocene. The 590-625 year cycle has been recorded in tree ring records from the south and northwest Pacific and is thought to originate from an internal mode of ocean oscillation related to North Atlantic deep water formation, however solar influences have also been suggested (Stuiver and Braziunas, 1993; Cook et al., 2000). The significance of this cycle in Antarctica is yet to be proven. The 1200-1600 year cycle is a common feature in Holocene climatic records, however its significance and origin are still under debate between solar forcing and an independent mode of internal ocean oscillation (Bond et al.,

1997; 2001; Debret et al., 2007). The 2200-2400 year cycle is close in periodicity to a well-known cycle of Holocene solar variability with a period of 2400 years (Damon and Sonett, 1991; Vasiliev and Dergachev, 2002). This cycle has been identified in Holocene biogenic records in the Antarctic Peninsula and offshore Adélie Land and is suggested to regulate primary productivity through amplification of various ocean-atmosphere processes such as heat exchange, production of cloud cover and upwelling dynamics (Leventer et al., 1996; Newton, 2015).



## Chapter 6: Conclusions and Future Work

### 6.1 Conclusions

An assessment of sedimentary transport mechanisms and Holocene climate variability was undertaken offshore Adélie Land, East Antarctic margin. This was achieved through: [i] analysis of the U1357B grain size data derived in this thesis; [ii] correlation of the grain size characteristics with other U1357B datasets; [iii] image analysis of U1357B core photographs and through; [iv] spectral analyses of the grain size and image analyses results.

- A total of 341 samples were analysed using the Laser Diffraction Particle Size Analyser. The results were interpolated onto an age model developed by Prof Rob Dunbar (Stanford University, USA), producing an 11.4 kyr record with a sampling resolution of  $66\pm 33$  years. The majority of grain size distributions fall within the poorly sorted category of Folk and Ward (1957), but some very poorly sorted samples are present before  $\sim 11$  ka. The mean grain size and sorting trends show a long-term up core decrease and increase, respectively. The sorting trend shows three distinct intervals. Between 11.4 and 8 ka, sorting persistently increases, followed by a relatively stable distribution until  $\sim 2$  ka, after which sorting again increases.
- First order variations are also readily identified in the sand ( $>63 \mu\text{m}$ ) and mud ( $<63 \mu\text{m}$ ) content of the record. Three distinct intervals are identified, with an overall trend of decreasing sand% up core ranging from  $\sim 20$ - $10\%$  between  $\sim 11.4$  and 8.2 ka,  $\sim 15$ - $10\%$  between 8.2 and 4.5 ka, and dropping sharply to  $\sim 10$ - $5\%$  at  $\sim 4.5$  ka until present time. The mud% shows the opposite trend.
- The terrigenous and mass accumulation rates (MARs) show increasing trends from 11.4 to 8.2 ka, after which point a sudden drop occurs. From  $\sim 7.8$  to 4.5 ka both MAR curves remain relatively stable. From  $\sim 4.5$  to 3.8 ka, the MARs show a sudden drop and remain relatively low until 2 ka, after which a sharp increase in values is observed. The terrigenous and biogenic MAR curves closely follow one another, however the long-term trends of the two components are opposite, with the biogenic MAR displaying an overall weak long-term decline while the terrigenous MAR shows a weak

long-term increase. The decoupling between the two trends is particularly evident after 4.5 ka.

- Based on the above grain size characteristics of the 11.4 kyr dataset three distinct lithologic intervals were identified: 1) a laminated muddy diatom ooze deposited from ~4.5 ka to the present, 2) a laminated diatom ooze with reduced terrigenous input deposited between ~4.5 and 8.2 ka, and 3) a muddy diatom ooze with an IBRD influence deposited between ~8.2 and 11.4 ka.
- Through correlation of the grain size characteristics with the  $\delta^{13}\text{C}_{\text{FA}}$  and BSi% (primary productivity proxies),  $\delta\text{D}_{\text{FA}}$  (glacial meltwater influence proxy) and  $\text{TEX}^{\text{L}}_{86}$  (subsurface temperature proxy) U1357B datasets, changes to the depositional environment at the core site were interpreted. Interval 3 is characterised by low primary productivity, poor sorting and high sand% and glacial meltwater influence, and is interpreted to have been deposited in a calving bay depositional environment via meltwater plumes and ice-berg rafting.  $\text{TEX}^{\text{L}}_{86}$  data suggests an important influence of MCDW onto the continental shelf during this time, coincident with the early Holocene warm period recorded at other East Antarctic sites between ~11.7 and 9 ka. Interval 2 is characterised by absence of IBRD, increase in paleoproductivity and a significant increase in MARs, and is inferred to have been deposited in open marine conditions during the mid-Holocene Climatic Optimum. It is suggested in this thesis that the local glaciers had retreated to their present day grounding line by ~8.2 ka, and from then on sediment was being delivered to the core site primarily via a suspended sediment load in the Antarctic Coastal and Slope Front Currents, largely through erosion of the surrounding banks.
- Interval 1 is characterised by a rapid increase in mud content at 4.5 ka, coincident with a pulse of glacial meltwater and a sudden decrease in biogenic and terrigenous MARs. This interval is interpreted to represent enhanced mud deposition under a reduced flow regime of the Antarctic Coastal and Slope Front Currents after deglaciation in the Ross Sea was largely completed (Anderson et al., 2015; McKay et al. 2016). It is suggested here that this was the consequence of the final phase of deglaciation in the Ross Sea leading to the modern regime of polynya-mixing, sea ice and AASW

production becoming established in the region. Advection of glacial melt and AASW into the Adélie Land region via the Antarctic Coastal Current is inferred to have led to increased sea ice growth in the region, as evident by increased concentration of the sea ice diatom *Thalassiosira antarctica* in MD03-2601. Increased sea ice concentrations consequently led to reduced primary production (Newton, 2015) and to a decrease in maximum current strength advecting sediment to the site. The development of the modern-style water masses in the region appears to have been pivotal for the onset of cold 'Neoglacial' conditions in East Antarctica.

- Correlation of the U1357B grain size record with other records of climate variability from U1357B and a nearby core, MD03-2601, has revealed the following pattern of Holocene climate evolution: a warm early Holocene (~11.4-8.2 ka), a stable warm mid-Holocene between ~8.2 and 4.5 ka and a colder period from 4.5 ka to the present. This pattern broadly matches Holocene climate evolution recorded from ice cores in East Antarctica and from a sedimentary core recovered in the Antarctic Peninsula, suggesting that the different regions of Antarctica are responding to similar climatic forcings throughout the Holocene.
- Line scanned core photographs were converted to a greyscale value. Counting of light laminae (biogenic bloom events) was carried out by overlaying the grey-depth scale with the greyscale values on the core photographs and visually picking high values on the greyscale curves (i.e. peaks), as well as visual confirmation of a light laminae in the core photograph. The laminae count per 100 years plotted against time and depth shows a clear resemblance with the biogenic MAR curve, with increased laminae deposition/preservation occurring during periods of higher sedimentation rate.
- Spectral analysis of the greyscale values identified significant peaks in the 2-7 year band which fall into the known El Niño Southern Oscillation (ENSO) frequencies (Turner, 2004b). Modern observations of sea ice extent in the Ross Sea region reveal that El Niño events induce expansion of coastal sea ice (Gregory, 2012). Comparison of the ENSO frequency curve derived by Zhang et al. (2014) with the laminae count per 100 years and the biogenic MAR curve from U1357B reveals that periods dominated by El Niño (La Niña) events are characterised by lower (higher) laminae

counts and MARs, suggesting that the modern relationship between ENSO and sea ice extent appears to have held throughout the Holocene.

- Spectral analysis of the sand and NGR content of U1357B picked out cycles in the 40-60 year band, with a significant peak centred at 55 years, persisting throughout the Holocene. These cycles may be related to internal mass balance dynamics of the Mertz Glacier (Campagne et al., 2015) or to the expansion and contraction of the circumpolar vortex around Antarctica, which is also known to have variations at this time frequency (Domack et al., 2001; Cook et al., 1992; 1996). Cycles in the 200-300 and 2200-2400 year bands were identified to have a strong signal in the early and mid-Holocene and have been attributed to solar variability (Cook et al., 1996; Leventer et al., 1996; Domack et al., 2001; Vasiliev and Dergachev, 2002). Cycles in the 590-625 and 1200-1600 year bands have a strong signal through the entire record and are common features of Holocene climatic records, however the origin of these cycles is still under debate between solar forcing and an independent mode of internal ocean oscillation (Cook et al., 2000; Bond et al., 1997; 2001; Debret et al., 2007).

## 6.2 Future Work

Interpretations made in this thesis remain working hypotheses, particularly the interpretations associated with the 4.5 ka event. Improved understanding of the processes that have formed the Adélie Drift will help to test these hypotheses.

- Improved multibeam/seismic coverage over the drift area will help to characterise the drift morphology relative to the prevailing oceanographic currents and local glaciers.
- Integration of local sediment trap data with oceanographic measurements such as temperature-velocity and suspended particulate matter profiles will help with the understanding of sediment deposition from local sources, such as through erosion of the Mertz and Adélie Banks, and possibly meltwater plumes from local glaciers. It will also enable examination of distant outlet sources eastward of the drift, advected into the region as suspended sediment load.

- Future work could also focus on improving the characterisation of the ENSO periodicity identified in the core through image and spectral analyses and its influence on Antarctic Holocene climate. This could be done through an increased resolution of the grain size record and an X-ray computed scan of the core (or selected intervals) to assess the errors associated with the greyscale counting. Line-scan XRF comparison to the laminae could provide a powerful method to identify potential ENSO and decadal to millennial periodicity in the core. Any shifts in elemental abundances at 4.5 ka could also be useful for the interpretation of the increased mud supply to the core site at this time.



## Appendices

### **Following Appendices are attached on Disc 1:**

Appendix 1A: Sample depths, ages and lamina types

Appendix 1b: Sample weights prior to and after chemical treatment

Appendix 2A: Raw output data from the Laser Particle Size Analyser for all samples

Appendix 2B: GRADISTAT statistics for all samples

Appendix 3A: GRADISTAT statistics for dark and light laminae of Interval 1

Appendix 3B: GRADISTAT statistics for dark and light laminae of Interval 2

Appendix 3C: GRADISTAT statistics for dark and light laminae of Interval 3

Appendix 4: Calculations of linear sedimentation and mass accumulation rates

Appendix 5: Normalised values (to the overall terrigenous content) of sand and mud

Appendix 6: Additional U1357B datasets ( $\delta^{13}\text{C}_{\text{FA}}$ ,  $\delta\text{D}_{\text{FA}}$ ,  $\text{TEX}^{\text{L}}_{86}$ ,  $\text{BSi}\%$ )



## References

- Abram, N. J., Mulvaney, R., Vimeux, F., Phipps, S. J., Turner, J., & England, M. H. (2014). Evolution of the Southern Annular Mode during the past millennium. *K* *k* (7), 564-569.
- Ackley, S., & Sullivan, C. (1994). Physical controls on the development and characteristics of Antarctic sea ice biological communities—a review and synthesis. *F* (10), 1583-1604.
- Adolphs, U., & Wendler, G. (1995). A pilot study on the interactions between katabatic winds and polynyas at the Adélie Coast, eastern Antarctica. *J*, 307-307.
- Allan, R. J. (2000). ENSO and climatic variability in the past 150 years. *K* *Rk* , 3-55.
- An, S.-I., & Jin, F.-F. (2004). Nonlinearity and Asymmetry of ENSO\*. *k* (12), 2399-2412.
- Anderson, J. B. (1999). *k* : Cambridge University Press.
- Anderson, J. B., Conway, H., Bart, P. J., Witus, A. E., Greenwood, S. L., McKay, R. M., . . . Jakobsson, M. (2014). Ross Sea paleo-ice sheet drainage and deglacial history during and since the LGM. *J* , 31-54.
- Anderson, J. B., Wellner, J. S., Lowe, A. L., Mosola, A. B., & Shipp, S. S. (2001). Footprint of the expanded West Antarctic Ice Sheet: ice stream history and behavior. *J* (10), 4-9.
- Anderson, R. F., Ali, S., Bradtmiller, L. I., Nielsen, S. H. H., Fleisher, M. Q., Anderson, B. E., & Burckle, L. H. (2009). Wind-Driven Upwelling in the Southern Ocean and the Deglacial Rise in Atmospheric CO<sub>2</sub>. *J* (5920), 1443-1448.
- Arrigo, K. R., & Thomas, D. N. (2004). Large scale importance of sea ice biology in the Southern Ocean. *J* (04), 471-486.
- Arrigo, K. R., & Van Dijken, G. L. (2003). Phytoplankton dynamics within 37 Antarctic coastal polynya systems. *J* (C8).
- Arrigo, K. R., van Dijken, G. L., & Bushinsky, S. (2008). Primary production in the Southern Ocean, 1997–2006. *J* (C8).
- Arrigo, K. R., Worthen, D., Schnell, A., & Lizotte, M. P. (1998). Primary production in Southern Ocean waters. *J* (C8), 15587-15600.
- Atkins, C. B., & Dunbar, G. B. (2009). Aeolian sediment flux from sea ice into Southern McMurdo Sound, Antarctica. *J* (3), 133-141.
- Ayliffe, L. K., Gagan, M. K., Zhao, J.-x., Drysdale, R. N., Hellstrom, J. C., Hantoro, W. S., . . . Cowley, J. A. (2013). Rapid interhemispheric climate links via the Australasian monsoon during the last deglaciation. *K* *k k* .
- Baldwin, M., Gray, L., Dunkerton, T., Hamilton, K., Haynes, P., Randel, W., . . . Horinouchi, T. (2001). The quasi-biennial oscillation. *J* (2), 179-229.
- Beaman, R. J., & Harris, P. T. (2005). Bioregionalization of the George V Shelf, East Antarctica. *J* (14), 1657-1691.
- Beaman, R. J., O'Brien, P. E., Post, A. L., & De Santis, L. (2011). A new high-resolution bathymetry model for the Terre Adélie and George V continental margin, East Antarctica. *J* (01), 95-103.
- Beans, C., Hecq, J.-H., Koubbi, P., Vallet, C., Wright, S., & Goffart, A. (2008). A study of the diatom-dominated microplankton summer assemblages in coastal waters from Terre Adélie to the Mertz Glacier, East Antarctica (139 E–145 E). *J* (9), 1101-1117.

- Bentley, M. J., Hodgson, D., Smith, J., Cofaigh, C. Ó., Domack, E., Larter, R., . . . Hjort, C. (2009). Mechanisms of Holocene palaeoenvironmental change in the Antarctic Peninsula region. *Journal of Quaternary Science*, *24*(1), 51-69.
- Bertler, N., Naish, T., Mayewski, P., & Barrett, P. (2006). Opposing oceanic and atmospheric ENSO influences on the Ross Sea Region, Antarctica. *Journal of Geophysical Research*, *111*, 83-86.
- Bertler, N. A., Barrett, P. J., Mayewski, P. A., Fogt, R. L., Kreutz, K. J., & Shulmeister, J. (2004). El Niño suppresses Antarctic warming. *Journal of Geophysical Research*, *109*, (15).
- Bertler, N. A. N., Mayewski, P. A., & Carter, L. (2011). Cold conditions in Antarctica during the Little Ice Age - Implications for abrupt climate change mechanisms. *Journal of Geophysical Research*, *116*(1-2), 41-51.
- Bianchi, G. G., & McCave, I. N. (1999). Holocene periodicity in North Atlantic climate and deep-ocean flow south of Iceland. *Journal of Geophysical Research*, *104*(6719), 515-517.
- Bijl, P. K., Bendle, J. A., Bohaty, S. M., Pross, J., Schouten, S., Tauxe, L., . . . Olney, M. (2013). Eocene cooling linked to early flow across the Tasmanian Gateway. *Journal of Geophysical Research*, *118*(24), 9645-9650.
- Bindoff, N. L., Rintoul, S. R., & Massom, R. (2000). *Journal of Geophysical Research*, *105*(k), k. Paper presented at the Papers and Proceedings of the Royal Society of Tasmania.
- Blaauw, M., & Christen, J. A. (2011). Flexible paleoclimate age-depth models using an autoregressive gamma process. *Journal of Geophysical Research*, *116*(3), 457-474.
- Blott, S. J., & Pye, K. (2001). GRADISTAT: a grain size distribution and statistics package for the analysis of unconsolidated sediments. *Journal of Geophysical Research*, *106*(k), (11), 1237-1248.
- Boggs, S. (2006). *Journal of Geophysical Research*, *111*(k), k. : Pearson Prentice Hall.
- Bond, G., Kromer, B., Beer, J., Muscheler, R., Evans, M. N., Showers, W., . . . Bonani, G. (2001). Persistent solar influence on north Atlantic climate during the Holocene. *Journal of Geophysical Research*, *106*(5549), 2130-2136.
- Bond, G., Showers, W., Cheseby, M., Lotti, R., Almasi, P., Priore, P., . . . Bonani, G. (1997). A pervasive millennial-scale cycle in North Atlantic Holocene and glacial climates. *Journal of Geophysical Research*, *102*(5341), 1257-1266.
- Brown, D. P., & Comrie, A. C. (2004). A winter precipitation 'dipole' in the western United States associated with multidecadal ENSO variability. *Journal of Geophysical Research*, *109*(9).
- Cai, W., & Cowan, T. (2007). Trends in Southern Hemisphere circulation in IPCC AR4 models over 1950-99: Ozone depletion versus greenhouse forcing. *Journal of Geophysical Research*, *112*(k), (4), 681-693.
- Cai, W., Shi, G., Cowan, T., Bi, D., & Ribbe, J. (2005). The response of the Southern Annular Mode, the East Australian Current, and the southern mid-latitude ocean circulation to global warming. *Journal of Geophysical Research*, *110*(23).
- Campagne, P., Crosta, X., Houssais, M.-N., Swingedouw, D., Schmidt, S., Martin, A., . . . Closset, I. (2015). Glacial ice and atmospheric forcing on the Mertz Glacier Polynya over the past 250 years. *Journal of Geophysical Research*, *120*(k), k.
- Cane, M. A. (2005). The evolution of El Niño, past and future. *Journal of Geophysical Research*, *110*(3), 227-240.
- Carter, L., McCave, I., & Williams, M. J. (2008). Circulation and water masses of the Southern Ocean: a review. *Journal of Geophysical Research*, *113*(k), k, 85-114.

- Carter, L., Mitchell, J., & Day, N. (1981). Suspended sediment beneath permanent and seasonal ice, Ross Ice Shelf, Antarctica. *K* (2), 249-262.
- Cavalieri, D. J., Parkinson, C. L., Gloersen, P., Comiso, J. C., & Zwally, H. J. (1999). Deriving long-term time series of sea ice cover from satellite passive-microwave multisensor data sets. (C7), 15803-15814.
- Chewings, J. M., Atkins, C. B., Dunbar, G. B., & Golledge, N. R. (2014). Aeolian sediment transport and deposition in a modern high-latitude glacial marine environment. *k* (6), 1535-1557.
- Clark, P. U., Dyke, A. S., Shakun, J. D., Carlson, A. E., Clark, J., Wohlfarth, B., . . . McCabe, A. M. (2009). The last glacial maximum. (5941), 710-714.
- Clement, A. C., Seager, R., & Cane, M. A. (2000). Suppression of El Niño during the Mid-Holocene by changes in the Earth's orbit. (6), 731-737.
- Comiso, J. C. (2006). Abrupt decline in the Arctic winter sea ice cover. (18).
- Comiso, J. C., & Nishio, F. (2008). Trends in the sea ice cover using enhanced and compatible AMSR-E, SSM/I, and SMMR data. (C2).
- Conroy, J. L., Overpeck, J. T., Cole, J. E., Shanahan, T. M., & Steinitz-Kannan, M. (2008). Holocene changes in eastern tropical Pacific climate inferred from a Galápagos lake sediment record. (11), 1166-1180.
- Cook, C. P., van de Flierdt, T., Williams, T., Hemming, S. R., Iwai, M., Kobayashi, M., . . . Khim, B.-K. (2013). Dynamic behaviour of the East Antarctic ice sheet during Pliocene warmth. *K* (9), 765-769.
- Cook, E., Bird, T., Peterson, M., Barbetti, M., Buckley, B., D'Arrigo, R., & Francey, R. (1992). Climatic change over the last millennium in Tasmania reconstructed from tree-rings. (3), 205-217.
- Cook, E., Buckley, B., D'arrigo, R., & Peterson, M. (2000). Warm-season temperatures since 1600 BC reconstructed from Tasmanian tree rings and their relationship to large-scale sea surface temperature anomalies. *k* *k* (2-3), 79-91.
- Cook, E. R., Buckley, B. M., & D'Arrigo, R. (1996). Inter-decadal climate oscillations in the Tasmanian sector of the Southern Hemisphere: evidence from tree rings over the past three millennia *k* *k* (pp. 141-160): Springer.
- Costa, E., Dunbar, R., Kryc, K., Mucciarone, D., Brachfeld, S., Roark, E., . . . Leventer, A. (2007). Solar forcing and El Niño-Southern Oscillation (ENSO) influences on productivity cycles interpreted from a late-Holocene high-resolution marine sediment record, Adélie Drift, East Antarctic Margin. *F* .
- Coxall, H. K., Wilson, P. A., Pälike, H., Lear, C. H., & Backman, J. (2005). Rapid stepwise onset of Antarctic glaciation and deeper calcite compensation in the Pacific Ocean. *K* (7021), 53-57.
- Cremer, H., Gore, D., Melles, M., & Roberts, D. (2003). Palaeoclimatic significance of late Quaternary diatom assemblages from southern Windmill Islands, East Antarctica. *k* (3), 261-280.
- Crespin, J., Yam, R., Crosta, X., Masse, G., Schmidt, S., Campagne, P., & Shemesh, A. (2014). Holocene glacial discharge fluctuations and recent instability in East Antarctica. , 38-47.
- Croot, P. L., Andersson, K., Öztürk, M., & Turner, D. R. (2004). The distribution and speciation of iron along 6 E in the Southern Ocean. *#* (22), 2857-2879.

- Crosta, X., Debret, M., Denis, D., Courty, M. A., & Ther, O. (2007). Holocene long- and short-term climate changes off Adelie Land, East Antarctica. *Journal of Quaternary Science*, *22*(3), 271-280.
- Crosta, X., Denis, D., & Ther, O. (2008). Sea ice seasonality during the Holocene, Adelie Land, East Antarctica. *Journal of Quaternary Science*, *23*(3-4), 222-232.
- Crosta, X., Pichon, J.-J., & Labracherie, M. (1997). Distribution of Chaetoceros resting spores in modern peri-Antarctic sediments. *Journal of Quaternary Science*, *12*(3), 283-299.
- Crowley, T. J. (2000). Causes of climate change over the past 1000 years. *Journal of Quaternary Science*, *15*(5477), 270-277.
- Cunningham, W. L., Leventer, A., Andrews, J. T., Jennings, A. E., & Licht, K. J. (1999). Late Pleistocene-Holocene marine conditions in the Ross Sea, Antarctica: evidence from the diatom record. *Journal of Quaternary Science*, *14*(2), 129-139.
- Damon, P. E., & Sonett, C. P. (1991). *Journal of Quaternary Science*, *16*(3), 271-280. Paper presented at the The Sun in Time.
- Davis, B. A. S., & Brewer, S. (2009). Orbital forcing and role of the latitudinal insolation/temperature gradient. *Journal of Quaternary Science*, *24*(2-3), 143-165.
- De Santis, L., Brancolini, G., Donda, F., & O'Brien, P. (2010). Cenozoic deformation in the George V Land continental margin (East Antarctica). *Journal of Quaternary Science*, *25*(1), 1-17.
- Debret, M., Bout-Roumazielles, V., Grousset, F., Desmet, M., McManus, J. F., Massei, N., . . . Trentesaux, A. (2007). The origin of the 1500-year climate cycles in Holocene North-Atlantic records. *Journal of Quaternary Science*, *22*(2), 679-692.
- DeConto, R., Pollard, D., & Harwood, D. (2007). Sea ice feedback and Cenozoic evolution of Antarctic climate and ice sheets. *Journal of Quaternary Science*, *22*(3), 271-280.
- DeConto, R. M., & Pollard, D. (2003). Rapid Cenozoic glaciation of Antarctica induced by declining atmospheric CO<sub>2</sub>. *Journal of Quaternary Science*, *18*(6920), 245-249.
- DeConto, R. M., & Pollard, D. (2016). Contribution of Antarctica to past and future sea-level rise. *Journal of Quaternary Science*, *31*(7596), 591-597.
- Denis, D., Crosta, X., Barbara, L., Masse, G., Renssen, H., Ther, O., & Giraudeau, J. (2010). Sea ice and wind variability during the Holocene in East Antarctica: insight on middle-high latitude coupling. *Journal of Quaternary Science*, *25*(27-28), 3709-3719.
- Denis, D., Crosta, X., Schmidt, S., Carson, D. S., Ganeshram, R. S., Renssen, H., . . . Giraudeau, J. (2009a). Holocene glacier and deep water dynamics, Adélie Land region, East Antarctica. *Journal of Quaternary Science*, *24*(13-14), 1291-1303.
- Denis, D., Crosta, X., Schmidt, S., Carson, D. S., Ganeshram, R. S., Renssen, H., . . . Giraudeau, J. (2009b). Holocene productivity changes off Adelie Land (East Antarctica). *Journal of Quaternary Science*, *24*(12), 1137-1147.
- Denis, D., Crosta, X., Zaragosi, S., Romero, O., Martin, B., & Mas, V. (2006). Seasonal and subseasonal climate changes recorded in laminated diatom ooze sediments, Adelie Land, East Antarctica. *Journal of Quaternary Science*, *21*(8), 1137-1147.
- Deschamps, P., Durand, N., Bard, E., Hamelin, B., Camoin, G., Thomas, A. L., . . . Yokoyama, Y. (2012). Ice-sheet collapse and sea-level rise at the Bolling warming 14,600 years ago. *Journal of Quaternary Science*, *27*(7391), 559-564.
- Ding, Q., Steig, E. J., Battisti, D. S., & Wallace, J. M. (2012). Influence of the tropics on the Southern Annular Mode. *Journal of Quaternary Science*, *27*(18), 6330-6348.
- Domack, E., Amblas, D., Gilbert, R., Brachfeld, S., Camerlenghi, A., Rebesco, M., . . . Urgeles, R. (2006). Subglacial morphology and glacial evolution of the Palmer deep outlet system, Antarctic Peninsula. *Journal of Quaternary Science*, *21*(1), 125-142.

- Domack, E., Leventer, A., Dunbar, R., Taylor, F., Brachfeld, S., & Sjunneskog, C. (2001). Chronology of the Palmer Deep site, Antarctic Peninsula: a Holocene palaeoenvironmental reference for the circum-Antarctic. *Journal of Quaternary Science*, *16*(1), 1-9.
- Domack, E., & Williams, C. (1990). Fine structure and suspended sediment transport in three Antarctic fjords. *Journal of Marine Research*, *48*, 71-89.
- Dunbar, R. B., Anderson, J. B., Domack, E. W., & Jacobs, S. S. (1985). Oceanographic influences on sedimentation along the Antarctic continental shelf. *Journal of Geophysical Research*, *90*, 291-312.
- Dutton, A., & Lambeck, K. (2012). Ice volume and sea level during the last interglacial. *Journal of Quaternary Science*, *27*(6091), 216-219.
- Eitrem, S. L. (1994). Transition from continental to oceanic crust on the Wilkes-Adélie margin of Antarctica. *Journal of Geophysical Research*, *99*(B12), 24189-24205.
- Escutia, C., Brinkhuis, H., Klaus, A., & Scientists, E. (2011). Retrieved from
- Escutia, C., De Santis, L., Donda, F., Dunbar, R., Cooper, A., Brancolini, G., & Eitrem, S. (2005). Cenozoic ice sheet history from East Antarctic Wilkes Land continental margin sediments. *Journal of Quaternary Science*, *20*(1), 51-81.
- Ferraccioli, F., Armadillo, E., Jordan, T., Bozzo, E., & Corr, H. (2009). Aeromagnetic exploration over the East Antarctic Ice Sheet: a new view of the Wilkes Subglacial Basin. *Journal of Geophysical Research*, *114*(1), 62-77.
- Finocchiaro, F., Langone, L., Colizza, E., Fontolan, G., Giglio, F., & Tuzzi, E. (2005). Record of the early Holocene warming in a laminated sediment core from Cape Hallett Bay (Northern Victoria Land, Antarctica). *Journal of Quaternary Science*, *20*(1), 193-206.
- Flower, B. P., & Kennett, J. P. (1995). Middle Miocene deepwater paleoceanography in the southwest Pacific: relations with East Antarctic Ice Sheet development. *Journal of Geophysical Research*, *100*(6), 1095-1112.
- Fogt, R. L., & Bromwich, D. H. (2006). Decadal variability of the ENSO teleconnection to the high-latitude South Pacific governed by coupling with the Southern Annular Mode\*. *Journal of Geophysical Research*, *111*(k), 979-997.
- Fogt, R. L., Bromwich, D. H., & Hines, K. M. (2011). Understanding the SAM influence on the South Pacific ENSO teleconnection. *Journal of Geophysical Research*, *116*(7-8), 1555-1576.
- Fogt, R. L., Perlwitz, J., Monaghan, A. J., Bromwich, D. H., Jones, J. M., & Marshall, G. J. (2009). Historical SAM variability. Part II: twentieth-century variability and trends from reconstructions, observations, and the IPCC AR4 models\*. *Journal of Geophysical Research*, *114*(k), 5346-5365.
- Fogwill, C. J., Turney, C. S., Meissner, K. J., Gollidge, N. R., Spence, P., Roberts, J. L., . . . Carter, L. (2014). Testing the sensitivity of the East Antarctic Ice Sheet to Southern Ocean dynamics: past changes and future implications. *Journal of Quaternary Science*, *29*(1), 91-98.
- Folk, R. L., & Ward, W. C. (1957). Brazos River bar: a study in the significance of grain size parameters. *Journal of Sedimentation*, *1*(1).
- Fukamachi, Y., Wakatsuchi, M., Taira, K., Kitagawa, S., Ushio, S., Takahashi, A., . . . Fukuchi, M. (2000). Seasonal variability of bottom water properties off Adélie Land, Antarctica. *Journal of Geophysical Research*, *105*(C3), 6531-6540.
- Gedalof, Z. e., Mantua, N. J., & Peterson, D. L. (2002). A multi-century perspective of variability in the Pacific Decadal Oscillation: new insights from tree rings and coral. *Journal of Geophysical Research*, *107*(24).
- Godfred-Spenning, C. R., & Simmonds, I. (1996). An analysis of Antarctic sea-ice and extratropical cyclone associations. *Journal of Geophysical Research*, *101*(k), 1315-1332.

- Golledge, N., Menviel, L., Carter, L., Fogwill, C., England, M., Cortese, G., & Levy, R. (2014). Antarctic contribution to meltwater pulse 1A from reduced Southern Ocean overturning. *K* *k* *k*.
- Golledge, N. R., Fogwill, C. J., Mackintosh, A. N., & Buckley, K. M. (2012). Dynamics of the last glacial maximum Antarctic ice-sheet and its response to ocean forcing. *K* *k* (40), 16052-16056.
- Golledge, N. R., Kowalewski, D. E., Naish, T. R., Levy, R. H., Fogwill, C. J., & Gasson, E. G. (2015). The multi-millennial Antarctic commitment to future sea-level rise. *K* (7573), 421-425.
- Gomez, B., Carter, L., Orpin, A. R., Cobb, K. M., Page, M. J., Trustrum, N. A., & Palmer, A. S. (2011). ENSO/SAM interactions during the middle and late Holocene. *K* (7573), 0959683611405241.
- Goodge, J. W., & Fanning, C. M. (2010). Composition and age of the East Antarctic Shield in eastern Wilkes Land determined by proxy from Oligocene-Pleistocene glaciomarine sediment and Beacon Supergroup sandstones, Antarctica. *k* (7-8), 1135-1159.
- Gregory, T. R. (2012). *K* *k* *k*. Cardiff University.
- Grove, J. M. (2013). *F* (Vol. 2): Routledge.
- Hall, A., & Visbeck, M. (2002). Synchronous variability in the Southern Hemisphere atmosphere, sea ice, and ocean resulting from the Annular Mode\*. *k* (21), 3043-3057.
- Hall, B. L., Henderson, G. M., Baroni, C., & Kellogg, T. B. (2010). Constant Holocene Southern-Ocean 14 C reservoir ages and ice-shelf flow rates. *k* (1), 115-123.
- Hammer, Ø. (2013a). *K* *k* *k*: University of Oslo.
- Hammer, Ø., & Harper, D. (2013b). PAST: Paleontological statistics Version 3.0. *K* *k* *k*.
- Hammer, Ø., Harper, D., & Ryan, P. (2001). PAST: Paleontological Statistics Software Package for Education and Data Analysis. *Paleontología Electrónica* 4: 1: 9. <http://www.uio.no/~palaeo/past/>. *k* *k*.
- Harris, P. T., & Beaman, R. J. (2003). Processes controlling the formation of the Mertz Drift, George Vth continental shelf, East Antarctica: evidence from 3.5 kHz sub-bottom profiling and sediment cores. *FF* (8), 1463-1480.
- Harris, P. T., Brancolini, G., Armand, L., Busetti, M., Beaman, R. J., Giorgetti, G., . . . Trincardi, F. (2001). Continental shelf drift deposit indicates non-steady state Antarctic bottom water production in the Holocene. *FF* (1), 1-8.
- Haywood, A., Valdes, P., Lunt, D., & Pekar, S. (2010). *K* *k* *k*. Paper presented at the EGU General Assembly Conference Abstracts.
- Hodell, D. A., Kanfoush, S. L., Shemesh, A., Crosta, X., Charles, C. D., & Guilderson, T. P. (2001). Abrupt cooling of Antarctic surface waters and sea ice expansion in the South Atlantic sector of the Southern Ocean at 5000 cal yr BP. *FF* (2), 191-198.
- Hosking, J. S., Orr, A., Marshall, G. J., Turner, J., & Phillips, T. (2013). The influence of the Amundsen–Bellingshausen Seas low on the climate of West Antarctica and its representation in coupled climate model simulations. *K* *k* (17), 6633-6648.

- Hoskins, B. J., & Karoly, D. J. (1981). The steady linear response of a spherical atmosphere to thermal and orographic forcing. *J. Geophys. Res.* **86**, 1179-1196.
- Hughes, M. K., & Diaz, H. F. (1994). Was there a 'Medieval Warm Period', and if so, where and when? *Geology* **22**, 109-142.
- Hunt, B. G. (2006). The medieval warm period, the little ice age and simulated climatic variability. *Quaternary Science Reviews* **25**, 677-694.
- Huybers, P., & Denton, G. (2008). Antarctic temperature at orbital timescales controlled by local summer duration. *Nature* **455**, 787-792.
- Jacobs, S. S. (2004). Bottom water production and its links with the thermohaline circulation. *Journal of Marine Research* **62**, 427-437.
- Jacobs, S. S., & Giulivi, C. F. (2010). Large multidecadal salinity trends near the Pacific-Antarctic continental margin. *Journal of Geophysical Research* **115**, 4508-4524.
- Jacobs, S. S., Jenkins, A., Giulivi, C. F., & Dutrieux, P. (2011). Stronger ocean circulation and increased melting under Pine Island Glacier ice shelf. *Journal of Geophysical Research* **116**, 519-523.
- Joughin, I., Smith, B. E., & Medley, B. (2014). Marine ice sheet collapse potentially under way for the Thwaites Glacier Basin, West Antarctica. *Nature* **513**, 735-738.
- Kennett, J. (1976). Oxygen isotopic evidence for the development of the psychrosphere 38 Myr ago. *Journal of Geophysical Research* **81**, 513-515.
- Kim, J.-H., Van der Meer, J., Schouten, S., Helmke, P., Willmott, V., Sangiorgi, F., . . . Damsté, J. S. S. (2010). New indices and calibrations derived from the distribution of crenarchaeal isoprenoid tetraether lipids: Implications for past sea surface temperature reconstructions. *Journal of Geophysical Research* **115**, 4639-4654.
- Kim, J. H., Crosta, X., Willmott, V., Renssen, H., Bonnin, J., Helmke, P., . . . Sinninghe Damsté, J. S. (2012). Holocene subsurface temperature variability in the eastern Antarctic continental margin. *Journal of Geophysical Research* **117**, C06001.
- Kirkup, H., Melles, M., & Gore, D. B. (2002). Late Quaternary environment of southern Windmill islands, east Antarctica. *Journal of Geophysical Research* **107**, 385-394.
- Kirtman, B. P., & Schopf, P. S. (1998). Decadal variability in ENSO predictability and prediction. *Journal of Geophysical Research* **103**, 2804-2822.
- Kleinschmidt, G., & Talarico, F. (2000). The Mertz shear zone. *Journal of Geophysical Research* **105**, 109-115.
- Konert, M., & Vandenberghe, J. (1997). Comparison of laser grain size analysis with pipette and sieve analysis: a solution for the underestimation of the clay fraction. *Journal of Geophysical Research* **102**, 523-535.
- König-Langlo, G., King, J., & Pettré, P. (1998). Climatology of the three coastal Antarctic stations Dumont d'Urville, Neumayer, and Halley. *Journal of Geophysical Research* **103**, 10935-10946.
- Kreutz, K., Mayewski, P. A., Pittalwala, I., Meeker, L., Twickler, M., & Whitlow, S. (2000). Sea level pressure variability in the Amundsen Sea region inferred from a West Antarctic glaciochemical record. *Journal of Geophysical Research* **105**, 4047.
- Krissek, L., Browne, G., Carter, L., Cowan, E., Dunbar, G., McKay, R., . . . Wilch, T. (2007). Sedimentology and stratigraphy of the AND-1B Core, ANDRILL McMurdo Ice Shelf Project, Antarctica.
- Kusahara, K., & Hasumi, H. (2013). Modeling Antarctic ice shelf responses to future climate changes and impacts on the ocean. *Journal of Geophysical Research* **118**, 2454-2475.

- Kusahara, K., Hasumi, H., & Williams, G. D. (2011a). Dense shelf water formation and brine-driven circulation in the Adélie and George V Land region. (3–4), 122-138.
- Kusahara, K., Hasumi, H., & Williams, G. D. (2011b). Impact of the Mertz Glacier Tongue calving on dense water formation and export. *K* *k* *k*, 159.
- Kushner, P. J., Held, I. M., & Delworth, T. L. (2001). Southern Hemisphere atmospheric circulation response to global warming. *k* (10), 2238-2249.
- Kwok, R., & Comiso, J. (2002). Southern Ocean climate and sea ice anomalies associated with the Southern Oscillation. *k* (5), 487-501.
- Lacarra, M., Houssais, M.-N., Sultan, E., Rintoul, S., & Herbaut, C. (2011). Summer hydrography on the shelf off Terre Adélie/George V Land based on the ALBION and CEAMARC observations during the IPY. (2), 88-103.
- Lacarra, M., Houssais, M. N., Herbaut, C., Sultan, E., & Beauverger, M. (2014). Dense shelf water production in the Adélie Depression, East Antarctica, 2004–2012: Impact of the Mertz Glacier calving. (8), 5203-5220.
- Lachlan-Cope, T., & Connolley, W. (2006). Teleconnections between the tropical Pacific and the Amundsen-Bellinghausens Sea: Role of the El Niño/Southern Oscillation. *k* (D23).
- Lawver, L. A., Gahagan, L. M., & Coffin, M. F. (1992). The development of paleoseaways around Antarctica. *k*, 7-30.
- Lefebvre, W., Goosse, H., Timmermann, R., & Fichefet, T. (2004). Influence of the Southern Annular Mode on the sea ice–ocean system. (C9).
- Leventer, A. (1991). Sediment trap diatom assemblages from the northern Antarctic Peninsula region. (8), 1127-1143.
- Leventer, A. (2003). Particulate flux from sea ice in polar waters. *k*, 303-332.
- Leventer, A., Domack, E., Barkoukis, A., McAndrews, B., & Murray, J. (2002). Laminations from the Palmer Deep: A diatom-based interpretation. (3).
- Leventer, A., Domack, E., Dunbar, R., Pike, J., Stickley, C., Maddison, E., . . . McClennen, C. (2006). Marine sediment record from the East Antarctic margin reveals dynamics of ice sheet recession. (12), 4.
- Leventer, A., Domack, E. W., Ishman, S. E., Brachfeld, S., McClennen, C. E., & Manley, P. (1996). Productivity cycles of 200–300 years in the Antarctic Peninsula region: understanding linkages among the sun, atmosphere, oceans, sea ice, and biota. *k* (12), 1626-1644.
- Leventer, A., & Dunbar, R. B. (1988). Recent diatom record of McMurdo Sound, Antarctica: Implications for history of sea ice extent. (3), 259-274.
- Lewis, D. W., & McConchie, D. (2012). *k* : Springer Science & Business Media.
- Lieser, J., Curran, M., Bowie, A., Davidson, A., Doust, S., Fraser, A., . . . Melbourne-Thomas, J. (2015). Antarctic slush-ice algal accumulation not quantified through conventional satellite imagery: Beware the ice of March. , 6187-6222.
- Liu, J., Curry, J. A., & Martinson, D. G. (2004). Interpretation of recent Antarctic sea ice variability. (2).
- Liu, Z., Pagani, M., Zinniker, D., DeConto, R., Huber, M., Brinkhuis, H., . . . Pearson, A. (2009). Global cooling during the Eocene-Oligocene climate transition. (5918), 1187-1190.

- Lorenz, S. J., Kim, J. H., Rimbu, N., Schneider, R. R., & Lohmann, G. (2006). Orbitally driven insolation forcing on Holocene climate trends: Evidence from alkenone data and climate modeling. *Journal of Climate*, *19*(1), 1-13.
- Lytle, V., Worby, A., Massom, R., Paget, M., Allison, I., Wu, X., & Roberts, A. (2001). Ice formation in the Mertz Glacier polynya, East Antarctica, during winter. *Journal of Geophysical Research*, *106*(3), 368-372.
- Mackintosh, A., Golledge, N., Domack, E., Dunbar, R., Leventer, A., White, D., . . . Zwartz, D. (2011). Retreat of the East Antarctic ice sheet during the last glacial termination. *Journal of Geophysical Research*, *116*(3), 195-202.
- Mackintosh, A. N., Verleyen, E., O'Brien, P. E., White, D. A., Jones, R. S., McKay, R., . . . Post, A. L. (2014). Retreat history of the East Antarctic Ice sheet since the last glacial maximum. *Journal of Geophysical Research*, *119*, 10-30.
- Maddison, E. J., Pike, J., & Dunbar, R. (2012). Seasonally laminated diatom-rich sediments from Dumont d'Urville Trough, East Antarctic Margin: Late-Holocene Neoglacial sea-ice conditions. *Journal of Geophysical Research*, *117*(8), 857-875.
- Maddison, E. J., Pike, J., Leventer, A., Dunbar, R., Brachfeld, S., Domack, E. W., . . . McClennen, C. (2006). Post-glacial seasonal diatom record of the Mertz Glacier Polynya, East Antarctica. *Journal of Geophysical Research*, *111*(1), 66-88.
- Mann, M. E., & Lees, J. M. (1996). Robust estimation of background noise and signal detection in climatic time series. *Journal of Geophysical Research*, *101*(3), 409-445.
- Marshall, G. J. (2003). Trends in the Southern Annular Mode from observations and reanalyses. *Journal of Climate*, *16*(24), 4134-4143.
- Marshall, G. J. (2007). Half-century seasonal relationships between the Southern Annular Mode and Antarctic temperatures. *Journal of Climate*, *20*(3), 373-383.
- Marshall, G. J., Stott, P. A., Turner, J., Connolley, W. M., King, J. C., & Lachlan-Cope, T. A. (2004). Causes of exceptional atmospheric circulation changes in the Southern Hemisphere. *Journal of Climate*, *17*(14), 2111-2126.
- Marshall, J., & Speer, K. (2012). Closure of the meridional overturning circulation through Southern Ocean upwelling. *Journal of Geophysical Research*, *117*(3), 171-180.
- Marsland, S., Church, J., Bindoff, N., & Williams, G. (2007). Antarctic coastal polynya response to climate change. *Journal of Geophysical Research*, *112*(C7), C7301.
- Marsland, S. J., Bindoff, N. L., Williams, G. D., & Budd, W. F. (2004). Modeling water mass formation in the Mertz Glacier Polynya and Adelie Depression, East Antarctica. *Journal of Geophysical Research*, *109*(C11), C11301.
- Martin, J. H. (1990). Glacial-interglacial CO<sub>2</sub> change: The iron hypothesis. *Journal of Geophysical Research*, *95*(1), 1-13.
- Martin, J. H., & Fitzwater, S. (1988). Iron deficiency limits phytoplankton growth in the north-east Pacific subarctic. *Journal of Geophysical Research*, *93*(3414343), 947-975.
- Massom, R., Hill, K., Lytle, V., Worby, A., Paget, M., & Allison, I. (2001). Effects of regional fast-ice and iceberg distributions on the behaviour of the Mertz Glacier polynya, East Antarctica. *Journal of Geophysical Research*, *106*(1), 391-398.
- Masson-Delmotte, V., Buiron, D., Ekaykin, A., Frezzotti, M., Gallée, H., Jouzel, J., . . . Oerter, H. (2011). A comparison of the present and last interglacial periods in six Antarctic ice cores. *Journal of Geophysical Research*, *116*(2), 397-423.
- Masson, V., Vimeux, F., Jouzel, J., Morgan, V., Delmotte, M., Ciais, P., . . . Mosley-Thompson, E. (2000). Holocene climate variability in Antarctica based on 11 ice-core isotopic records. *Journal of Geophysical Research*, *105*(3), 348-358.

- Mayewski, P., & Maasch, K. (2006). Recent warming inconsistent with natural association between temperature and atmospheric circulation over the last 2000 years. *k* (3), 327-355.
- Mayewski, P. A., Rohling, E. E., Stager, J. C., Karlén, W., Maasch, K. A., Meeker, L. D., . . . Holmgren, K. (2004). Holocene climate variability. (3), 243-255.
- McCartney, M. S., & Donohue, K. A. (2007). A deep cyclonic gyre in the Australian–Antarctic Basin. (4), 675-750.
- McCave, I., & Hall, I. R. (2006). Size sorting in marine muds: Processes, pitfalls, and prospects for paleoflow-speed proxies. *k* (10).
- McCave, I. N., Manighetti, B., & Robinson, S. G. (1995). Sortable silt and fine sediment size composition slicing-parameters for paleocurrent speed and paleoceanography. (3), 593-610.
- McKay, R., Browne, G., Carter, L., Cowan, E., Dunbar, G., Krissek, L., . . . Talarico, F. (2009). The stratigraphic signature of the late Cenozoic Antarctic Ice Sheets in the Ross Embayment. *k* (11-12), 1537-1561.
- McKay, R., Golledge, N. R., Maas, S., Naish, T., Levy, R., Dunbar, G., & Kuhn, G. (2016). Antarctic marine ice-sheet retreat in the Ross Sea during the early Holocene. (1), 7-10.
- McManus, J. F., Francois, R., Gherardi, J.-M., Keigwin, L. D., & Brown-Leger, S. (2004). Collapse and rapid resumption of Atlantic meridional circulation linked to deglacial climate changes. *K* (6985), 834-837.
- McMullen, K., Domack, E., Leventer, A., Olson, C., Dunbar, R., & Brachfeld, S. (2006). Glacial morphology and sediment formation in the Mertz Trough, East Antarctica. *k* (1), 169-180.
- McPhaden, M. J. (2015). Tropical Atmosphere Ocean project diagrams. Retrieved from [http://www.pmel.noaa.gov/tao/proj\\_over/diagrams/index.html](http://www.pmel.noaa.gov/tao/proj_over/diagrams/index.html)
- Meehl, G. A., Stocker, T. F., Collins, W. D., Friedlingstein, P., Gaye, A. T., Gregory, J. M., . . . Noda, A. (2007). Global climate projections. *k* (10), 747-845.
- Meredith, M. P. (2013). Oceanography: Replenishing the abyss. *K* (3), 166-167.
- Miller, K., Wright, J., Katz, M., Browning, J., Cramer, B., Wade, B., & Mizintseva, S. (2008). A view of Antarctic ice-sheet evolution from sea-level and deep-sea isotope changes during the Late Cretaceous–Cenozoic. (10), 55-70.
- Miller, K. G., Wright, J. D., Browning, J. V., Kulpeck, A., Kominz, M., Naish, T. R., . . . Sosdian, S. (2012). High tide of the warm Pliocene: Implications of global sea level for Antarctic deglaciation. (5), 407-410.
- Moore, J. K., & Abbott, M. R. (2000). Phytoplankton chlorophyll distributions and primary production in the Southern Ocean. (12), C12.
- Moore, J. K., Abbott, M. R., Richman, J. G., & Nelson, D. M. (2000). The Southern Ocean at the last glacial maximum: A strong sink for atmospheric carbon dioxide. *k* (1), 455-475.
- Moreno, P., Francois, J., Moy, C., & Villa-Martínez, R. (2010). Covariability of the Southern Westerlies and atmospheric CO<sub>2</sub> during the Holocene. (8), 727-730.
- Morgan, V. I. (2009). Antarctic Cold Reversal. *k* (pp. 22-24): Springer.

- Moros, M., De Deckker, P., Jansen, E., Perner, K., & Telford, R. J. (2009). Holocene climate variability in the Southern Ocean recorded in a deep-sea sediment core off South Australia. *Journal of Marine Research*, 67(19), 1932-1940.
- Mortlock, R. A., & Froelich, P. N. (1989). A simple method for the rapid determination of biogenic opal in pelagic marine sediments. *Deep Sea Research*, 36(9), 1415-1426.
- Moy, C. M., Seltzer, G. O., Rodbell, D. T., & Anderson, D. M. (2002). Variability of El Niño/Southern Oscillation activity at millennial timescales during the Holocene epoch. *Science*, 297(5578), 162-165.
- Newton, K. (2015). *Climate Change: The Science and Solutions*. University of Birmingham. School of Geography, Earth and Environmental Sciences.
- Nielsen, S. H., Koç, N., & Crosta, X. (2004). Holocene climate in the Atlantic sector of the Southern Ocean: Controlled by insolation or oceanic circulation? *Journal of Marine Research*, 62(4), 317-320.
- Nøst, O. A., & Østerhus, S. (1998). Impact of grounded icebergs on the hydrographic conditions near the Filchner Ice Shelf. *Journal of Marine Research*, 56(3), 267-284.
- Ohshima, K. I., Fukamachi, Y., Williams, G. D., Nihashi, S., Roquet, F., Kitade, Y., . . . Field, I. (2013). Antarctic Bottom Water production by intense sea-ice formation in the Cape Darnley polynya. *Journal of Marine Research*, 71(3), 235-240.
- Orsi, A. H., & Wiederwohl, C. L. (2009). A recount of Ross Sea waters. *Journal of Marine Research*, 67(13), 778-795.
- Orsi, A. J., Cornuelle, B. D., & Severinghaus, J. P. (2012). Little Ice Age cold interval in West Antarctica: evidence from borehole temperature at the West Antarctic Ice Sheet (WAIS) divide. *Journal of Marine Research*, 70(9), 1455-1468.
- Pachauri, R. K., Allen, M. R., Barros, V., Broome, J., Cramer, W., Christ, R., . . . Dasgupta, P. (2014). *Climate Change 2014: The Physical Science Basis*. Working Group I Contribution to the Fifth Assessment Report of the Intergovernmental Panel on Climate Change (IPCC).
- Panizzo, V., Crespin, J., Crosta, X., Shemesh, A., Massé, G., Yam, R., . . . Cardinal, D. (2014). Sea ice diatom contributions to Holocene nutrient utilization in East Antarctica. *Journal of Marine Research*, 72(4), 328-343.
- Parish, T., Pettré, P., & Wendler, G. (1993). The influence of large-scale forcing on the katabatic wind regime at Adelie Land, Antarctica. *Journal of Marine Research*, 51(3-4), 165-176.
- Parker, D. (1983). Documentation of a Southern Oscillation index. *Journal of Marine Research*, 41(1331), 184-188.
- Patterson, M. O., McKay, R., Naish, T., Escutia, C., Jimenez-Espejo, F. J., Raymo, M. E., . . . McManis, J. E. (2014). Orbital forcing of the east antarctic ice sheet during the pliocene and early pleistocene. *Journal of Marine Research*, 72(1), 1-12.
- Pezza, A. B., Rashid, H. A., & Simmonds, I. (2012). Climate links and recent extremes in Antarctic sea ice, high-latitude cyclones, Southern Annular Mode and ENSO. *Journal of Marine Research*, 70(1-2), 57-73.
- Pierce, D. W., Barnett, T. P., & Mikolajewicz, U. (1995). Competing roles of heat and freshwater flux in forcing thermohaline oscillations. *Journal of Marine Research*, 53(9), 2046-2064.
- Powell, R., & Domack, E. (1995). Modern glaciomarine environments. *Journal of Marine Research*, 53(4), 445-486.

- Presti, M., De Santis, L., Brancolini, G., & Harris, P. T. (2005). Continental shelf record of the East Antarctic Ice Sheet evolution: seismo-stratigraphic evidence from the George V Basin. *Journal of Geophysical Research*, *110*, 1223-1241.
- Presti, M., De Santis, L., Busetti, M., & Harris, P. T. (2003). Late Pleistocene and Holocene sedimentation on the George V continental shelf, East Antarctica. *Journal of Geophysical Research*, *108*, 1441-1461.
- Prézelin, B. B., Hofmann, E. E., Mengelt, C., & Klinck, J. M. (2000). The linkage between Upper Circumpolar Deep Water (UCDW) and phytoplankton assemblages on the west Antarctic Peninsula continental shelf. *Journal of Geophysical Research*, *105*, 165-202.
- Pritchard, H., Ligtenberg, S., Fricker, H., Vaughan, D., Van den Broeke, M., & Padman, L. (2012). Antarctic ice-sheet loss driven by basal melting of ice shelves. *Nature*, *491*, 502-505.
- Raphael, M. (2003). Impact of observed sea-ice concentration on the Southern Hemisphere extratropical atmospheric circulation in summer. *Journal of Geophysical Research*, *108*, D22.
- Renssen, H., Goosse, H., Fichefet, T., Masson-Delmotte, V., & Koç, N. (2005). Holocene climate evolution in the high-latitude Southern Hemisphere simulated by a coupled atmosphere-sea ice-ocean-vegetation model. *Journal of Geophysical Research*, *110*, 951-964.
- Rhodes, R. H., Bertler, N. A. N., Baker, J. A., Steen-Larsen, H. C., Sneed, S. B., Morgenstern, U., & Johnsen, S. J. (2012). Little Ice Age climate and oceanic conditions of the Ross Sea, Antarctica from a coastal ice core record. *Journal of Geophysical Research*, *117*, 1223-1238.
- Riaux-Gobin, C., Poulin, M., Dieckmann, G., Labrune, C., & Vétion, G. (2011). Spring phytoplankton onset after the ice break-up and sea-ice signature (Adélie Land, East Antarctica). *Journal of Geophysical Research*, *116*, C05001.
- Rignot, E., Mouginot, J., & Scheuchl, B. (2011). Ice flow of the Antarctic ice sheet. *Journal of Geophysical Research*, *116*, 1427-1430.
- Rintoul, S., Hughes, C., & Olbers, D. (2001). The Antarctic circumpolar current system. *Journal of Geophysical Research*, *106*, 271-302.
- Rintoul, S. R. (1998). On the origin and influence of Adélie Land Bottom Water. *Journal of Geophysical Research*, *103*, 151-171.
- Rintoul, S. R. (2007). Rapid freshening of Antarctic Bottom Water formed in the Indian and Pacific oceans. *Journal of Geophysical Research*, *112*, C06001.
- Rintoul, S. R., & Bullister, J. L. (1999). A late winter hydrographic section from Tasmania to Antarctica. *Journal of Geophysical Research*, *104*, 1417-1454.
- Roscoe, H. K., & Haigh, J. D. (2007). Influences of ozone depletion, the solar cycle and the QBO on the Southern Annular Mode. *Journal of Geophysical Research*, *112*, 1855-1864.
- Russell, J. L., Dixon, K. W., Gnanadesikan, A., Stouffer, R. J., & Toggweiler, J. R. (2006). The Southern Hemisphere westerlies in a warming world: Propping open the door to the deep ocean. *Journal of Geophysical Research*, *111*, 6382-6390.
- Sambrotto, R. N., Matsuda, A., Vaillancourt, R., Brown, M., Langdon, C., Jacobs, S. S., & Measures, C. (2003). Summer plankton production and nutrient consumption patterns in the Mertz Glacier Region of East Antarctica. *Journal of Geophysical Research*, *108*, 1393-1414.
- Santoso, A., McGregor, S., Jin, F.-F., Cai, W., England, M. H., An, S.-I., . . . Guilyardi, E. (2013). Late-twentieth-century emergence of the El Niño propagation asymmetry and future projections. *Journal of Geophysical Research*, *118*, 126-130.

- Schulz, M., & Mudelsee, M. (2002). REDFIT: estimating red-noise spectra directly from unevenly spaced paleoclimatic time series. *k* (3), 421-426.
- Sedwick, P. N., DiTullio, G. R., & Mackey, D. J. (2000). Iron and manganese in the Ross Sea, Antarctica: Seasonal iron limitation in Antarctic shelf waters. (C5), 11321-11336.
- Sedwick, P. N., Harris, P. T., Robertson, L. G., McMurtry, G. M., Cremer, M. D., & Robinson, P. (2001). Holocene sediment records from the continental shelf of Mac. Robertson Land, East Antarctica. (2), 212-225.
- Sen Gupta, A., Santoso, A., Taschetto, A. S., Ummenhofer, C. C., Trevena, J., & England, M. H. (2009). Projected changes to the Southern Hemisphere ocean and sea ice in the IPCC AR4 climate models. *k* (11), 3047-3078.
- Shadwick, E., Rintoul, S. R., Tilbrook, B., Williams, G., Young, N., Fraser, A., . . . Tamura, T. (2013). Glacier tongue calving reduced dense water formation and enhanced carbon uptake. (5), 904-909.
- Shevenell, A., Ingalls, A., Domack, E., & Kelly, C. (2011). Holocene Southern Ocean surface temperature variability west of the Antarctic Peninsula. *K* (7333), 250-254.
- Shevenell, A. E., & Kennett, J. P. (2002). Antarctic Holocene climate change: A benthic foraminiferal stable isotope record from Palmer Deep. (2).
- Shin, S.-I., Liu, Z., Otto-Bliesner, B., Brady, E., Kutzbach, J., & Harrison, S. (2003). A simulation of the Last Glacial Maximum climate using the NCAR-CCSM. *k* *k* (2-3), 127-151.
- Shindell, D. T., & Schmidt, G. A. (2004). Southern Hemisphere climate response to ozone changes and greenhouse gas increases. (18).
- Siani, G., Michel, E., De Pol-Holz, R., DeVries, T., Lamy, F., Carel, M., . . . Lourantou, A. (2013). Carbon isotope records reveal precise timing of enhanced Southern Ocean upwelling during the last deglaciation. *K* *k* *k* .
- Siegert, M. J. (2001). *F* *k* : John Wiley & Sons Inc.
- Sigman, D. M., Hain, M. P., & Haug, G. H. (2010). The polar ocean and glacial cycles in atmospheric CO<sub>2</sub> concentration. *K* (7302), 47-55.
- Singer, J. K., & Anderson, J. B. (1984). Use of total grain-size distributions to define bed erosion and transport for poorly sorted sediment undergoing simulated bioturbation. (1-4), 335-359.
- Smethie, W. M., & Jacobs, S. S. (2005). Circulation and melting under the Ross Ice Shelf: estimates from evolving CFC, salinity and temperature fields in the Ross Sea. *F* (6), 959-978.
- Smith Jr, W. O., Sedwick, P. N., Arrigo, K. R., Ainley, D. G., & Orsi, A. H. (2012). The Ross Sea in a sea of change. .
- Smith, W. O., & Comiso, J. C. (2008). Influence of sea ice on primary production in the Southern Ocean: A satellite perspective. (C5).
- Spence, P., Saenko, O. A., Dufour, C. O., Le Sommer, J., & England, M. H. (2012). Mechanisms Maintaining Southern Ocean Meridional Heat Transport under Projected Wind Forcing. (11), 1923-1931.
- Stammerjohn, S., Martinson, D., Smith, R., Yuan, X., & Rind, D. (2008). Trends in Antarctic annual sea ice retreat and advance and their relation to El Niño–Southern Oscillation and Southern Annular Mode variability. (C3).

- Steig, E., Brook, E., White, J., Sucher, C., Bender, M., Lehman, S., . . . Clow, G. (1998). Synchronous climate changes in Antarctica and the North Atlantic. (5386), 92-95.
- Steig, E. J., Schneider, D. P., Rutherford, S. D., Mann, M. E., Comiso, J. C., & Shindell, D. T. (2009). Warming of the Antarctic ice-sheet surface since the 1957 International Geophysical Year. *K* (7228), 459-462.
- Stickley, C. E., Pike, J., Leventer, A., Dunbar, R., Domack, E., Brachfeld, S., . . . McClennan, C. (2005). Deglacial ocean and climate seasonality in laminated diatom sediments, Mac. Robertson Shelf, Antarctica. *k* (4), 290-310.
- Strickland, J. D., & Parsons, T. R. (1972). A practical handbook of seawater analysis.
- Stuiver, M., & Braziunas, T. F. (1993). Sun, ocean, climate and atmospheric  $^{14}\text{CO}_2$ : an evaluation of causal and spectral relationships. (4), 289-305.
- Sugden, D. E., Marchant, D. R., & Denton, G. H. (1993). The case for a stable East Antarctic ice sheet: the background. , 151-154.
- Tamura, T., Williams, G., Fraser, A., & Ohshima, K. (2012). Potential regime shift in decreased sea ice production after the Mertz Glacier calving. *K k k* , 826.
- ten Brink, U. S., Hackney, R. I., Bannister, S., Stern, T. A., & Makovsky, Y. (1997). Uplift of the Transantarctic Mountains and the bedrock beneath the East Antarctic ice sheet. (B12), 27603-27621.
- Thomas, R. H., & Bentley, C. R. (1978). A model for Holocene retreat of the West Antarctic Ice Sheet. (2), 150-170.
- Thompson, D. W., & Solomon, S. (2002). Interpretation of recent Southern Hemisphere climate change. (5569), 895-899.
- Thompson, D. W., & Wallace, J. M. (2000). Annular modes in the extratropical circulation. Part I: month-to-month variability\*. *k* (5), 1000-1016.
- Thomson, D. J. (1982). Spectrum estimation and harmonic analysis. *F* (9), 1055-1096.
- Timmermann, A., & Jin, F. F. (2002). A nonlinear mechanism for decadal El Niño amplitude changes. (1).
- Torrence, C., & Compo, G. (1998). A practical guide to wavelet analysis. *bulletin of the American Meteorological Society* 79: 61–78.
- Trenberth, K. (1991). General characteristics of El Niño-southern oscillation. *k k* , 13-42.
- Turner, J. (2004). The El Niño–Southern Oscillation and Antarctica. *F k* (1), 1-31.
- Turner, J., Bindschadler, R., Convey, P., Di Prisco, G., Fahrbach, E., Gutt, J., . . . Summerhayes, C. (2009). *k k* .
- Turner, J., Colwell, S. R., Marshall, G. J., Lachlan-Cope, T. A., Carleton, A. M., Jones, P. D., . . . lagovkina, S. (2004). The SCAR READER project: toward a high-quality database of mean Antarctic meteorological observations. *k* (14), 2890-2898.
- Turner, J., Overland, J. E., & Walsh, J. E. (2007). An Arctic and Antarctic perspective on recent climate change. *F k* (3), 277-293.
- Turner, J., Phillips, T., Hosking, J. S., Marshall, G. J., & Orr, A. (2013). The Amundsen Sea low. *F k* (7), 1818-1829.
- Van Den Broeke, M. R., & Van Lipzig, N. P. (2003). Response of wintertime Antarctic temperatures to the Antarctic Oscillation: Results of a regional climate model. *k k* , 43-58.

- van Ommen, T. D., Morgan, V., & Curran, M. A. (2004). Deglacial and holocene changes in accumulation at Law Dome, East Antarctica. (1), 359-365.
- Vasiliev, S., & Dergachev, V. (2002). *k* Paper presented at the Annales Geophysicae.
- Vautard, R., Yiou, P., & Ghil, M. (1992). Singular-spectrum analysis: A toolkit for short, noisy chaotic signals. *K k* (1), 95-126.
- Verleyen, E., Hodgson, D. A., Sabbe, K., Cremer, H., Emslie, S. D., Gibson, J., . . . Vyverman, W. (2011). Post-glacial regional climate variability along the East Antarctic coastal margin-Evidence from shallow marine and coastal terrestrial records. (4), 199-212.
- Vimeux, F., Masson, V., Jouzel, J., Petit, J. R., Steig, E. J., Stievenard, M., . . . White, J. W. C. (2001). Holocene hydrological cycle changes in the Southern Hemisphere documented in East Antarctic deuterium excess records. *k k* (7), 503-513.
- Wagner, B., Cremer, H., Hultsch, N., Gore, D. B., & Melles, M. (2004). Late Pleistocene and Holocene history of Lake Terrasovoje, Amery Oasis, East Antarctica, and its climatic and environmental implications. *k* (4), 321-339.
- Warner, N. R., & Domack, E. W. (2002). Millennial-to decadal-scale paleoenvironmental change during the Holocene in the Palmer Deep, Antarctica, as recorded by particle size analysis. (3), PAL 5-1-PAL 5-14.
- Weber, M., Clark, P., Kuhn, G., Timmermann, A., Spreng, D., Gladstone, R., . . . Chikamoto, M. (2014). Millennial-scale variability in Antarctic ice-sheet discharge during the last deglaciation. *K* (7503), 134-138.
- Wendler, G., Gilmore, D., & Curtis, J. (1997b). On the formation of coastal polynyas in the area of Commonwealth Bay, Eastern Antarctica. *k* (1), 55-75.
- Wendler, G., Stearns, C., Weidner, G., Dargaud, G., & Parish, T. (1997a). On the extraordinary katabatic winds of Adélie Land. *k* (D4), 4463-4474.
- White, D. A., Fink, D., & Gore, D. B. (2011). Cosmogenic nuclide evidence for enhanced sensitivity of an East Antarctic ice stream to change during the last deglaciation. (1), 23-26.
- Whitworth, T. (2002). Two modes of bottom water in the Australian-Antarctic Basin. (5).
- Whitworth, T., Orsi, A., Kim, S. J., Nowlin, W., & Locarnini, R. (1998). Water masses and mixing near the Antarctic Slope Front. *F k F* *k* , 1-27.
- Williams, G., Aoki, S., Jacobs, S., Rintoul, S., Tamura, T., & Bindoff, N. (2010). Antarctic bottom water from the Adélie and George V Land coast, East Antarctica (140–149 E). (C4).
- Williams, G., & Bindoff, N. (2003). Wintertime oceanography of the Adélie Depression. *F* (8), 1373-1392.
- Williams, G. D., Bindoff, N. L., Marsland, S. J., & Rintoul, S. R. (2008). Formation and export of dense shelf water from the Adélie Depression, East Antarctica. (C4).
- Young, N., Legresy, B., Coleman, R., & Massom, R. (2010). Mertz Glacier tongue unhinged by giant iceberg. (18), 19.
- Yuan, X. (2004). ENSO-related impacts on Antarctic sea ice: a synthesis of phenomenon and mechanisms. (04), 415-425.

- Yuan, X., & Li, C. (2008). Climate modes in southern high latitudes and their impacts on Antarctic sea ice. *Journal of Climate*, 21(C6), 1697-1717.
- Yuan, X., & Martinson, D. G. (2000). Antarctic sea ice extent variability and its global connectivity\*. *Journal of Climate*, 13(10), 1697-1717.
- Zachos, J. C., Quinn, T. M., & Salmey, K. A. (1996). High-resolution (104 years) deep-sea foraminiferal stable isotope records of the Eocene-Oligocene climate transition. *Journal of Geology*, 104(3), 251-266.
- Zhang, Y., Wallace, J. M., & Battisti, D. S. (1997). ENSO-like interdecadal variability: 1900-93. *Journal of Climate*, 10(5), 1004-1020.
- Zhang, Z., Leduc, G., & Sachs, J. P. (2014). El Niño evolution during the Holocene revealed by a biomarker rain gauge in the Galápagos Islands. *Journal of Geology*, 122(3), 420-434.